Real-time Retrieval of Precipitable Water Vapour from GNSS Precise Point Positioning

A thesis submitted in fulfilment of the requirements for the degree of Doctor of Philosophy

Yubin Yuan

B. A., Wuhan University, 2007

M. S., Chinese Academy of Surveying and Mapping, 2010

School of Mathematical and Geospatial Sciences

College of Science Engineering and Health

RMIT University

December 2015

Declaration

I certify that except where due acknowledgement has been made, the work is that of the author alone; the work has not been submitted previously, in whole or in part, to qualify for any other academic award; the content of the thesis is the result of work which has been carried out since the official commencement date of the approved research program; any editorial work, paid or unpaid, carried out by a third party is acknowledged; and, ethics procedures and guidelines have been followed.

Yubin Yuan

10/12/2015

Acknowledgements

I would like to thank my supervisors, Prof. Kefei Zhang and Dr. Suelynn Choy, for their support, encouragement, and guidance over the years. Their work has greatly improved the quality and increased the depth of this research.

I also wish to express my thanks to all of my colleagues at the School of Mathematical and Geospatial Sciences. In particular: Dr. Witold Rohm and Dr. Carl Wang for the technical support and discussions about the retrieval of precipitable water vapour. Dr. Robert Norman and Mr. Lucas Holden are thanked for polishing the thesis.

I have also been teaching at RMIT University for two years. Prof. Matt Duckham, Prof. Mark Shortis and Mr. Thierry Demathieu are thanked for providing teaching opportunities including lectures, practical exercises and lab sessions.

Finally I need to thank my parents for giving me the freedom and backing during my upbringing to let me think anything is possible. Without their encouragement and understanding over the years I would not be able to complete this research process.

Abstract

Global Positioning System (GPS) meteorology (GPS-MET) as a novel approach for precipitable water vapour (PWV) sounding using ground-based GPS receivers has been conducted since earlier 1990s. Further research to date is based on post-processing or near-real-time processing using differenced GPS observations. It still remains a challenging task at high temporal resolutions and in real time. In addition, new Global Navigation Satellite Systems (GNSS) are under development quickly. This has the potential to improve the retrieval of PWV, leading GPS-MET research to a new stage of GNSS-MET. This study aims to take these aspects into account and investigates the retrieval of zenith total delay (ZTD) and PWV using real-time precise point positioning (PPP) approach.

The PPP processing in this study is conducted using the BKG (the Federal Agency for Cartography and Geodesy) NTRIP Client (BNC) software platform which is substantially modified. The modifications include the modelling of tropospheric delay in which GPT2 is implemented and the corrections of error sources such as solid Earth tides, ocean tide loading and the antenna-related. The retrieved ZTD is then converted into PWV by multiplying a dimensionless proportionality which is derived from the Forecast Vienna Mapping Functions 1 (VMF1-FC) model.

The retrievals of ZTD and PWV are validated using GPS observations in a one-month period at 20 globally distributed stations. The derived real-time ZTDs at most stations agree well with the tropospheric products from the International GNSS Service (IGS) and the root mean square (RMS) errors are <12 mm. The RMS errors of the PWVs in comparison with the radiosonde data are $\leqslant$3 mm. Note that 15 mm accuracy is the threshold if ZTDs are input to Numerical Weather Prediction (NWP) models and 3 mm accuracy is the threshold if PWVs are inputs to weather nowcasting according to the document by World Meteorological Organization (WMO). Furthermore, the theoretical accuracy of PWVs in various conditions is analysed. The RMS error of PWV is proved to be a strictly increasing function of zenith wet delay (ZWD) and

weighted mean temperature. Hence the retrieval of PWV is more challenging in higher temperature and humidity conditions. This research proves that even in poor retrieval conditions, i.e., high humidity and temperature, an accuracy of PWV at 3 mm level is still achievable using the real-time ZTD from PPP and the empirical models for the determination of weighted mean temperature.

A preliminary study of the ZTD retrieval using multi-GNSS data is also conducted in this study. The addition of GLONASS (GLObal NAvigation Satellite System) observations will significantly increase the number of visible satellites and improve the Dilution of Precision (DOP) indices like Positional DOP (PDOP) and Geometric DOP (GDOP). However, a test of ZTD retrieval at 12 global IGS stations shows that adding GLONASS data degrades the accuracy of ZTD. A further analysis implies that the multi-GNSS processing can be improved by the refinement of functional model and real-time GLONASS orbits and clocks.

This research realised the real-time, high-accuracy, high temporal- and spatial-resolution retrievals of ZTD and PWV in a context of multiple GNSS constellations. The implemented PPP approach demonstrates its high accuracy in those retrievals. The retrieved real-time ZTD and PWV potentially have a wide range of applications in meteorology such as improving the NWP models and weather nowcasting.

List of Figures

List of Tables

Acronyms

AC	–	IGS Analysis Centre
ACCESS	–	Australian Community Climate and Earth-System Simulator
ARGN	–	Australian Regional GNSS Network
AWS	–	Automatic Weather Station
BDS	–	BeiDou Navigation Satellite System
BKG	–	Bundesamt für Kartographieund Geodäsie (German: Federal Agency for Cartography and Geodesy)
BNC	–	BKG NTRIP Client –
C/A	–	Coarse/Acquisition Code
CODATA	–	Committee on Data for Science and Technology
CoM	–	Centre of Mass
CORS	–	Continuously Operating Reference Station
DCB	–	Differential Code Bias
DD	–	Double-Difference
DoD	–	US Department of Defence
DOY	–	Day of Year
DPB	–	Differential Phase Bias
ECEF	–	Earth Centred Earth Fixed
ECMWF	–	European Centre for Medium-Range Weather Forecasts
EOP	–	Earth Orientation Parameter
EPN	–	EUREF Permanent Network
ERA-40	–	the 40-year period ECMWF Re-Analysis
ESA	–	European Space Agency
ESOC	–	European Space Operations Centre
EU	–	European Union
EUREF	–	European Reference Frame
FDMA	–	Frequency Division Multiple Access
FOC	–	Full Operational Capability
GA	–	Geoscience Australia
GEO	–	Geostationary Earth Orbit
GGOS	–	Global Geodetic Observing System
GLONASS	–	Globalnaya navigatsionnaya sputnikovaya sistema, or GLObal NAvigation Satellite System

GLONASST	–	GLONASS Time
GMF	–	Global Mapping Function
GNSS	–	Global Navigation Satellite System
GNSS-MET	–	GNSS Meteorology
GPL	–	GNU General Public License
GPS	–	Global Positioning System
GPST	–	GPS Time
GPS-MET	–	GPS Meteorology
GPT	–	Global Pressure and Temperature
IAG	–	International Association of Geodesy
IFB	–	Inter-Frequency Bias
IGS	–	International GNSS Service
IGS-RTPP	–	IGS Real-time Pilot Project
IGSO	–	Inclined Geosynchronous Orbit
IGU	–	IGS Ultrarapid
IMF	–	the Isobaric mapping function
IRNSS	–	Indian Regional Navigational Satellite System
ISB	–	Inter-System Bias
MCS	–	Master Control Station
MEO	–	Medium Earth Orbit
MSL	–	Mean Sea Level
MTT	–	MIT Temperature Mapping (function)
NCEP	–	the National Centres of Environmental Prediction
NMF	–	the New Mapping Function
NOAA	–	the National Oceanic and Atmospheric Administration
NPI	–	National Positioning Infrastructure
NTRIP	–	Networked Transport of RTCM via Internet Protocol
NWP	–	Numerical Weather Prediction
PCO	–	Phase Centre Offset
PCV	–	Phase Centre Variation
PNT	–	Positioning, Navigation, and Timing
PPP	–	Precise Point Positioning
PPS	–	Precise Positioning Service
PWV	–	Precipitable Water Vapour
PZ-90	–	Parametry Zemli 1990 (Russian: Earth Parameter System 1990)
QZSS	–	Quasi-Zenith Satellite System

RINEX	–	Receiver Independent Exchange Format
RMS	–	Root Mean Square (Error)
RO	–	Radio Occultation
RTCM	–	Radio Technical Commission for Maritime Services
SPRGN	–	South Pacific Regional GNSS Network
SPS	–	Standard Positioning Service
SSR	–	State Space Representation
STD	–	Standard Deviation
SU	–	Russian National Reference of UTC
TAI	–	International Atomic Time
UNB	–	University of New Brunswick
UTC	–	Coordinated Universal Time
VMF1	–	Vienna Mapping Functions 1
VMF1-FC	–	Forecast VMF1
WGS	–	World Geodetic System
WMO	–	World Meteorological Organization
WVR	–	Water Vapour Radiometer
ZHD	–	Zenith Hydrostatic Delay
ZTD	–	Zenith Total Delay
ZWD	–	Zenith Wet Delay

Table of Contents

Chapter 1. Introduction

1.1 Background

Australia is a country experiencing severe weather and climate conditions. This includes thunderstorms, tropical cyclones and floods due to phenomena like El Niño and La Niña [*Meteorology*, 2014]. The floods in Queensland in 2011 are typical examples of severe weather events and they have caused billions of dollars damage and claimed a large number of lives [*van den Honert and McAneney*, 2011; *ABC News*, 2014]. Those severe weather events have much to do with water vapour in the atmosphere as it is the means by which moisture and latent heat are transported to form specific "weather" phenomena [*Cai and van Rensch*, 2012]. As an important component of greenhouse gas, water vapour plays a critical role in the global climate system. This is not restricted to absorbing and radiating energy from the sun, but also includes the effects it has on the formation of clouds and aerosols and the chemical process of the lower atmosphere [*Bevis et al.*, 1992]. At present climate change and global warming have become a major challenge for the sustainable development of our Earth and its environment. Intensive research needs to be carried out to understand atmospheric processes and their implications. It is widely recognised that the improved monitoring of atmospheric water vapour will lead to more accurate forecasts of precipitation and better understanding of climate and climate change [*Duan et al.*, 1996].

However, despite its critical importance to atmospheric processes over a wide range of spatial and temporal scales, water vapour is still one of the least understood and poorly described components of the Earth's atmosphere [*Bevis et al.*, 1992]. Currently there exist a number of instruments for the sounding of water vapour contents. For example, the radiosonde uses balloon-borne equipment to observe atmospheric parameters. However, this instrument has its serious disadvantages due to the high expense, which largely restricts the number of launches (typically twice daily) and observing locations. In other words, radiosonde measurements are limited for an effective resolution of the temporal and spatial variability of water vapour.

Another sounding instrument is water vapour radiometer (WVR) which measures the microwave radiation produced by atmospheric water vapour and estimates the PWV precisely. While ground-based WVR can provide good temporal coverage, it could not offer good spatial coverage. On the other hand, space-based WVR can provide good spatial coverage, but temporal coverage usually is very poor. It is concluded that the lack of accurate and successive water vapour information is one of the main error sources of short-term precipitation forecasts [*Kuo et al.*, 1993; 1996].

GPS is a satellite-based radio navigation system widely used for navigation, positioning, and timing (PNT) services. It has been routinely used for the continuous monitoring of positions of permanent stations for crustal deformation and plate tectonic movement due to its capability of high positioning precision. On the other hand, GPS has been regarded as a powerful emerging space-borne technology for non-positioning applications. GPS-MET as an innovative approach for PWV sounding is one of those non-positioning applications. The space-based GPS-MET, i.e. GPS radio occultation (RO) is dedicated to limb sounding from satellites [*Kursinski et al.*, 1997; *Wickert et al.*, 2001; *Zhang et al.*, 2011]. Relevant results such as refractivity have been assimilated into operational NWP models and demonstrated their benefits [*Le Marshall et al.*, 2010; 2012; *Ho et al.*, 2014]. The ground-based GPS-MET which was first proposed by *Bevis et al.* (1992) is a promising technique particularly for the retrieval of PWV. Previous studies of the retrieved PWVs [*Poli et al.*, 2007; *Bennitt and Jupp*, 2012] show that they can significantly improve the accuracy of weather forecasting when assimilated into NWP models. The ground-based GPS-MET is proved to be complementary to the conventional sounding means of PWV due to its real-time, all-day and all-weather capabilities and high temporal resolutions.

However, modern weather forecasting systems have an ever increasing demand of GPS-PWV retrieval in terms of: 1) short latency or no latency, 2) higher spatial resolutions of GPS stations while relatively low increase of computational resources is needed, and 3) higher temporal resolutions specifically for severe weather nowcasting [*Li et al.*, 2009]. To meet those tough requirements, new algorithms or new data processing procedures of PWV retrieval need to be investigated. In addition, in the past few years the GPS technique has been developed rapidly.

This includes new satellite constellations, expansion of ground-based infrastructure, and new products generated to facilitate the PNT applications. These developments of the GPS technique are potentially to improve GPS-MET.

The ground-based GPS-MET relies on the development of Continuously Operating Reference Station (CORS) networks, which have been developed quickly all over the world. Take Australia for example, in the past few years almost all states are in the process of either establishing or enhancing their state-wide CORS networks. GPSnet in Victoria is the most advanced and dense state-wide CORS network dedicated to geospatial industry. Currently it has approximately 120 online and fully operational stations and it offers the positioning and navigation correction services for GPS users throughout Victoria, Australia [*Vicmap Position*, 2014]. However, the advanced CORS system has not been well developed for non-positioning purposes and the ground-based GPS derived PWV has not yet been assimilated into the NWP model in Australia. It is highly desirable to incorporate the critical National Positioning Infrastructure (NPI) [*Hausler and Collier*, 2013] of CORS networks into the operational Australian Community Climate and Earth-System Simulator (ACCESS) model, which is the Australian weather forecast model [*Zhang et al.*, 2015].

In the past few years new GNSS space constellations other than GPS and GLONASS have emerged. The sole GPS constellation is moving to multi-GNSS which predominantly consists of the US GPS, Russian GLONASS, Chinese BeiDou Navigation Satellite System (BDS), European Galileo, Japanese QZSS (Quasi-Zenith Satellite System) and Indian IRNSS (Indian Regional Navigational Satellite System). GPS-MET is moving to a new stage of GNSS-MET. Those new constellations are expected to improve the accuracy of current GNSS-MET. However, to date the retrieval of PWV using multi-GNSS is still under development.

1.2 Current Status

Since the first investigation of GPS-MET using ground-based GPS receivers by *Bevis et al.*

(1992) extensive research based on post-processing scenarios has been conducted [*Duan et al.*, 1996; *Tregoning et al.*, 1998; *Hagemann et al.*, 2003; *Rohm et al.*, 2014]. The EUMETNET (the Network of European Meteorological Services) EIG GNSS water vapour programme (E-GVAP) was set up in April 2005 to provide EUMETNET members with GNSS delay and water vapour estimates for operational meteorology in near real-time [*E-GVAP*, 2014]. Currently the E-GVAP network consists of more than 1500 GNSS sites. In some other research, near-real-time GPS-MET products (e.g., the GPS retrieved ZTDs) have also been applied in NWP models [*Poli et al.*, 2007; *Smith et al.*, 2007]. The assimilated ZTDs were proved to be beneficial for cloud forecasting [*Bennitt and Jupp*, 2012] and precipitation forecasting [*Boniface et al.*, 2009]. These researches are based on post-processing with latencies up to several hours. For the real-time scenario, *Lee et al.* (2013) conducted an experiment of PWV retrieval in a six-month period based on a single-difference data processing strategy. The differences of PWVs between the daily solutions and the radiosonde solutions range from 2.1 to 3.4 mm. It should be noted that most of these GPS-MET studies were based on GPS network solutions, which use differenced pseudorange and phase observations over regional or international scale. The data processing is complex in terms of the formation of simultaneous observations and selection of baselines. Furthermore, the significant development and densification of GPS CORS networks has increased the number of observations and hence the data processing load has increased exponentially.

Early tests of the PPP technique using GPS data from single receivers were conducted by *Zumberge et al.* (1997) and *Kouba and Heroux* (2001). In the PPP approach, if accurate satellite orbit and clock products are available, the absolute values of ZTDs rather than the differences between two stations can be estimated and then converted into the corresponding PWVs. IGS has routinely provided the ultra-rapid (IGU) products every six hours with a latency of three hours [*Springer and Hugentobler*, 2001]. However, the predicted part of IGS clocks is not sufficiently accurate for PPP. The IGS Real-time Pilot Project (IGS-RTPP) aims to estimate and distribute high-resolution GPS corrections of orbits and clocks in real time through Networked Transport of RTCM (Radio Technical Commission for Maritime Services) via Internet Protocol (NTRIP) [*Dettmering et al.*, 2006]. The real-time observation and correction stream can be

collected and then converted into the Receiver Independent Exchange (RINEX) format. The IGS Real-time Working Group (RTWG) started to provide the Real-time Service (RTS) since March 2013. The RTS products consist of GNSS satellite orbit and clock corrections to the broadcast ephemeris. These real-time products are then disseminated through NTRIP protocol. This makes real-time high-resolution sensing of PWV possible. To facilitate the real-time PNT applications of RTS products, two open source software packages have been developed for the collection and decoding of such real-time observations and corrections. They are BNC developed by *Mervart and Weber* (2013) at the Federal Agency for Cartography and Geodesy (BKG, Bundesamt für Kartographieund Geodäsie) and RTKLIB developed by *Takasu* (2009) at Tokyo University of Marine Science and Technology.

Based on the IGS RTS service, several researches in PNT applications have been conducted recently. *Dousa and Vaclavovic* (2014) have developed program G-Nut/Tefnut and continuously processed real-time ZTDs in a nine-month demonstration campaign between February and October, 2013 and 36 European and global stations were used. Their ZTD results can be characterised by mean standard deviations of 6–10 mm. Since remaining ZTD biases can be effectively eliminated using reduction procedures prior to the assimilation, results are promising to meet the target requirements of relative accuracy. Currently their real-time strategy and software are still under development. The real-time software GEMon (GREF EUREF Monitoring) is under development through a co-operation between BKG and the Technical University of Darmstadt [*Stürze et al.*, 2014]. GEMon is able to process GPS and GLONASS observation and RTS product streams in PPP mode. In addition, several state-of-the-art tropospheric models, for example, based on numerical weather prediction data, are implemented. Relevant software package is also under development and preliminary research outcomes are available as a form of presentation or conference paper [*Pacione and Söhne*, 2014; *Stürze et al.*, 2014]. It should be noted that those real-time PPP researches have only been conducted in the past two years, after the launch of RTS products in March 2013.

In multi-GNSS research *Bruyninx* (2007) investigates the influence of adding GLONASS observations to the European Reference Frame (EUREF) Permanent Network (EPN)

processing. Their experimental results show that including GLONASS data can change the coordinates at the level of 1–2 mm in the horizontal components and 2-6 mm in the vertical components. For the horizontal components, the coordinate differences are mainly caused by reference frame differences while the cause of vertical coordinate differences is not clear. Their research is based on post-processing using the double-difference approach. *Cai and Gao* (2013) and *Cai et al.* (2014) systematically investigate both functional and stochastic models of PPP using GPS and GLONASS data. The results indicate that the convergence time can be significantly reduced if GLONASS data is included, although the corresponding positioning accuracy is not significantly improved. *Chen et al.* (2013) analysed the precise GPS/GLONASS system bias and they concluded that the precision of GLONASS-only solution can be improved by 55% and the precision of GPS/GLONASS combined solution can be improved by 30% if the system bias is applied into PPP positioning. As a preliminary study of real-time multi-GNSS, *Agrotis et al.* (2014) compared the RTS products with the IGS and ESA rapid solutions. The performance statistics of GPS and GLONASS corrections indicates that the GLONASS corrections are not as accurate as their GPS counterparts. *Hadas and Bosy* (2014) also validated the real-time multi-GNSS orbit and clock products of a one-week period. According to their research the real-time multi-GNSS products are of high accuracy, i.e., 5 cm for GPS orbits, 8 cm for GPS clocks, 13 cm for GLONASS orbits and 24 cm for GLONASS clocks. Unfortunately up to date the real-time positioning or the retrieval of PWV using multi-GNSS data is still under development and no relevant concrete materials have been published.

This thesis is a comprehensive research based on the preliminary work [*Yuan et al.*, 2014]. At the time of writing this thesis, some other institutions have also been undertaking similar investigations. For example, the research about estimating ZTD using data from BDS only [*Xu et al.*, 2013], the PPP technique in a real-time mode [*Li et al.*, 2013; *Shi et al.*, 2015], the real-time retrievals of ZTD and PWV using data from GPS and BDS [*Lu et al.*, 2015b], from GPS and GLONASS [*Lu et al.*, 2015a], from GPS and QZSS [*Choy et al.*, 2015],and from all four GNSS constellations, i.e. GPS, GLONASS, BDS and Galileo [*Li et al.*, 2015]. All those real-time retrievals are enabled thanks to the availability of RTS products.

1.3 Research Aims and Objectives

As is discussed in Section 1.1, the modern weather forecasting system requires the ground-based GPS-MET to be conducted with hourly to sub-hourly latency or even in a real-time mode. Thanks to the effort of IGS, the launch of RTS products enables this application. This research aims to take these aspects into account and comprehensively investigate the retrievals of ZTDs and PWVs using the real-time PPP approach. More specifically, the research objectives are listed as follows:

1) Realise the retrieval of ZTD using PPP technique in real time, at high accuracy and high temporal resolutions using the currently available GPS and GLONASS data.

2) Realise the retrieval of PWV using the ZTD derived from PPP and the empirical models for the conversion from ZTD to PWV. This PWV retrieval will not be dependent on external dataset hence it is ideal for operational applications. It will also achieve high accuracies of ZTD and PWV while the computational resources for high-resolution PPP processing are not highly demanded.

3) Validate the retrieved real-time ZTD and PWV using external datasets. The IGS tropospheric products and radiosonde data are ideal for this purpose. The validation should be conducted in different climatic conditions across the globe over a period which is sufficiently long enough.

4) Test various models which are currently available for mitigating errors in PPP processing and converting ZTD to PWV.

5) Analyse the theoretical accuracies of PWV in different humidity and temperature conditions based on the ZTD obtained from PPP.

1.4 Thesis Outline

Chapter 2 introduces the fundamentals of GNSS. Current GNSS includes the US GPS, Russian GLONASS, Chinese BDS, European Galileo, Japanese QZSS and Indian IRNSS. Those different satellite constellations will be addressed, followed by the introduction of ground infrastructure of CORS networks and the functional models of GPS positioning.

Chapter 3 introduces the fundamentals of ground-based GPS-MET, starting from the structure of the atmosphere and signal path delays. The calculation of refractivity is derived in detail as it is important for the understanding of the retrieval of PWV from GPS-derived ZTD.

Chapter 4 focuses on the modelling of tropospheric delays in PPP processing. ZHD, ZWD, and ZTD are calculated using different empirical models and external meteorological data. At the end of this chapter, several widely-used ZHD models will be validated using *in-situ* meteorological data and the most accurate ones will be implemented in this study.

Chapter 5 explains the PPP algorithms used in this study. This includes the functional model based on the ionosphere-free combination, the Kalman filtering, and several corrections for error sources which significantly influence the accuracy of PPP-ZTD.

Chapter 6 presents the experimental results of the retrieved PPP-ZTD. Substantial modifications on the original BNC software are introduced in detail as this is the key step for the accurate retrieval of PPP-ZTD. To properly validate the results, the selection of reference data is also important and will be investigated.

Chapter 7 focuses on the conversion from ZTD to PWV which involves a number of empirical models like GPT2, GTm-III, VMF1-FC, etc. The experimental results of the retrieved PPP-PWVs are demonstrated in detail, followed by error analysis of PPP-PWV in different temperature and humidity conditions.

Chapter 8 is about the retrieval of PPP-ZTD using multi-GNSS observations and real-time correction streams. It constitutes of four aspects: 1) the observation equation using both GPS and GLONASS observations, 2) the potential benefits from using multi-GNSS data i.e. more visible satellites and the improved DOP indices, 3) demonstration of experimental results and 4) analysis of the sources of the accuracy degradation due to the introduction of GLONASS data.

Chapter 9 summarises the primary outcomes, draws main conclusions from this research and provides a few recommendations for future work based on the limitations of this research.

Chapter 2. Fundamentals of GNSS Positioning

This chapter presents the fundamentals of GNSS positioning, including the satellite constellations in a context of multi-GNSS, the ground infrastructure (i.e. the national and global CORS networks) and positioning algorithms. The current GNSS constellations include the US GPS, Russian GLONASS, Chinese BDS, European Galileo, Japanese QZSS and Indian IRNSS. The ground-based GNSS infrastructure mainly refers to the GNSS CORS networks covering local, national, regional and global scales. When it comes to observation equations, the traditional pseudorange and carrier phase observations, various linear combinations used for different purposes, different positioning modes i.e. PPP and differential positioning are discussed in detail.

2.1 Global Positioning System

The GPS was developed by the US Department of Defence (DoD) in the early 1970s. It was initially developed for military needs and is now available for civilians although with limited functionality. GPS provides users with PNT services. The positioning principle is based on the resection of a number of GPS satellites. As a rule of thumb, the determination of three Cartesian coordinate parameters requires at least three satellites in view. However, the GPS receiver clock is usually unstable, requiring another set of measurements. Therefore, at least four GPS satellites are needed in PNT applications.

The GPS system consists of three segments: the space segment, the control segment, and the user segment. The US Air Force develops, maintains and operates the space and control segments. The space segment consists of medium Earth orbit (MEO) satellites at an altitude of approximately 20,200 km above the ground. Each satellite circles the Earth approximately twice a day. The satellites in the GPS constellation are arranged into six equally-spaced orbital planes surrounding the Earth, with each plane contains four "slots". This minimum of 24 MEO satellites ensures GPS Full Operational Capability (FOC) hence users can view at least four

satellites from virtually any point on the Earth. In June 2011, the US Air Force successfully completed a GPS constellation expansion known as the "Expandable 24" configuration [*US AIR FORCE*, 2014]. Three of the 24 slots were expanded and six satellites were repositioned, so that three of the extra satellites became part of the constellation baseline. As a result, GPS now effectively operates as a 27-slot constellation (Figure 2.1) with improved coverage in most parts of the world. Except those 27 satellites there are several backup satellites and the current GPS constellation consists of 31 satellites (August 17, 2015) according to official U.S. Government information about GPS (http://www.gps.gov/). Technical details about the orbits, coverage, and performance of the GPS satellite constellation are documented in the GPS Performance Standards [*Leick*, 2004; *US Government*, 2008].

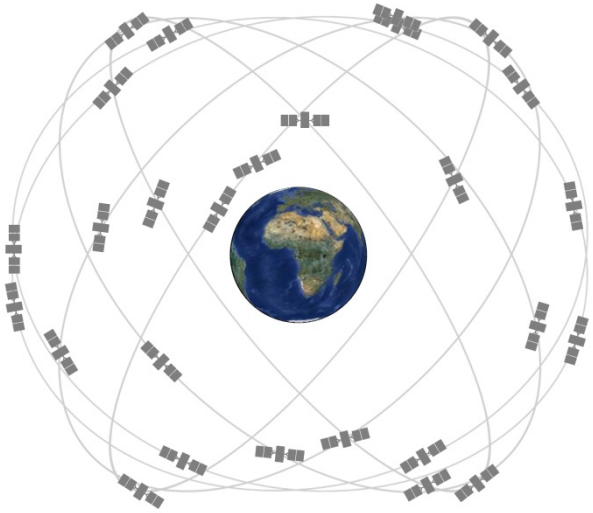

Figure 2.1 GPS 27-slot constellation excluding several backup satellites [*US Naval Observatory,* 2014]

The control segment of the GPS system consists of a worldwide network of ground-based tracking stations. The primary task of the operational control segment is to track the GPS satellites in order to determine and predict satellite locations, system integrity, behaviour of satellite atomic clocks, atmospheric information, satellite almanac along with many other considerations. The master control station (MCS) is located in the United States at Colorado Springs, Colorado. Information from operational control stations is analysed in MCS and then packed and uploaded into the GPS satellites through the S-band link.

The user segment includes users, GPS receivers for all military and civilian users, as well as peripherals such as meteorological instrument, computers, compasses, etc. A GPS receiver is a device which is used to receive and decode signals transmitted by GPS satellites. It consists of at least four components: 1) antenna unit to capture signals and deal with noise and possible interference, 2) front end to down-converts, filters, amplifies and digitises the incoming signals, 3) baseband signal processing to acquire and track different signals and 4) processor to perform different computation tasks. GPS receivers can be categorised by their type in different ways. Based on different target applications, receivers can be for navigation, accurate positioning or timing, surveying, etc. The GPS receivers used in this research are accurate positioning ones with capability of capturing both pseudorange and carrier phase measurements.

To maintain the US leadership in the service, provision, and the use of satellite navigation systems, the US government has been updating the GPS space and control segments with new features, i.e. the GPS modernisation program. This program includes three types of new satellites and two new signals, as well as the control segment updates [*US Naval Observatory*, 2014]. The new satellites to be launched include GPS IIR(M), GPS IIF, and GPS III. The second civil signal L2C on L2 band, also called Coarse/Acquisition (C/A) code, as well as a new carrier phase L5, will also be added to the current signals. When combined with the existing L1C in a dual-frequency receiver, L2C enables the correction of the first order of ionospheric delay. The three carrier phases L1, L2 and L5 enables the ionospheric correction to the second order. The addition of new signals is expected to significantly improve the accuracies of current PNT applications.

2.2 Multiple GNSS

GPS is not the only GNSS constellation available for PNT applications. The former Soviet Union began developing a similar system – GLONASS in the early 1980s and it reached FOC in 1998. However, due to financial difficulties and short satellite life, the number of available GLONASS satellites diminished to 5 in 2002 [*Leick*, 2004] and regained its FOC in December

2011 [*Gibbons*, 2014]. Unlike GPS, its satellites are not differentiated by PRN codes, but rather by means of a Frequency Division Multiple Access (FDMA) approach. The satellites transmit coded signals in two frequencies located on two frequency bands, 1602–1615.5 MHz and 1246–1256.5 MHz, with a frequency interval of 0.5625 MHz and 0.4375 MHz, respectively. So for each satellite *k*, frequencies on L1 and L2 are

$$f_k^{L1} = f_0^{L1} + k \cdot \Delta f^{L1} \tag{2.1}$$

and

$$f_k^{L2} = f_0^{L2} + k \cdot \Delta f^{L2} \tag{2.2}$$

where $f_0^{L1} = 1602\ MHz$ and $f_0^{L2} = 1246\ MHz$ are the nominal frequency on L1 and L2, respectively. $\Delta f^{L1} = 0.5625\ MHz$ and $\Delta f^{L2} = 0.4375\ MHz$ are frequency steps for each satellite. k is the satellite frequency channel number.

Similar to the GPS system, GLONASS also includes three components: A constellation of satellites (space segment equivalent of GPS), ground-based control facilities (control segment equivalent of GPS) and user's equipment (user segment equivalent of GPS) [*GLONASS IAC*, 2015]. GLONASS satellites are evenly spaced in three orbital planes, separated from each other by 120°. Each plane has eight GLONASS satellites separated by an argument of latitude of 45°. The satellites are placed into planes with a target inclination of 64.8°, which is considerably higher than that of GPS [*Xu*, 2007]. Recently the number of active dual-frequency satellites has raised to 24 according to Table 2.1[*GLONASS IAC*, 2015].

Table 2.1 GLONASS constellation status on January 6, 2015

GLONASS No.	Cosmos No.	Plane /slot	Frequ. chann.	Launch date	Intro date	Status
730	2456	1/01	1	14.12.2009	30.01.2010	operating
747	2485	1/02	-4	26.04.2013	04.07.2013	operating
744	2476	1/03	5	04.11.2011	08.12.2011	operating
742	2474	1/04	6	02.10.2011	25.10.2011	operating
734	2458	1/05	1	14.12.2009	10.01.2010	operating
733	2457	1/06	-4	14.12.2009	24.01.2010	operating
745	2477	1/07	5	04.11.2011	18.12.2011	operating
743	2475	1/08	6	14.11.2011	25.12.2011	operating
736	2464	2/09	-2	02.09.2010	04.10.2010	operating
717	2426	2/10	-7	25.12.2006	03.04.2007	operating
723	2436	2/11	0	25.12.2007	22.01.2008	operating
737	2465	2/12	-1	02.09.2010	11.10.2010	operating
721	2434	2/13	-2	25.12.2007	08.02.2008	operating
715	2424	2/14	-7	25.12.2006	03.04.2007	operating
716	2425	2/15	0	25.12.2006	12.10.2007	operating
738	2466	2/16	-1	02.09.2010	12.10.2010	operating
746	2478	3/17	4	28.11.2011	23.12.2011	operating
754	2491	3/18	-3	24.03.2014	14.04.2014	operating
720	2433	3/19	3	26.10.2007	25.11.2007	operating
719	2432	3/20	2	26.10.2007	27.11.2007	operating
755	2500	3/21	4	14.06.2014	03.08.2014	operating
731	2459	3/22	-3	02.03.2010	28.03.2010	operating
732	2460	3/23	3	02.03.2010	28.03.2010	operating
735	2461	3/24	2	02.03.2010	28.03.2010	operating

GLONASS uses a time reference system which is different from that of GPS [*Leick*, 2004]. In GPS Time system (GPST) a continuous time scale (no leap seconds) is defined by the GPS control segment on the basis of a set of atomic clocks at the Monitor Stations and on-board the satellites. It starts at 0h UTC (Coordinated Universal Time, at midnight) of January 5th to 6th 1980 when the difference between International Atomic Time (TAI) and UTC was 19 seconds [*GPS Directorate*, 2011]. Thus

$$GPST = UTC + n + 19s \tag{2.3}$$

where n is the leap seconds.

On the contrary, GLONASS Time (GLONASST) is not continuous. It is generated by the GLONASS Central Synchroniser and the difference between the Russian National Reference of UTC (SU) and GLONASST should not exceed one millisecond plus three hours [*Russian Institute of Space Device Engineering*, 2008]. That is

$$GLONASST = UTC(SU) + 3h - \tau \ (|\tau| < 1\ millisecond) \tag{2.4}$$

Besides the time reference system, the coordinate system used in GLONASS is also different from that is used in GPS. GPS originally employed a coordinate frame known as the World Geodetic System 1972 (WGS72) which is later updated to the World Geodetic System 1984 (WGS84). GLONASS satellites transmit ephemeris data in the Parametry Zemli 1990 (PZ-90) system which is similar in quality to the one employed in WGS-84 [*Russian Institute of Space Device Engineering*, 2008; *GPS Directorate*, 2011].

The key parameters of GPS and GLONASS that must be considered when combining GPS/GLONASS data processing are summarised in Table 2.2.

Table 2.2 Comparisons of the key parameters between GPS and GLONASS

		GPS	GLONASS
Constellation	number of satellites	32	24
	number of orbit planes	6	3
	orbit inclination	55°	64.8°
	orbit altitude	20200 km	19130 km
	orbit period	11h 58 min	11h 15.8 min
Signal Characteristics	multiplexing mode	FDMA	CDMA
	L1 frequency	1575.42 MHz	1602+*k**0.5625 MHz
	L2 frequency	1227.60 MHz	1246+*k**0.4375 MHz
	C/A code frequency	1.023 MHz	0.511 MHz
	P code frequency	10.23 MHz	5.11 MHz
Reference System	time system	GPST	GLONASST
	coordinate system	WGS-84	PZ-90

China began to design its own regional navigation satellite system termed Beidou in 1994, with the first generation consisting of two separate satellite constellations. Now it is at the second generation stage called BDS, with a space constellation of 18 operational satellites in orbit. This includes 5 Geostationary Earth Orbit (GEO) satellites, 7 Inclined Geosynchronous Orbit (IGSO) satellites, and 6 MEO satellites. BDS has been in full service to provide open services to the most part of the Asia-Pacific region shown in Figure 2.2 since December 27, 2012 [*China Satellite Navigation Office*, 2013a].

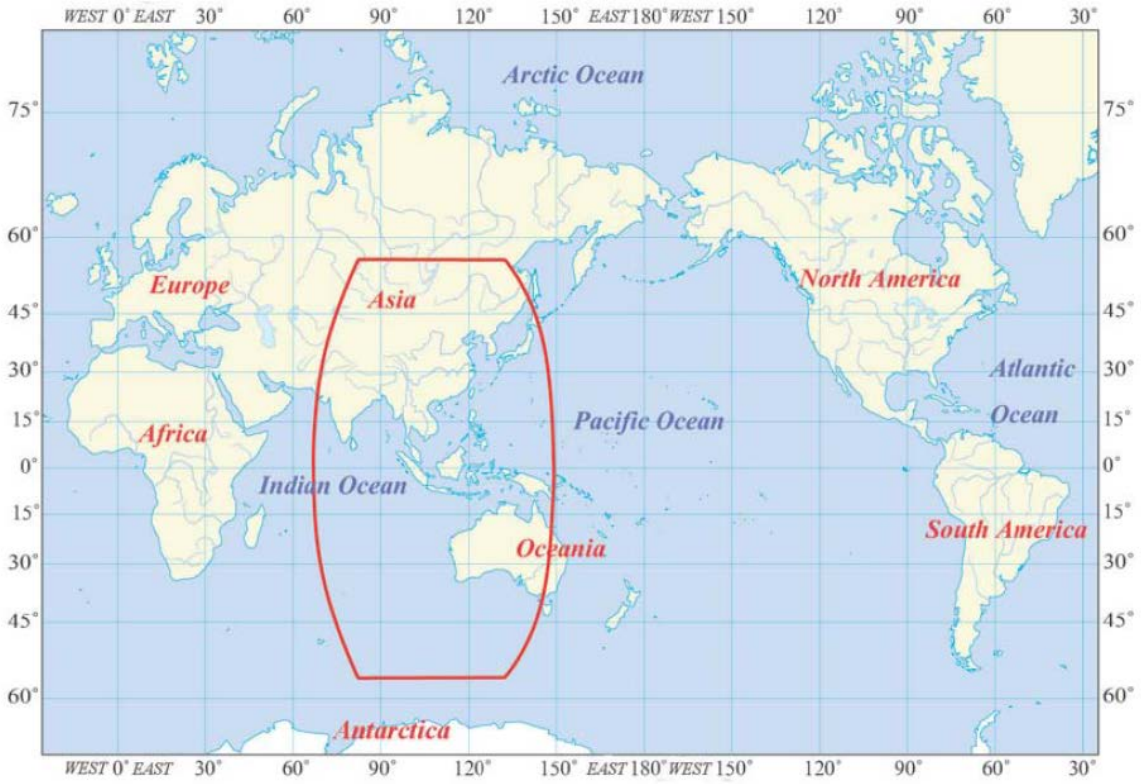

Figure 2.2 The BDS Service Area [*China Satellite Navigation Office,* 2013a]

BDS will provide services to global users in the third generation stage by 2020. According to [*China Satellite Navigation Office*, 2013b], the space constellation of BDS will then consist of 35 satellites, including 5 GEO satellites, 3 IGSO satellites and 27 MEO satellites.

The European Union (EU) and European Space Agency (ESA) intended to develop their Galileo system which is named after the Italian astronomer in 1999. One of the aims of Galileo is to provide a high-precision positioning system upon which European nations can rely. It is intended to be independent from the Russian GLONASS, US GPS, and Chinese BDS, as the latter three can be disabled by their operators in times of war or conflict.

FOC of Galileo needs 27 operational MEO satellites and three spares. The first two of four testing satellites were launched on 21 October 2011, followed by another two on 12 October 2012, to validate the positioning system. However, the first determination of a position relying on signals emitted from Galileo satellites only was achieved on 12 March 2013. FOC of Galileo is scheduled to complete by 2019 then services at two levels of accuracy can be provided. The

low-precision Galileo services will be free and open to everyone, while the high-precision capabilities will be available for commercial and military users only [*European GNSS Programmes*, 2010].

The GPS, GLONASS, BDS and Galileo systems can be used for PNT applications independently. The current Galileo system is in the test stage while the BDS only covers the Asia-Pacific region. Recently some other countries are in the process of developing their regional satellite based augmentation systems, e.g., the Japanese QZSS and Indian IRNSS. However, at the current stage those two GNSSes cannot be used for PNT applications without the dependence on the US GPS [*Rao et al.*, 2001; *Kishimoto et al.*, 2007; *Rao*, 2007; *Hauschild et al.*, 2012]. As such multi-GNSS data from GPS and GLONASS system only are investigated in this study.

2.3 GNSS Ground Infrastructure

Ground-based GNSS meteorology technique relies on the availability of ground infrastructure over all scales – global, national, state-wide and local regions. Taking Australia for example, spatial organisations have been leading the push to develop an NPI that will deliver uniformed access to reliable and accurate PNT information. The NPI will be based on the acquisition, processing and distribution of GNSS data through CORS networks [*Hausler and Collier*, 2013]. The major CORS networks include the Australian Regional GNSS Network (ARGN), the South Pacific Regional GNSS Network (SPRGN), and AuScope (A recent national initiative to characterise the structure and evolution of the Australian continent). All three CORS networks (shown in Figure 2.3) are cooperatively operated and maintained by Geoscience Australia (GA) [*Geoscience Australia*, 2014], which is Australia's national geoscience agency. Due to the ever increasing needs for a high accuracy, real-time positioning and navigation across a large area, almost all states in Australia are in the process of either establishing or enhancing their state-wide CORS networks. GPSnet in Victoria is the most advanced and densest state-wide CORS network dedicated to geospatial industry. Currently it

has approximately 120 fully operational stations [*Vicmap Position*, 2014] and it offers the positioning and navigation correction service for GPS users throughout Victoria, Australia [*Zhang et al.*, 2006].

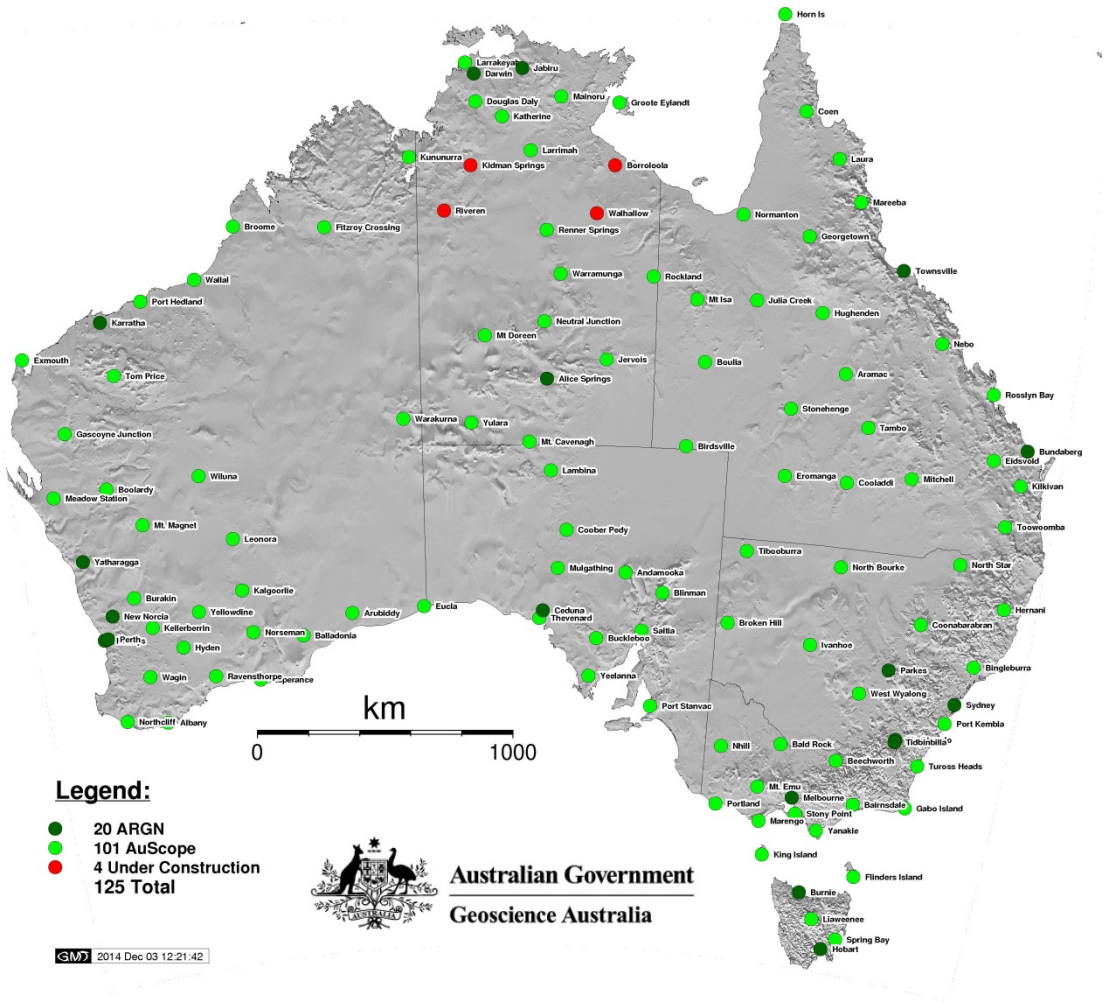

Figure 2.3 A network map of the ARGN and AuScope stations located in Australia [*Geoscience Australia,* 2014]

CORS networks across the globe have been coordinated by the International GNSS Service (IGS), formerly the International GPS Service which was officially established by the International Association of Geodesy (IAG) in January 1994. IGS is a voluntary federation of more than 200 worldwide agencies. It aims to provide the highest quality data and products for GNSS in support of Earth science research, multidisciplinary applications and education. Currently only the GPS and the GLONASS are available for global users, therefore these two GNSSes are included in the IGS routine analysis, with intention to incorporate future GNSSes

like BDS and Galileo systems [*Dow et al.*, 2009; *IGS*, 2014].

2.4 International GNSS Service

The IGS collects, archives, and distributes GPS and GLONASS observation datasets to meet the objectives of a wide range of scientific and engineering users. Those observations are collected from over 350 IGS stations [*IGS*, 2014]. Users from all over the world can access and download these datasets for their own applications. In addition, these datasets are analysed by the IGS Analysis Centres (ACs) which commit to deliver some or all of the core products promptly and reliably. These ACs are shown in Table 2.3.

Table 2.3 The current IGS Analysis Centres

Abbreviations	Full name
CODE	Center for Orbit Determination in Europe, AIUB, Switzerland
ESOC	European Space Operations Center, ESA, Germany
GOP-RIGTC	Geodetic Observatory Pecny, Czech Republic
GFZ	GeoForschungsZentrum, Germany
GRGS	GRGS-CNES/CLS, Toulouse, France
JPL	Jet Propulsion Laboratory, USA
MIT	Massachusetts Institute of Technology, USA
NOAA	National Oceanic and Atmospheric Administration / NGS, USA
NRCan	Natural Resources Canada, Canada
SIO	Scripps Institution of Oceanography, USA
USNO	US Naval Observatory, USA
WHU	Wuhan University, China

Based on the provided products from the above ACs, the IGS Analysis Centre Coordinator generates a wide range of combined products which are available to interested users through the internet. The generated products include:

- GPS satellite ephemerides
- GLONASS satellite ephemerides

- Earth rotation parameters
- Coordinates and velocities of IGS tracking stations
- Clock information of GPS satellites and IGS tracking stations
- Zenith tropospheric path delay estimates
- Global ionospheric maps

The IGS official website lists the accuracy levels of the above products. Those of interest to this research are collected and tabulated in Table 2.4. In this table, orbit accuracies are 1D mean RMS values over the three geocentric components. IGS accuracy limits, except for predicted orbits, are based on comparisons with independent laser ranging results and discontinuities between consecutive days. The RMS accuracy of all clocks is expressed relative to the IGS timescale, which is linearly aligned to GPS time in one-day segments [*IGS*, 2014].

Table 2.4 The current IGS products which are updated routinely by the IGS [*IGS*, 2014]

		Accuracy	Latency	Update	Interval
GPS Satellite Ephemerides & Clocks	Broadcast Orbits	~100 cm	Real-time	--	daily
	Broadcast Clocks	~5 ns	Real-time	--	daily
	IGU Predicted Orbits	~5 cm	Real-time	6-hourly	15 min
	IGU Predicted Clocks	~3 ns	Real-time	6-hourly	15 min
	Rapid Orbits	~2.5 cm	17-41 hours	daily	15 min
	Rapid Clocks	~75 ps	17-41 hours	daily	5 min
	Final Orbits	~2.5 cm	12-18 days	weekly	15 min
	Final Clocks	~75 ps	12-18 days	weekly	30s
GLONASS Satellite Ephemerides	Final orbits[a]	~3 cm	12-18 days	weekly	15 min
Geocentric Coordinates of IGS Stations	Horizontal Position	3 mm	11-17 days	weekly	weekly
	Vertical Position	6 mm	11-17 days	weekly	weekly
	Horizontal Velocity	2 mm/year	11-17 days	weekly	weekly
	Vertical Velocity	3 mm/year	11-17 days	weekly	weekly
Zenith Path Delay	Final	4 mm	<4 weeks	weekly	2 hours
	IGU	6 mm	2-3 hours	3-hourly	1 hour

[a]Statistics of GLONASS clocks are not available.

Recently IGS is engaged in RTS which is supported by the RTWG. The RTS products consist of GNSS satellite orbit and clock corrections to the broadcast ephemeris. The generation of those

RTS products is based on the IGS global infrastructure of network stations, data centres and analysis centres that provide high-precision GNSS products. The dissemination of those products relies on the internet. RTCM's 'State Space Representation' (SSR) working group has developed appropriate v3 messages to disseminate such broadcast corrections in real time through the NTRIP protocol [*IGS*, 2015]. This enables real-time PPP and related applications, such as time synchronisation and disaster monitoring, on worldwide scales. The definition of SSR messages in RTCM v3 format is listed in Table 2.5.

Table 2.5 Broadcast corrections in RTCM version 3 format [*IGS*, 2015]

Message	Contents
1019	GPS Broadcast Ephemeris
1020	GLONASS Broadcast Ephemeris
1045	Galileo Broadcast Ephemeris
1057	GPS orbit corrections to Broadcast Ephemeris
1058	GPS clock corrections to Broadcast Ephemeris
1059	GPS code biases
1060	Combined orbit and clock corrections to GPS Broadcast Ephemeris
1061	GPS User Range Accuracy
1062	High-rate GPS clock corrections to Broadcast Ephemeris
1063	GLONASS orbit corrections to Broadcast Ephemeris
1064	GLONASS clock corrections to Broadcast Ephemeris
1065	GLONASS code biases
1066	Combined orbit and clock corrections to GLONASS Broadcast Ephemeris
1067	GLONASS User Range Accuracy
1068	High-rate GLONASS clock corrections to Broadcast Ephemeris

Currently the RTS is still under development. It is offered as a beta service in terms of GPS for the development and testing of applications, which will be used and discussed later in Section 6.2. In terms of GLONASS it is initially provided as an experimental product and will be included within the service when the RTS reaches its full operating capability at the end of 2015

[*IGS*, 2015]. The GLONASS products will be used and discussed later in Section 8.3.

2.5 GPS Observation Equations and Linear Combinations

2.5.1 GPS Observation Equations

Precise GPS positioning involves the code and phase measurements on both frequencies. Code measurement is recorded in metres while the phase measurement is recorded in unit of phase cycles. The phase measurement is more complex as it includes the integer and the fractional part of the phases. GPS observation equations between a single dual-frequency receiver and a single GPS satellite can be expressed as [*Kouba and Heroux*, 2001; *Dach et al.*, 2007]:

$$\begin{aligned}\Phi_1^p(t) = {} & \rho^p(t) + cdt(t) - cdt^p(t) + d_{ant}^p + d_{rot}(t) + d_{rel}(t) + d_{otl}(t) \\ & + d_{set} + T^p(t) - I^p(t) + \frac{c}{f_1}\left\{N_1^p + \phi_1(t) - \phi_1^p(t-\tau)\right\}_1 + d_{windup} + \varepsilon_{\Phi 1}^p\end{aligned} \tag{2.5}$$

$$\begin{aligned}\Phi_2^p(t) = {} & \rho^p(t) + cdt(t) - cdt^p(t) + d_{ant}^p + d_{rot}(t) + d_{rel}(t) + d_{otl}(t) \\ & + d_{set} + T^p(t) - \frac{f_1^2}{f_2^2} I^p(t) + \frac{c}{f_2}\left\{N_2^p + \phi_2(t) - \phi_2^p(t-\tau)\right\}_2 + d_{windup} + \varepsilon_{\Phi 2}^p\end{aligned} \tag{2.6}$$

$$\begin{aligned}P_1^p(t) = {} & \rho^p(t) + cdt(t) - cdt^p(t) + d_{ant}^p + d_{rot}(t) + d_{rel}(t) + d_{otl}(t) \\ & + d_{set} + T^p(t) + I^p(t) + \varepsilon_{P1}^p\end{aligned} \tag{2.7}$$

$$\begin{aligned}P_2^p(t) = {} & \rho^p(t) + cdt(t) - cdt^p(t) + d_{ant}^p + d_{rot}(t) + d_{rel}(t) + d_{otl}(t) \\ & + d_{set} + T^p(t) + \frac{f_1^2}{f_2^2} I^p(t) + \varepsilon_{P2}^p\end{aligned} \tag{2.8}$$

where

P	represents the code measurement in metres
Φ	represent the phase measurement in metres

superscript ^{p}	represents the PRN of the GPS satellite
f_1, f_2	represent the L1 and L2 frequencies, respectively: $f_1 = 1575.42$ MHz, $f_2 = 1227.60$ MHz
c	represents the speed of light in vacuum
t	represents the GPS time when the signal is received
τ	represents the GPS signal travelling time
$\Phi_1^p(t), \Phi_2^p(t)$	represents the phase measurements in metres on L1 and L2, respectively
$P_1^p(t), P_2^p(t)$	are the pseudorange measurements on L1 and L2, respectively
$\rho^p(t)$	represents the geometric distance between satellite and receiver
$dt^p(t)$	represents the satellite clock offset from GPST
$dt(t)$	represents the receiver clock offset from GPST
d_{ant}^p	represents the phase centre offset & variation of satellite antenna
$d_{rot}(t)$	represents the effect by the Earth rotation
$d_{rel}(t)$	represents the relativistic effects
$d_{otl}(t)$	represents the effect of ocean tide loading
d_{set}	represents the effect of solid Earth tide
d_{windup}	represents the satellite phase wind up error
$I^p(t)$	represents the signal path delay due to the ionosphere
$T^p(t)$	represents the signal path delay due to the neutral-atmosphere
N_1^p, N_2^p	represent the initial integer ambiguities on L1 and L2, respectively
$\phi_1(t),\ \phi_2(t)$	represent the phase generated by the receiver oscillator at signal reception time t
$\phi_1^p(t-\tau), \phi_2^p(t-\tau)$	represent the phase of the carrier at emission time $t-\tau$ on L1 and L2, respectively
$\varepsilon_{\Phi 1}^p,\ \varepsilon_{\Phi 2}^p, \varepsilon_{P1}^p,\ \varepsilon_{P2}^p$	represent residual errors including orbit errors, multipath, signal noises, etc.

The ambiguity items can be simplified as $N^{*p}_1 = N_1^p + \phi_1(t) - \phi_1^p(t-\tau)$ and $N^{*p}_2 = N_2^p + \phi_2(t) - \phi_2^p(t-\tau)$ and taken as one parameter for each frequency in GPS data processing. The geometric distance between GPS satellite and receiver is calculated using the

following equation

$$\rho^p(t) = \sqrt{\left\{\left(X_s^p(t-\tau)\right) - X_r\right\}^2 + \left\{\left(Y_s^p(t-\tau)\right) - Y_r\right\}^2 + \left\{\left(Z_s^p(t-\tau)\right) - Z_r\right\}^2} \quad (2.9)$$

where X_s^p, Y_s^p, Z_s^p represent the Earth Centred Earth Fixed (ECEF) coordinates of the satellite and X_r, Y_r, Z_r represent the ECEF coordinates of the receiver.

2.5.2 Linear Combinations

Equations (2.5) – (2.8) contain a number of error sources that need to be properly removed or mitigated. Linear combination of observations in terms of different observation types (i.e. pseudorange and phase measurement), receivers and satellites is an effective way for this purpose. In addition, the GPS raw data tends to be coarse and preparation work is necessary before parameter estimation. The preparation includes the detection of gross errors and cycle slips in the raw measurements. In this context, linear combinations of phase measurements φ_1 and φ_2 (in phase) are particularly useful and widely used in GPS data processing:

$$\varphi = n_1\varphi_1 + n_2\varphi_2 \quad (2.10)$$

where n_1 and n_2 are the linear combination coefficients. If $l_1 = \lambda_1\varphi_1$, $l_2 = \lambda_2\varphi_2$ (λ_1, λ_2 represent the wavelengths of L1 and L2, respectively) then the range of combination φ in metres will be

$$l = \alpha_1 l_1 + \alpha_2 l_2 \quad (\alpha_i = n_i \frac{\lambda}{\lambda_i}) \quad (2.11)$$

Similarly, the corresponding frequency and ambiguity parameter will be

$$f = n_1 f_1 + n_2 f_2 \tag{2.12}$$

and

$$N = n_1 N_1 + n_2 N_2 \tag{2.13}$$

Assuming φ_1 and φ_2 are independent and their measurement noises are σ, the measurement noise of combination φ will be

$$\begin{cases} \sigma_\lambda = \sigma\sqrt{n_1^2 + n_2^2} & \text{(in cycles)} \\ \sigma_l = \sigma\sqrt{\alpha_1^2 + \frac{f_1^2}{f_2^2}\alpha_2^2} & \text{(in metres)} \end{cases} \tag{2.14}$$

Substituting equations (2.5) and (2.6) in equation (2.11) indicates that the first order of ionospheric delay of φ will be cancelled if $n_1 = \frac{f_1^2}{f_1^2 - f_2^2}, n_2 = \frac{f_1 f_2}{f_1^2 - f_2^2}$. This so-called ionosphere-free combination constitutes the functional model in this investigation. Its disadvantages include the non-integer ambiguity, as well as the noise which is almost three times as big as that of L1 measurement according to equation (2.14).

If $n_1 = 1, n_2 = -1$ then we obtain the wide-lane combination. Its ambiguity remains an integer according to equation (2.13). However, the combined wavelength is approximately 86 cm, which is much bigger than that of L1 (approximately 19 cm) or L2 (approximately 24 cm). The longer wavelength makes the wide-lane measurements much easier for the detection of cycle slips. However, only the ambiguity difference $N_1 - N_2$ can be calculated according to equation (2.13), which requires an extra geometry-free combination (when $n_1 = \lambda_1, n_2 = -\lambda_2$) to determine the N_1 and N_2 values. According to equation (2.11) it removes the satellite orbit error, receiver clock offset, satellite clock offset and tropospheric delay. It is ideal for the detection and determination of cycle slips together with the wide-lane combination.

2.6 GPS Positioning Models

2.6.1 Single Point Positioning

There are two positioning modes when it comes to the manipulation of raw observations. One is single point positioning using observations from a single station while another is differential positioning using observations from at least two stations and/or two satellites. A general mode of single point positioning is to use pseudorange observations and broadcast ephemerides hence the resultant accuracy tends to be coarse. As an optimal mode of single point positioning, PPP uses both pseudorange and carrier phase observations together with high-accuracy post-processed orbits, clocks and Earth orientation parameters (EOP). Parameters to be estimated are station coordinates, receiver clocks, tropospheric parameters and ambiguities. Furthermore, various error sources such as ocean tide loading, phase wind-up, PCV and PCO are corrected. All those lead to a more accurate approach of positioning to provide station coordinates and an inverse approach to retrieve atmospheric delays. This research takes the benefits of PPP to obtain epoch-by-epoch tropospheric delays and further to derive PWVs.

Section 2.5.2 lists various combinations of phase observations which are widely utilised in the detection of gross error measurements and cycle slips. At the stage of parameter estimation, both the phase and pseudorange observations are used simultaneously so as to make the most out of raw measurements if high-accuracy positioning is required. The widely-used combined observations of phase and pseudorange includes the Melbourne-Wübbena combination described by *Melbourne* (1985) and *Wübbena* (1985), and the combination based on ionosphere-free carrier phases and ionosphere-free pseudoranges.

The Melbourne-Wübbena combination is expressed by

$$L_{M-W} = \frac{f_1 L_1 - f_2 L_2}{f_1 - f_2} - \frac{f_1 P_1 + f_2 P_2}{f_1 + f_2} \tag{2.15}$$

This combination eliminates the effect of ionosphere, troposphere, geometry and clocks. In addition, the combined wavelength is approximately 86 cm, which is much bigger than that of L1 or L2. The longer wavelength makes the Melbourne-Wübbena measurement easier for the detection of cycle slips. However, its measurement noise is at the same level as pseudorange which is much (usually 100 times) larger than the carrier phase level. Furthermore, its ambiguity determination requires geometric information. Therefore, the Melbourne-Wübbena combination is normally not used for parameter estimation in high-accuracy applications. Instead, carrier phase and pseudorange observations are processed separately. That is

$$\Phi_{IF}^{p}(t) = \frac{f_1^{\,2}}{f_1^{\,2} - f_2^{\,2}} \Phi_1^{p}(t) - \frac{f_2^{\,2}}{f_1^{\,2} - f_2^{\,2}} \Phi_2^{p}(t) \tag{2.16}$$

and

$$P_{IF}^{p}(t) = \frac{f_1^{\,2}}{f_1^{\,2} - f_2^{\,2}} P_1^{p}(t) - \frac{f_2^{\,2}}{f_1^{\,2} - f_2^{\,2}} P_2^{p}(t) \tag{2.17}$$

where $\Phi_{IF}^{p}(t)$ and $P_{IF}^{p}(t)$ are the ionosphere-free carrier phase and pseudorange combinations of satellite p, respectively. Equations (2.16) and (2.17) can be expanded using equations (2.5) – (2.8)

$$\begin{aligned}\Phi_{IF}^{p}(t) = {} & \rho^{p}(t) + cdt(t) - cdt^{p}(t) + T^{p}(t) + d_{ant}^{p} + d_{rot}(t) + d_{rel}(t) \\ & + d_{otl}(t) + d_{set} + d_{windup} + N^{*p}_{IF} + \varepsilon^{p}_{\Phi 1,\Phi 2}\end{aligned} \tag{2.18}$$

$$\begin{aligned}P_{IF}^{p}(t) = {} & \rho^{p}(t) + cdt(t) - cdt^{p}(t) + T^{p}(t) + d_{ant}^{p} + d_{rot}(t) + d_{rel}(t) \\ & + d_{otl}(t) + d_{set} + \varepsilon^{p}_{P1,P2}\end{aligned} \tag{2.19}$$

N^{*p}_{IF} in equation (2.18) represents the combined ambiguity of ionosphere-free carrier phases

for satellite p and it can be expressed as $N^{*p}_{IF} = \frac{c}{f_1^2 - f_2^2}\left(f_1 N^{*p}_1 - f_2 N^{*p}_2 \right)$. Obviously it is not an integer. It should be noted that in PPP processing, satellite orbits, clocks and EOPs are introduced from external sources. Therefore, accuracies and consistencies of those products are of utmost importance to reach high accuracy. Real-time PPP is applicable only when real-time products of orbits, clocks and EOPs are available. The recently released RTS products by RTWG since March 2013 make real-time PPP possible and this research is conducted in this context.

2.6.2 Differential Positioning

GNSS observations from pairs of receivers and satellites can be differenced, which is widely used to eliminate satellite and receiver clock errors. Single-difference in terms of receivers (i, j) and satellite k is defined as

$$\begin{aligned} \Delta\Phi_{ij}^{k} &= \Phi_i^k - \Phi_j^k \\ \Delta P_{ij}^{k} &= P_i^k - P_j^k \end{aligned} \tag{2.20}$$

where operator Δ donates single-difference. A double-difference is the difference between two single-differences. To form a double-difference observation for two satellites (k,l) and two stations (i, j), the first step is to form single-differences between the two receives, while the second step is further difference between the two single-differenced observations formed from the previous step:

$$\begin{aligned} \nabla\Delta\Phi_{ij}^{kl} &= \Phi_{ij}^k - \Phi_{ij}^l \\ \nabla\Delta P_{ij}^{kl} &= P_{ij}^k - P_{ij}^l \end{aligned} \tag{2.21}$$

where operator ∇Δ donates double-difference. Equation (2.21) can be expanded using

equations (2.5) – (2.8)

$$\begin{aligned} \nabla\Delta\Phi_{ij}^{kl} &= \Delta\rho_{ij}^{kl} + \Delta T_{ij}^{kl} + \Delta N_{ij}^{kl}\frac{c}{f_{ij}^{kl}} + \Delta\varepsilon_{\varphi ij}^{kl} \\ \nabla\Delta P_{ij}^{Kl} &= \Delta\rho_{ij}^{kl} + \Delta T_{ij}^{kl} + \Delta\varepsilon_{Pij}^{kl} \end{aligned} \tag{2.22}$$

where ΔT_{ij}^{kl} represents the difference of signal path delays between station i and j and ΔN_{ij}^{kl} represents the difference of ambiguity between these two stations and two satellite k and l. f_{ij}^{kl} is the frequency of the combined carrier phase. It should be noted that receiver clock offsets are eliminated through double-difference. The double-difference processing is also not significantly affected by the accuracies and consistencies of external products. Therefore, double-difference has been widely used in the previous GNSS-MET applications as is mentioned in Chapter 1. However, with continuous refinement of satellite orbits, clocks and EOPs, currently PPP is also able to provide high-accuracy positions, tropospheric delays and other products.

2.7 Advantages of PPP against Double-difference for the Retrieval of PWV

According to the observation equation discussed previously, the PPP approach has its unique advantages against double-difference. In PPP all the GPS observations are used for calculations while in double-difference only the simultaneous observations from the same pair of two stations and two satellites are considered. In addition, in PPP there is no need of reference stations. Hence GPS data from each station is processed independently and data processing time is linearly proportional to the number of GPS stations. This is an advantage when a large amount of GPS data is processed and multi-thread processing is adopted. Furthermore, the epoch solutions in double-difference are only available at the epochs when double-difference observations exist. Therefore, PPP is potentially more promising for the particular application

of real-time retrieval of tropospheric dealys and the corresponding PWVs, as long as it is able to achieve equivalent accuracies. This research is to investigate the application of this novel technique of PPP in GNSS-MET.

2.8 Summary

This chapter provides a comprehensive background of GNSS positioning in the context of multi-GNSS. As is known new GNSSes have been emerging in the past few years. This has potential to improve the accuracy and reliability of GNSS positioning and the retrieval of ZTD and PWV. However, due to the lack of observations, real-time satellite orbits and clocks of newer GNSSes such as BDS, Galileo, QZSS and IRNSS, this research of GNSS-MET only use GNSS data from GPS and GLONASS.

The ground infrastructure over all scales – global, national, state-wide and local regions is of great significance to the applications of GNSS. IGS is a voluntary federation of more than 200 worldwide agencies and the highest-precision international civilian GNSS community. It provides not only raw GNSS measurements but also precise products such as satellite orbits, clocks, ZTDs, and so on. For this study the real-time orbit and clock corrections generated based on IGS network by BKG is used in PPP processing while the ZTD products from two IGS analysis centres (i.e., USNO and CODE) are used as reference data to validate the retrieved ZTDs.

This chapter also introduces observation equations and the corresponding linearisations. In GNSS positioning raw pseudorange and phase observations are usually linearly combined for various purposes. This includes the elimination of ionospheric delay, and the detection and determination of cycle slips, etc. The ionosphere-free combination is particularly important as it constitutes the functional model of PPP in this study. According to the formulae for the two positioning modes, i.e., PPP and double-difference, we can conclude that PPP has a higher accuracy demand of introduced satellite orbits, clocks and EOPs. It is not until the release of

IGS RTS produces that real-time PPP became applicable. However once such high-accuracy products are available and PPP is enabled, the PPP approach shows its unique advantages against double-difference. This includes no requirement of simultaneous observations from the same pair of two stations and two satellites, no requirement of reference stations, reasonable data processing time which is linearly proportional to the number of stations, along with the capability of providing high-resolution epoch-by-epoch solutions. All those advantages of PPP lead to the selection of this approach for the real-time retrievals of ZTD and PWV in this research.

In PPP processing, the ZTD is taken as one of the parameters to be estimated. The obtained ZTD can then converted into PWV, which is a complex process requires a good understanding of the background of GNSS-MET. The fundamentals of GNSS-MET are discussed later in Chapter 3.

Chapter 3. Fundamentals of Ground-based GNSS Meteorology

This chapter presents an overview of the fundamentals of ground-based GNSS-MET technology. Firstly, the atmosphere structure, i.e., different layers of atmosphere is introduced. In neutral atmosphere, the propagation of GNSS signals is affected by the slowing and bending effects. This tropospheric path delay can be derived using atmospheric refractivity. In GNSS data processing the tropospheric path delay is often divided into a hydrostatic part and a wet part. Both parts can be mapped from a vertical component using a mapping function to facilitate data processing. In GNSS-MET, tropospheric delays and PWV are of interest at the end of the data processing. While tropospheric delays can be directly obtained in GNSS data processing, the calculation of PWV involves zenith wet delay and a dimensionless constant of proportionality along with various empirical models.

3.1 Atmosphere Layers

The solid Earth is surrounded by gases which constitute the atmosphere. Most of the atmosphere (about 80%) is within 16 km of the surface of the Earth. There is no exact place where the atmosphere ends. It just gets thinner and thinner, until it merges with outer space. The atmosphere of the Earth can be divided into several distinct layers, thereby facilitating specific scientific research such as weather forecasting, global warming, space weather, and so on. Figure 3.1 displays the heights of ionosphere, mesosphere, stratosphere and troposphere.

The troposphere is the lowest layer of the Earth’s atmosphere which extends from the Earth's surface to a height of 9-18 km depending on altitude and weather variations [*Sturman and Tapper*, 2006]. It contains 99% of water vapour and aerosols. The weather and clouds occur in this layer. The stratosphere extends between 18 and 50 kilometres above the Earth's surface. Air flow in the stratosphere is mostly horizontal. Ozone, a particularly reactive form of oxygen

protecting human from ultraviolet radiation, is located in this layer. Above the stratosphere is the mesosphere which extends from 50 to 80 km. The temperature drops to about -100 ℃ in this layer hence it is the coldest region of the atmosphere. This layer protects the Earth from meteoroids which burn up in this area. The ionosphere starts at a height about 70-80 km and continues for hundreds of kilometres. It is therefore assumed that the ionosphere has an average height of 350 km [*Xu*, 2007]. It contains many ions and free electrons (plasma) which are created when sunlight hits atoms and tears off some electrons. The ionosphere layer reflects radio waves, which makes long-distance radio communication possible.

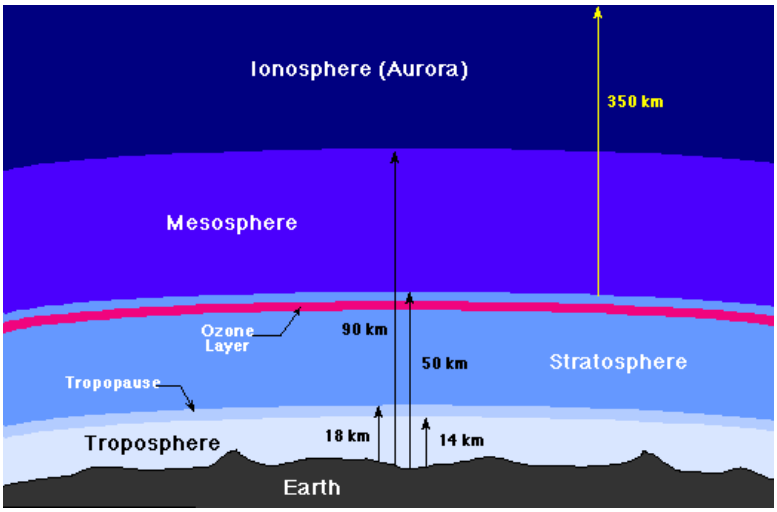

Figure 3.1 Layers of the atmosphere surrounding the Earth [*University of Tennessee,* 2014]

GPS signals are bent by ionosphere and troposphere when they propagate from satellites to receivers. The first order of ionospheric effect can be eliminated using ionosphere-free combinations if dual frequencies are available. This is because the ionosphere is a dispersive medium, i.e. the ionospheric effect is frequency dependent [*Xu*, 2007; *Yan et al.*, 2014]. However, unlike the ionosphere, the troposphere is a non-dispersive medium at GPS carrier frequencies. In other words, the tropospheric effects on the GPS signal propagation are independent from the GPS frequencies. To eliminate the tropospheric delay in GPS positioning or to determine the value of tropospheric delay for meteorological applications i.e. GPS-MET in this research, *a priori* models either empirical or derived using metrological data need to be

implemented.

3.2 Path Delay and Refractivity

3.2.1 Path Delay in the Atmosphere

The propagation speed v of GPS signals in the atmosphere can be expressed as

$$v = \frac{c}{n} \tag{3.1}$$

where n is the refractive index. Usually it is expressed as $n = c_0 / c$ where c and c_0 are the speed of light in the atmosphere and the vacuum, respectively. n is a complex number. Its imaginary part relates to the absorption of signals whereas the real part relates to the delay and bending [*Hall et al.*, 1996].

According to Snell's law, if we consider the neutral atmosphere to be horizontally stratified,

$$n_i \sin z_i = n_{i+1} \sin z_{i+1} \tag{3.2}$$

where z_i and z_{i+1} are the zenith angles of the arriving radio signal in layers i and $i+1$. n_i and n_{i+1} are the corresponding refractive indexes. Although the refractive index n varies in different atmosphere pressure, temperature and relative humidity conditions, its value is close to one. This makes the so called atmospheric refractivity N (in mm/km, or ppm) more convenient to be used instead.

$$N = (n-1) \times 10^6 \tag{3.3}$$

The electro-magnetic (or optical) distance L of a GPS signal propagating along the path S through the atmosphere will be

$$L = \int c dt = \int \frac{c}{v} ds = \int_S n(s) ds \tag{3.4}$$

Let G be the straight distance of a GPS signal in the atmosphere. The atmospheric delay ΔL can be expressed as

$$\begin{aligned} \Delta L &= L - G \\ &= \int_S n(s) ds - G \\ &= \int_S [n(s) - 1] ds + \int_S ds - G \\ &= 10^{-6} \int_S N(s) ds + S - G \end{aligned} \tag{3.5}$$

As such ΔL contains two parts. Firstly, the travelling speed of GPS signal in a region of finite density is slower than it would in a vacuum [*Boehm and Schuh*, 2013]. This slowing effect is the first term on the right hand side of equation (3.5). The $S - G$ part of equation (3.5) is called bending effect due to the signal bending in response to the gradients in the index of refraction of the atmosphere. The bending effect is approximately 1 cm or less which is much smaller than the slowing effect. Normally the bending term is by convention considered to be part of the hydrostatic delay [*Kleijer*, 2004] which is discussed later in Section 4.1. It can also be determined by a ray tracing technique by *Norman et al.* (2012).

3.2.2 Calculation of Refractivity

In the troposphere, the refractivity N can be divided into dry and vapour parts according to [*Smith and Weintraub*, 1953]. That is

$$N = N_d + N_v \tag{3.6}$$

Where N_d and N_v are the refractivity of dry air and water vapour respectively. Equation (3.6) makes sense because the relative concentrations of the dry gases are approximately constant. It can be further expressed as a function of pressure, temperature, and humidity [*Smith and Weintraub*, 1953] for frequencies up to 20 GHz [*Thayer*, 1974]:

$$N_d = k_1 \frac{P_d}{T} Z_d^{-1} \tag{3.7}$$

$$N_v = [k_2 \frac{e}{T} + k_3 \frac{e}{T^2}] Z_v^{-1} \tag{3.8}$$

where P_d and e are the partial pressures of dry air and water vapour in $\mathrm{N\,m^{-2}}$. T is the tropospheric temperature. Z_d and Z_v are the compressibility factors of dry air and water vapour, respectively. k_1, k_2 and k_3 are three empirically derived constants.

Empirical values of constants k_1, k_2 and k_3 have been investigated in different studies as is shown in Table 3.1. The constant k_1 is practically dependent on the relative concentrations of atmospheric gases. Most dry gases have stable concentrations with only the concentration of carbon dioxide showing a significant variation. As such the value of k_1 varies in different carbon dioxide concentration conditions. *Rüeger* (2002) computed the k_1 constant when the carbon dioxide concentrations are 375 ppm (for year 2004 case) and 392 ppm (for 2012 case). The values of 77.6900 $\mathrm{K.hPa^{-1}}$ for k_1, 71.2952 $\mathrm{K.hPa^{-1}}$ for k_2 and 375463 $\mathrm{K^2.hPa^{-1}}$ for k_3 respectively are adopted in this investigation.

Table 3.1 Empirical values of constants k_1, k_2 and k_3 according to different publications

Sources	k_1 (K.hPa^{-1})	k_2 (K.hPa^{-1})	k_3 (K^2.hPa^{-1})
[*Smith and Weintraub*, 1953]	77.6100	72.0000	375000
[*Boudouris*, 1963]	77.5900	72.0000	375000
[*Thayer*, 1974]	77.6000	64.7900	377600
375 ppm CO_2 [*Rüeger*, 2002][1]	77.6890	71.2952	375463
392 ppm CO_2 [*Rüeger*, 2002][1]	77.6900	71.2952	375463

[1] [*Rüeger*, 2002] gives two values of k_1 with regard to different carbon dioxide concentrations.

The compressibility factors in equation (3.7) and (3.8) are given by

$$Z_d = \frac{PM_d}{\rho_d RT} \tag{3.9}$$

and

$$Z_v = \frac{PM_v}{\rho_v RT} \tag{3.10}$$

where P and T are the tropospheric pressure and temperature respectively; M_d and M_v are the molar mass of dry air and water vapour with values 0.028964 kg.mol^{-1} and 0.018016 kg.mol^{-1}, respectively; ρ_d and ρ_v are the densities of dry air and water vapour, respectively; R is the gas constant with recommended value 8.3144621±0.0000075 J.K^{-1}.mol^{-1} according to [*Mohr et al.*, 2012]. Obviously for an ideal gas the compressibility factor is 1. The inverse compressibility factors can also be given by the empirical formulas. A widely used model using a least squares fitting to thermodynamic data by *Owens* (1967) is

$$Z_d^{-1} = 1 + P_d[57.97 \cdot 10^{-8}(1 + \frac{0.52}{T}) - 9.4611 \cdot 10^{-4} \frac{T - 273.15}{T^2}] \tag{3.11}$$

$$\begin{aligned} Z_v^{-1} = 1 + 1650\frac{e}{T^3}[1 - 0.01317(T - 273.15) \\ + 1.75 \cdot 10^{-4}(T - 273.15)^2 + 1.44 \cdot 10^{-6}(T - 273.15)^3] \end{aligned} \tag{3.12}$$

Moist air contains both dry gases and water vapour. Hence the density of moist air ρ_m is the

summation of the dry gas density ρ_d and the water vapour density ρ_v. With equations (3.7) and (3.8), along with the equations of state for dry air and water vapour, equation (3.6) can be expanded as

$$\begin{aligned} N &= k_1 R_d \rho_d + k_2 R_v \rho_v + k_3 \frac{e}{T^2} Z_v^{-1} \\ &= k_1 R_d \rho_m - k_1 R_d \rho_v + k_2 R_v \rho_v + k_3 \frac{e}{T^2} Z_v^{-1} \\ &= k_1 R_d \rho_m + (k_2 - k_1 \frac{R_d}{R_v}) R_v \rho_v + k_3 \frac{e}{T^2} Z_v^{-1} \\ &= k_1 \frac{R}{M_d} \rho_m + (k_2 - k_1 \frac{M_v}{M_d}) \frac{e}{T} Z_v^{-1} + k_3 \frac{e}{T^2} Z_v^{-1} \end{aligned} \tag{3.13}$$

where R_d and R_v are the specific gas constants of dry gases and water vapour, respectively. Let

$$k_2^{'} = k_2 - k_1 \frac{M_v}{M_d} \tag{3.14}$$

Then equation (3.13) becomes

$$\begin{aligned} N &= k_1 \frac{R}{M_d} \rho_m + (k_2^{'} \frac{e}{T} + k_3 \frac{e}{T^2}) Z_v^{-1} \\ &= N_h + N_w \end{aligned} \tag{3.15}$$

The first term N_h is called hydrostatic refractivity which depends only on the density of moist air ρ_m. The second term N_w is non-hydrostatic refractivity which is also called wet refractivity. N_w is dependent only on the partial pressure e of water vapour and temperature T.

3.3 Retrieval of PWV from GPS Derived Zenith Delays

3.3.1 Tropospheric Delays Derived from Refractivity

According to Section 3.2, instead of dividing the refractivity into dry and vapour parts following equations (3.6) – (3.8), we can also divide it into a hydrostatic and a wet part [*Davis et al.*, 1985] following equation (3.15). It should be noted that in the two cases dry refractivity N_d and hydrostatic refractivity N_h are not identical, as part of N_h is caused by water vapour. However, this separation of N_h and N_w will not affect but facilitate the calculation of the total refractivity N [*Boehm and Schuh*, 2013]. This is because the hydrostatic refractivity N_h can be simply calculated using surface pressure measurements as is discussed in Section 4.1.

Substituting equation (3.15) in equation (3.5) gives

$$\Delta L = 10^{-6}\int_S N_h(s)ds + 10^{-6}\int_S N_h(s)ds + S - G = \Delta L_h + \Delta L_w + S - G \tag{3.16}$$

where ΔL_h and ΔL_w are the hydrostatic and wet delay along the path S, respectively. The $S-G$ part is relatively small and usually considered to be part of the hydrostatic delay as is mentioned in Section 3.2.1.

As discussed previously, the atmospheric delay contains the ionospheric part and the tropospheric part. The former can be eliminated using ionosphere-free combinations and the latter contains the hydrostatic and wet delay. In GPS data processing, it is common that the tropospheric path delay of a signal is mapped from a vertical component using proper mapping functions. Normally mapping functions are elevation-dependent. As such, the corresponding tropospheric path delay becomes

$$\Delta L = z_t \cdot mf_t \tag{3.17}$$

$$\Delta L_h = z_h \cdot mf_h \tag{3.18}$$

$$\Delta L_w = z_w \cdot mf_w \tag{3.19}$$

$$z_t = z_h + z_w \tag{3.20}$$

$$\Delta L = \Delta L_h + \Delta L_w = z_h \cdot mf_h + z_w \cdot mf_w \tag{3.21}$$

where

z_t represents ZTD in troposphere,

z_h represents ZHD in troposphere,

z_w represents ZWD in troposphere,

mf_t represents the total mapping function,

mf_h represents the hydrostatic mapping function,

mf_w represents the wet mapping function.

3.3.2 Conversion from ZTD to PWV

In ground-based GPS-MET, ZWD is derived from the GNSS processing (either in the PPP or double-difference approach), then converted to PWV by a dimensionless constant of proportionality Π :

$$PWV = z_w \cdot \Pi \tag{3.22}$$

ZWD can be estimated directly from GNSS data processing. It can also be derived when ZHD

is subtracted from ZTD. The latter approach is adopted in this research as ZHD can be provided by more sophisticated but more accurate models than the one used in GNSS data processing. More discussions about the handling of ZWD are conducted in Section 7.1.

According to [*Bevis et al.*, 1994; *Duan et al.*, 1996],

$$\Pi = \frac{10^6 M_w}{\rho R\left(k_2 - k_1 \frac{M_w}{M_d} + \frac{k_3}{T_m} \right)} \tag{3.23}$$

where ρ is the density of liquid water; T_m is weighted mean temperature of troposphere. Values of constants R, k_1, k_2, k_3, M_w, M_d discussed in Section 3.2.2 are adopted in this study.

Errors in Π are mainly caused by errors in T_m and the constants in equation (3.23). *Foelsche and Kirchengast* (2001) proved that the influence of errors in T_m is at least one order of magnitude larger than the errors introduced by the constants. The accurate calculation of T_m requires the vertical profiles of water vapour and temperature [*Davis et al.*, 1985]:

$$T_m = \frac{\int \left(\frac{e}{T} \right) dz}{\int \left(\frac{e}{T^2} \right) dz} \approx \frac{\sum_{i=1}^{N} \left(\frac{e_i}{T_i} \right) \Delta z_i}{\sum_{i=1}^{N} \left(\frac{e_i}{T_i^2} \right) \Delta z_i} \tag{3.24}$$

where both e and T extend from the surface to the top of the atmosphere. For this real-time retrieval of PWVs, the vertical profiles of water vapour and temperature are not available without external meteorological data. Hence several empirical models are compared in Section 7.2 and the proper ones are used in this research.

Figure 3.2 simply shows a general process of GNSS-MET. At the end of data processing PWV

will be retrieved. However, this process involves accurate modelling of tropospheric delays, accurate corrections of error sources in PPP, empirical models for weighted mean temperature and proportionality constant Π, as well as comprehensive result validation. After discussions in these aspects in next few chapters, a more detailed flow chart of GNSS-MET (i.e., figure 7.1) is displayed in Section 7.1.

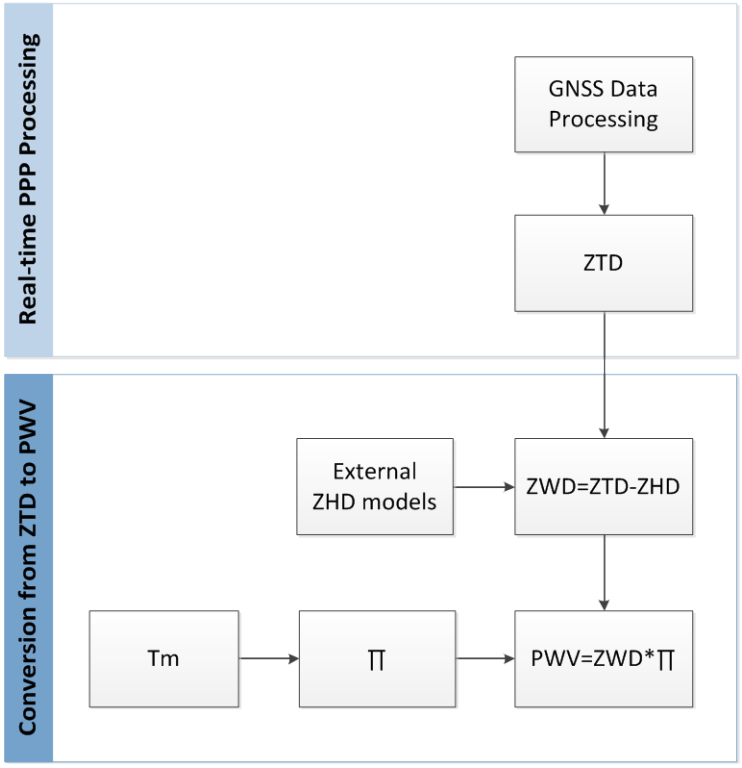

Figure 3.2 A flow chart of GNSS Meteorology

3.4 Summary

The refractivity can be divided into dry and vapour parts. Its calculation involves partial pressure of water vapour, surface temperature, and several constants. The refractivity can also be divided into hydrostatic and wet parts through a number of formula derivatives. This separation will not affect but facilitate the calculation of the total refractivity as the hydrostatic refractivity can be simply calculated using surface pressure measurements. Consequently, the signal path delay can be divided into hydrostatic and wet parts as it is the integral of the

refractivity. These tropospheric delays, including ZTD, ZHD and ZWD, are supposed to be derived from PPP processing in this research. The retrieved ZWD is then converted into PWV by multiplying a dimensionless constant of proportionality Π .

The accuracy of Π is critical for the retrieval of PWV. Its determination is dependent on several constants and variables using equation (3.24). It is concluded that the influence of variable T_m is at least one order of magnitude larger than that is introduced by the constants [*Boehm and Schuh*, 2013]. The accurate calculation of T_m requires the vertical profiles of water vapour and temperature, or accurate empirical models. This is further discussed in Chapter 7.

The next four chapters are presented following the flow chart of Figure 3.2. According this figure, the first stage of real-time PPP processing involves the modelling of tropospheric delays and error corrections. These two aspects are addressed in Chapter 4 and 5, respectively. The experimental results of PPP processing and corresponding validations are demonstrated in Chapter 6. The second stage of the flow chart involves empirical models for weighted mean temperature and proportionality constant Π , which is addressed in Chapter 7.

Chapter 4. Modelling of Tropospheric Delays in GNSS Positioning

This chapter discusses the modelling of tropospheric delays in PPP data processing, after the introduction of fundamentals of GNSS positioning and ground-based GNSS meteorology. The modelling of tropospheric delay includes the determination of ZHD, ZWD, ZTD and mapping functions. The ZTD in PPP processing is usually treated as the sum of ZHD and ZWD. The former is usually provided by an *a priori* value while the latter is a parameter to be estimated. Therefore, the determination of the *a priori* ZHD is critical as any error in this *a priori* value will be partly absorbed into the estimated ZWD. This requires the implementation of the latest models as well as proper validations using extern *in-situ* meteorological data.

4.1 Empirical Models for the Determination of Tropospheric Delays

4.1.1 ZHD

Integrating the hydrostatic refractivity N_h in vertical direction yields ZHD

$$z_h = 10^{-6} \int_{h_0}^{\infty} N_h(h) dh \tag{4.1}$$

where h_0 is the station height in metres above Mean Sea Level (MSL).

Substitution of the first term on the right side of equation (3.15) in equation (4.1) yields

$$z_h = 10^{-6} k_1 \frac{R}{M_d} \int_{h_0}^{\infty} \rho_m(h) dh \tag{4.2}$$

The hydrostatic equation under the condition of hydrostatic equilibrium is

$$\frac{dP}{dh} = -\rho_m(h)g(h) \tag{4.3}$$

where $g(h)$ is the gravity acceleration as a function of height above MSL. $g(h)$ can be replaced using a mean gravity g_m [*Saastamoinen,* 1972].

$$g_m = g_m^0 \cdot f(\phi, h_0) \tag{4.4}$$

where ϕ is the geodetic latitude and $g_m^0 = 9.784\ \mathrm{m \cdot s^{-2}}$. According to [*Davis et al.*, 1985],

$$f(\phi, h_0) = 1 - 0.00266\cos 2\phi - 0.00000028h_0 \tag{4.5}$$

Integrating equation (4.3) yields

$$\int_{P_0}^{0} dP = -\int_{h_0}^{\infty} \rho_m(h)g(h)dh = -g_m \int_{h_0}^{\infty} \rho_m(h)dh = -P_0 \tag{4.6}$$

where P_0 is the surface air pressure. As such

$$\int_{h_0}^{\infty} \rho_m(h)dh = \frac{P_0}{g_m} \tag{4.7}$$

Substituting equation (4.7) into equation (4.2) gives

$$z_h = 10^{-6} k_1 \frac{R}{g_m M_d} P_0 \tag{4.8}$$

Using constant $g_m^0 = 9.784\ \mathrm{m \cdot s^{-2}}$ given in [*Davis et al.*, 1985] and equations (4.4) – (4.5), equation (4.8) can be re-written as (in metres)

$$z_h = 0.0022768 \frac{P_0}{f(\phi, h_0)} \tag{4.9}$$

So for any GPS station with known geodetic latitude and height, its corresponding ZHD can be calculated using equation (4.9) as long as the surface air pressure is given. Surface pressure can also be obtained from empirical models. A widely used pressure is [*Kouba*, 2009]

$$P_0 = 1013.25 \cdot (1 - 0.0000226 h_0)^{5.225} \tag{4.10}$$

Another widely used ZHD model is the UNB (University of New Brunswick) model. It utilises the Saastamoinen zenith delays (as modified by [*Davis et al.*, 1985]) and a look-up table with annual mean and amplitude for temperature, pressure, and relative humidity varying with respect to latitude and propagated to station height [*Leandro et al.*, 2008].

According to previous studies [*Davis et al.*, 1985; *Boehm and Schuh*, 2013], the main errors in equation (4.9) include:

1) an error of 1 hPa in surface air pressure is likely to cause an error of approximately 2.2768 mm in the resultant ZHD. So in order to reach an accuracy of 0.1 mm in ZHD, the surface pressure needs to be as accurate as 0.05 hPa. This accuracy level is challenging for most of the empirical pressure models.

2) the coefficient 0.0022768 is calculated using several constants. Its accuracy is $0.0005\ \mathrm{m \cdot bar^{-1}}$ and the error is mainly caused by k_1 [*Davis et al.*, 1985].

3) equation (4.9) is based on the assumption of hydrostatic equilibrium depending on the wind, which may cause an error of 20 mm in ZHD under severe weathers.

4.1.2 ZWD

The determination of ZWD is based on wet refractivity. According to equation (3.15),

$$N_w = (k_2^{'} \frac{e}{T} + k_3 \frac{e}{T^2}) Z_v^{-1} \tag{4.11}$$

Integrating equation (4.11) along the propagation path yields ZWD

$$z_w = 10^{-6} [\int_{h_0}^{\infty} (k_2^{'} \frac{e}{T} Z_v^{-1}) dh + \int_{h_0}^{\infty} (k_3 \frac{e}{T^2} Z_v^{-1}) dh] \tag{4.12}$$

Obviously partial pressure e of water vapour and surface temperature T as functions of height are needed to calculate ZWD. It should be noted that due to the high variability and unpredictability of water vapour, the determination of ZWD is far more challenging than that of ZHD [*Boehm and Schuh*, 2013]. In this study, besides the *a priori* ZHD and ZWD, an additional parameter is setup to account for the residual ZWD. For the calculation of the *a priori* ZWD, *Saastamoinen* (1972) used an empirical model

$$z_w = 0.0022768(1255 + 0.05T) \frac{e}{T} \tag{4.13}$$

Other empirical models can be used and found in the literature [*Hopfield*, 1969; *Askne and Nordius*, 1987; *Baby et al.*, 1988; *Mendes and Langley*, 1999].

4.1.3 ZTD

For the determination of ZTD, there are also several empirical models. *Saastamoinen* (1972,

1973) proposed a model:

$$z_t = \frac{0.002277}{\sin E}[P_0 + (\frac{1255}{T} + 0.05)e - B\cot^2 E] + \delta R \tag{4.14}$$

where E is the elevation angle of the GPS signal; B and δR are the tabulated functions of station height h_0 and elevation angle E; R_h is relative humidity (in %). Some other empirical ZTD models can be found in the literature [*Hopfield*, 1971; *Chao*, 1974].

4.2 External Meteorological Data for the Determination of Tropospheric Delays

4.2.1 Meteorological Data Files in RINEX Format

The accurate modelling of tropospheric delays discussed in Section 4.1 requires meteorological measurements such as surface pressure, temperature, partial pressure of water vapour and relative humidity. The surface pressure data is particularly useful to obtain high-accuracy *a priori* ZHD using equation (4.9). To facilitate high-accuracy positioning, some GPS stations have collocated meteorological sensors like barometers and thermometers. Such meteorological data can be recorded as one of several Receiver Independent Exchange Format (RINEX) files which are widely used in GNSS community. Currently the RINEX format includes the following meteorological observation types [*Gurtner and Estey*, 2009]:

PR: Pressure (in mbar);

TD: Dry temperature (in Celsius degree);

HR: Relative humidity (in percent);

ZW: Wet zenith path delay (in mm), for water vapour radiometer (WVR);

ZD: Zenith hydrostatic delay (in mm);

ZT: Zenith total delay (in mm);

WD: Wind azimuth (in degree) from where the wind blows;

WS: Wind speed (in m/s);

RI: Rain accumulation since last measurement (in 1/10 mm);

HI: Hail detected since last measurement.

An example of meteorological file in RINEX Version 3.01 is shown in Figure 4.1.

```
+------------------------------------------------------------------------------+
|                                TABLE A15                                     |
|                     METEOROLOGICAL DATA FILE - EXAMPLE                       |
+------------------------------------------------------------------------------+

----|---1|0---|---2|0---|---3|0---|---4|0---|---5|0---|---6|0---|---7|0---|---8|

     3.01           METEOROLOGICAL DATA                     RINEX VERSION / TYPE
XXRINEXM V9.9       AIUB                 1996-04-02 00:10:12 PGM / RUN BY / DATE
EXAMPLE OF A MET DATA FILE                                   COMMENT
A 9080                                                       MARKER NAME
     3    PR    TD    HR                                    # / TYPES OF OBSERV
PAROSCIENTIFIC      740-16B                      0.2    PR SENSOR MOD/TYPE/ACC
HAENNI                                           0.1    TD SENSOR MOD/TYPE/ACC
ROTRONIC            I-240W                       5.0    HR SENSOR MOD/TYPE/ACC
        0.0           0.0           0.0        1234.5678 PR SENSOR POS XYZ/H
                                                           END OF HEADER
 96  4  1  0  0 15  987.1   10.6   89.5
 96  4  1  0  0 30  987.2   10.9   90.0
 96  4  1  0  0 45  987.1   11.6   89.0

----|---1|0---|---2|0---|---3|0---|---4|0---|---5|0---|---6|0---|---7|0---|---8|
```

Figure 4.1 An example of meteorological data file in RINEX Version 3.01. This file includes three types of data: surface pressure, dry temperature and relative humidity. Data is recorded at an interval of 15 seconds.

4.2.2 Meteorological Data from Weather Stations

Weather stations record a variety of weather phenomena and parameters, including temperature, humidity, rainfall, pressure, sunshine, wind, cloud and visibility. The recorded data includes synoptic, AWS (Automatic Weather Station), radiosonde measurements, and so on.

Some meteorological measurements like air temperature, humidity, wind, cloud and pressure may need to be recorded frequently, e.g. three-hourly or half-hourly. In that case AWS data is

particularly important to automatically record and send the measurements (mostly electronically). In addition, they generate a report when certain conditions of wind, rain, temperature or barometer changes occur, in order to monitor severe or unusual weather. There are many other measurements which are not taken so frequently but with more details. They may also be recorded by human observers at several hundred stations manually in a country.

For the determination of zenith delays discussed in Section 4.1, normally the surface pressure P, temperature T and relative humidity R_h need to be interpolated to the location of the GPS station when weather station and GPS station are not co-located. One approach is the linear interpolation using measurements from several surrounding weather stations [*Bosy et al.*, 2012]. The value of a particular parameter is calculated as a weighted average:

$$\bar{s} = \frac{\sum_{i=1}^{n} s_i \omega_i}{\sum_{i=1}^{n} \omega_i} \tag{4.15}$$

where s_i represents one of the parameters (P, T and R_h) and $\bar{s}$ is the corresponding result of the equation. ω_i is the weighting coefficient. At any of the selected surrounding stations, the corresponding values of ω_i in terms of P, T and R_h are treated differently [*Bosy et al.*, 2012].

Besides AWS, another type of weather stations is radiosonde. The radiosonde balloons are released two to four times per day in multiple locations. *In-situ* atmospheric parameters are collected as the balloons ascend. The radiosonde data is available from a repository of atmosphere profiles provided by the National Oceanic and Atmospheric Administration (NOAA, *http://www.esrl.noaa.gov/raobs/*). Pressure P, temperature T and partial pressure e of water vapor from the radiosonde profiles can be used to calculate PWVs, which are used as reference data to validate the PWVs retrieved from the real-time PPP technique in this research.

4.2.3 Meteorological Data from NWP Models

NWP models predict the weather based on current weather conditions using mathematical models of the atmosphere and oceans. NWP models can be used to generate short-term weather forecasts. It is important for longer-term climate predictions which are widely applied for understanding and projecting climate change. A good example of operational NWP model is the ACCESS model used by the Australian Bureau of Meteorology. The ACCESS data is in a digital gridded binary format i.e. GRIB edition 2 and NetCDF-4 [*Puri*, 2010]. Another widely used is the European Centre for Medium-Range Weather Forecasts (ECMWF) which is established in 1975 and supported by 34 member states [*Molteni et al.*, 1996].

NWP models provide almost all sorts of meteorological parameters. For a specific pressure layer i, the pressure P_i, temperature T_i and relative humidity $(R_h)_i$ are available and can be used in the GNSS data processing, i.e., equation (4.8) can be re-written to determine ZHD:

$$z_h = 10^{-6} k_1 \frac{R}{M_d} \sum_i \frac{1}{g_i} \Delta P_i \tag{4.16}$$

where g_i is the gravity and ΔP_i is the difference of pressure for two consecutive layers. ZWD can also be determined [*Kleijer*, 2004] using equation

$$z_w = 10^{-6} \frac{R}{M_w} \sum_i (k_2^{'} + \frac{k_3}{T_i}) \frac{(R_h)_i}{g_i} \Delta P_i \tag{4.17}$$

NWP data is also useful to determine the weighted mean temperature T_m following equation (3.23). This will significantly improve the accuracy of T_m for the conversion from ZWD to PWV.

4.3 Empirical Mapping Functions

According to the expressions of path delays in equations (3.17) – (3.19), mapping functions are approximately equal to $1/\sin(E)$. However, the determination of mapping functions in reality is far more complex due to the bending and slowing effects in the atmosphere. The accuracies of mapping functions are vital in high-accuracy positioning applications. This is because zenith delays, station heights, and clocks in GPS observation equations (2.18) and (2.19) are highly correlated. Any error of in mapping functions will result in corresponding errors in the station height and clock estimates.

The simple formula $1/\sin(E)$ is used as a total mapping function in the original BNC software for PPP processing. However the PPP module of the original BNC software has limitations and has only been developed for demonstration. This means that the accurate modelling of mapping functions needs to be carefully considered. An earlier study by *Marini* (1972) suggests that the total mapping function can be written as

$$mf_t(E) = \frac{1}{\sin(E) + \dfrac{0.00085599}{\sin(E) + \dfrac{0.0021722}{\sin(E) + \dfrac{0.0060788}{\sin(E) + 0.11571}}}} \tag{4.18}$$

Chao (1974) for the first time suggests that mapping functions for the hydrostatic and wet parts should be different and one of the $\sin(E)$ expressions in equation (4.18) can be replaced by $\tan(E)$:

$$mf_h = \frac{1}{\sin(E) + \dfrac{a_h}{\tan(E) + b_h}} \tag{4.19}$$

$$mf_w = \frac{1}{\sin(E) + \dfrac{a_w}{\tan(E) + b_w}} \tag{4.20}$$

where $a_h = 0.00143$, $b_h = 0.0445$, $a_w = 0.00035$ and $b_w = 0.0170$. The term $\tan(E)$ in the equations is used to ensure that both hydrostatic and wet mapping functions are equal to 1 in the zenith direction. The corresponding ZHD and ZTD by *Chao* (1974) are calculated using Equation (4.8) and (4.14) [*Saastamoinen*, 1972; *Saastamoinen*, 1973].

Based on the work by *Chao* (1974) but with improved accuracy at low elevation angles, *Davis et al.* (1985) developed a new mapping function by introducing a third constant c:

$$mf(E) = \frac{1}{\sin(E) + \dfrac{a}{\tan(E) + \dfrac{b}{\sin(E) + c}}} \tag{4.21}$$

This model is called CfA2.2. The three constants are determined as functions of pressure P (in mbar), partial pressure of water vapour e (in mbar), and temperature T_0 (in degrees Celsius) at the Earth's surface by ray tracing analyses for various atmospheric conditions. It should be noted that for hydrostatic and wet parts, the mapping functions are different. The CfA2.2 model has been widely used in space geodesy for a long time due to its simplicity. Its disadvantage is that $\tan(E)$ does not approach $\sin(E)$ quickly enough when the elevation angles are between 20° and 60°. Consequently, a corresponding error of 1-2 mm in representing the atmospheric delays is expected [*Davis et al.*, 1985].

Herring (1992) developed the MTT (MIT Temperature) mapping function which is slightly different from equation (4.19) – (20). That is:

$$mf(E) = \frac{1 + \dfrac{a}{1 + \dfrac{b}{1 + c}}}{\sin(E) + \dfrac{a}{\sin(E) + \dfrac{b}{\sin(E) + c}}} \tag{4.22}$$

where the three constants are determined as functions of latitude, height, and the surface temperature.

Based on equation (4.21), *Niell* (1996) presents the New Mapping Function (NMF). An advantage of NMF against MTT is that the three constants are functions of the day of the year (DOY), station latitude and station height above the mean sea level. This makes it widely used in earlier GPS applications. To further refine the NMF model, *Niell* (2000) re-determined the constant c using NWP data and proposed the Isobaric mapping function (IMF). Another work based on NMF is the UNB model which provides improved hydrostatic and wet mapping functions [*Leandro et al.*, 2008]. The input parameters for UNB are DOY, latitude, height above MSL and elevation angle.

It should be noted that the mapping function models presented earlier have their own disadvantages either in seasonal terms, or with deficiencies in certain areas [*Boehm et al.*, 2006b]. However, based on the earlier studies, new mapping functions depending on operational NWP data are developed. Recently two widely used models are VMF1 and GMF, both of which are implemented in this study.

4.4 VMF1 Model and Its Implementation

4.4.1 Advantages and Disadvantages of the Classical Separation of Hydrostatic and Wet Mapping Functions

VMF1 was initially proposed by *Boehm et al.* (2006b) based on the previous VMF model [*Boehm and Schuh*, 2004] and the mentioned IMF model [*Niell*, 2000]. The hydrostatic, wet and total mapping functions are all considered using the same expression of equation (4.22). Each mapping function depends on different sets of constants a, b and c. Those constants are determined using the 40-year period ECMWF Re-Analysis (ERA-40) data [*Uppala et al.*,

2005].

Normally if equation (3.21) is used for the modelling of tropospheric delays in GNSS data processing, an extra parameter Δz_w is needed to account for the residual ZWD as ZWD varies rapidly and significantly. The path delay becomes

$$\Delta L = z_h \cdot mf_h + (z_w + \Delta z_w) \cdot mf_w \tag{4.23}$$

Obviously the hydrostatic mapping function is different from the wet mapping function, particularly for low elevation angles. As such the ZHD should be fairly accurate. Otherwise any error in ZHD cannot be fully absorbed into the parameter Δz_w. Consequently, the retrieved ZTD, station coordinates and receiver clocks will not be accurate. These errors are called hydrostatic/wet mapping separation errors [*Kouba*, 2009]. When the cutoff elevation is as low as 5°, the error in station height can be one third of the error in ZHD at the cutoff elevation angle according to a rule of thumb [*Niell et al.*, 2001].

The hydrostatic/wet mapping separation error can be overcome if a total mapping function is used. The retrieved ZTDs will then not be affected by poor *a priori* ZHD values. Nonetheless, it should be noted that the total mapping function mf_t is close to the hydrostatic mapping function mf_h. Hence the rapid variation of the residual ZWD cannot be accounted for, let alone VMF1 data is updated every 6 hours. This disadvantage makes the total mapping function not an ideal model for the retrieval of ZWD and PWV in this research. So the classical separation of path delay into hydrostatic and wet parts is used in this research.

4.4.2 VMF1 Dataset

The Vienna University of Technology provides the VMF1 data which is available online (*http://ggosatm.hg.tuwien.ac.at/DELAY/*) for the implementation in GNSS applications.

Currently several types of data in terms of different latencies and GNSS stations are provided. For the selected IGS stations, VMF1 Site dataset provides station-specific parameters such as ZHD, ZWD, a_h and a_w. For other stations, Gridded VMF1 dataset is provided and users need to do an interpolation to obtain the corresponding parameters for a specific location. For real-time applications, Forecast VMF1 (VMF1-FC) files are provided and users need to perform an interpolation to obtain the corresponding parameters for the current epoch.

An alternative dataset for VMF1 is provided by the University of New Brunswick (UNB-VMF1). Their parameters are determined using a similar approach as is done by the Vienna University of Technology, based on data of the National Centres of Environmental Prediction (NCEP) and the Canadian Model (CMC). UNB-VMF1 dataset is available online at *http://unb-vmf1.gge.unb.ca/Products.html*.

4.4.3 Implementation of VMF1 Site

The stations included in VMF1 Site dataset are listed in file *http://ggosatm.hg.tuwien.ac.at/DELAY/SITE/gnss.ell*. The four-character name, latitude, longitude, ellipsoid height and domes number are used for the station identifications. The VMF1 Site coefficients are updated with a latency of less than 34 hours. A typical VMF1 Site file named 2014307.vmf1_g is partly listed in Figure 4.2. As can be seen, The VMF1 coefficients are provided as discrete values at a 6-hour interval. The record types for the 11 columns are: Station name, modified Julian date, hydrostatic coefficient "a", wet coefficient "a", ZHD in meter, ZWD in meter, mean temperature in Kelvin (to convert the wet zenith delay into precipitable water), pressure at the site in hPa, temperature at the site in degree Celsius, water vapour pressure at the site in hPa, and the approximate orthometric height.

ABMF	56964.00	0.00127969	0.00055790	2.3125	0.1829	289.9	1013.32	26.35	27.48	15.9
ABMF	56964.25	0.00127663	0.00054279	2.3081	0.2048	290.3	1011.77	25.17	27.63	15.9
ABMF	56964.50	0.00127729	0.00054406	2.3091	0.2058	290.7	1011.94	26.00	28.81	15.9
ABMF	56964.75	0.00127749	0.00056038	2.3055	0.2205	290.0	1009.84	28.59	24.77	15.9
ABPO	56964.00	0.00124136	0.00049113	1.9360	0.1258	281.7	848.04	18.49	12.47	1553.5
ABPO	56964.25	0.00124398	0.00045577	1.9394	0.0943	284.3	849.79	21.71	9.83	1553.5
ABPO	56964.50	0.00124625	0.00045981	1.9312	0.0942	286.4	846.82	25.85	9.95	1553.5
ABPO	56964.75	0.00124379	0.00046517	1.9386	0.1081	283.9	849.63	21.52	12.49	1553.5
ADE1	56964.00	0.00125832	0.00059112	2.3162	0.0552	278.3	1015.65	20.74	6.89	39.0
ADE1	56964.25	0.00126162	0.00060452	2.3049	0.0464	280.2	1010.65	27.04	4.54	39.0
ADE1	56964.50	0.00126157	0.00062693	2.3033	0.0776	280.5	1009.91	24.52	4.89	39.0
ADE1	56964.75	0.00125909	0.00057936	2.2977	0.0679	282.7	1008.58	20.85	4.73	39.0
ADE2	56964.00	0.00125832	0.00059112	2.3162	0.0552	278.3	1015.65	20.74	6.89	39.0
ADE2	56964.25	0.00126162	0.00060452	2.3049	0.0464	280.2	1010.65	27.04	4.54	39.0
ADE2	56964.50	0.00126157	0.00062693	2.3033	0.0776	280.5	1009.91	24.52	4.89	39.0
ADE2	56964.75	0.00125909	0.00057936	2.2977	0.0679	282.7	1008.58	20.85	4.73	39.0
ADIS	56964.00	0.00122321	0.00040755	1.7454	0.0506	279.1	764.38	13.19	6.85	2446.6
ADIS	56964.25	0.00122338	0.00044448	1.7501	0.0610	277.5	766.88	13.01	6.79	2446.6
ADIS	56964.50	0.00122644	0.00044938	1.7401	0.0654	280.3	763.34	17.49	6.73	2446.6
ADIS	56964.75	0.00122568	0.00047076	1.7462	0.0629	278.2	765.19	15.37	5.82	2446.6
AIRA	56964.00	0.00125117	0.00048745	2.2391	0.1068	283.3	982.53	19.65	15.32	282.6
AIRA	56964.25	0.00124917	0.00050040	2.2455	0.1305	281.9	984.05	19.07	15.36	282.6
AIRA	56964.50	0.00125036	0.00051881	2.2455	0.1355	281.2	984.12	18.08	16.32	282.6
AIRA	56964.75	0.00124999	0.00052371	2.2479	0.1445	280.3	985.62	16.63	16.53	282.6

Figure 4.2 Contents in a VMF1 Site file 2014307.vmf1_g. This file does not contain any header information.

For the calculation of mapping functions using equation (4.22), a_h and a_w are extracted from the online dataset. The other four coefficients b_h, b_w, c_h and c_w are empirically determined [*Boehm et al.*, 2006b] and their values are

$$\begin{aligned} b_h &= 0.0029 \\ b_w &= 0.00146 \\ c_h &= c_0 + ((\cos(\frac{doy - 28}{365.25} \cdot 2\pi + \psi) + 1) \cdot \frac{c_{11}}{2} + c_{10}) \cdot (1 - \cos\varphi) \\ c_w &= 0.04391 \end{aligned} \tag{4.24}$$

where constants c_0, c_{10}, c_{11} and ψ are defined in Table 4.1. ψ is used to specify the Northern or Southern Hemisphere. Their values are given in Table 4.1.

Table 4.1 Constants used for the determination of VMF1 hydrostatic mapping function [*Boehm et al.,* 2006b]

Hemisphere	c_0	c_{10}	c_{11}	ψ
Northern	0.062	0.001	0.005	0
Southern	0.062	0.002	0.007	π

4.4.4 Implementation of VMF1-FC

The VMF1-FC files are provided for real-time applications in terms of four daily epochs (0, 6, 12, 18 h UT) on a global grid (2.0° x 2.5°). Two steps are needed to implement the VMF1-FC model for a specific station at the current epoch. The first step is the interpolation to the current epoch using consecutive files. In this study eight files (two days) in total are used. The eight files are selected and updated based on a sliding window, which ensures that no big jumps in values of the interpolated parameters occur. The cubic spline interpolation (as is implemented in this research) or Lagrange interpolation can be used in this step. The second step is the interpolation to the specific location using data from four neighbouring grid points.

Height corrections of mapping functions, ZHD and ZWD

Height is a concern in the second step of interpolation. The actual heights for the GNSS station and the four neighbouring grid points are different. Hence the extracted parameters such as a_h, a_w, ZHD and ZWD need to be corrected for the height difference between the gridded heights and the actual station height.

Since the gridded hydrostatic coefficients a_h are valid for zero heights, the corresponding height correction of hydrostatic mapping function to the actual station height h_0 (in meters) is

$$h_{corr} = \left(\frac{1}{\sin(E)} - \frac{1 + \dfrac{a_0}{\left(1 + \dfrac{b_0}{(1 + c_0)}\right)}}{\sin(E) + \dfrac{a_0}{\sin(E) + \dfrac{b_0}{\sin(E) + c_0}}} \right) \cdot \frac{h_0}{1000} \tag{4.25}$$

where $a_0 = 2.53 \times 10^{-5}$, $b_0 = 5.49 \times 10^{-3}$, $c_0 = 1.14 \times 10^{-3}$. This correction approach is for the first time presented by *Niell* (1996). The corrected hydrostatic mapping functions then become

$$mf_h = mf_h + h_{corr} \tag{4.26}$$

The gridded hydrostatic delay z_h and wet delay z_w correspond to the ellipsoidal heights. Those ellipsoid heights are given in file *orography_ell* which is available on the website (*http://ggosatm.hg.tuwien.ac.at/DELAY/GRID/orography_ell)*. The height correction for ZHD is [*Fund et al.*, 2009]:

$$z_h(s) = z_h(g) - 0.002277 \cdot \frac{g_m}{R} \cdot \frac{P(g)}{T(g)} \cdot (h(s) - h(g)) \tag{4.27}$$

where (s) and (g) denote the GNSS station and grid point, respectively; g_m is the gravity constant and $g_m = 9.784\ \mathrm{m \cdot s^{-2}}$; R is the gas constant with recommended value 8.3144621±0.0000075 $\mathrm{J.K^{-1}.mol^{-1}}$ [*Mohr et al.*, 2012]; P and T are pressure and temperature in hPa and K, respectively. For the height correction of ZWD, an empirical decay coefficient (-1/2000) obtained using data from an IGS station KOKB [*Kouba*, 2008] is used:

$$z_w(s) = z_w(g) \cdot e^{-(h(s)-h(g))/2000} \tag{4.28}$$

Bilinear interpolation using surrounding four gridded points

After the implementation of above height corrections, the surrounding four gridded parameters correspond to the station height. Another bilinear interpolation based on geodetic coordinates (latitude φ and longitude λ) is needed as is demonstrated in Figure 4.3.

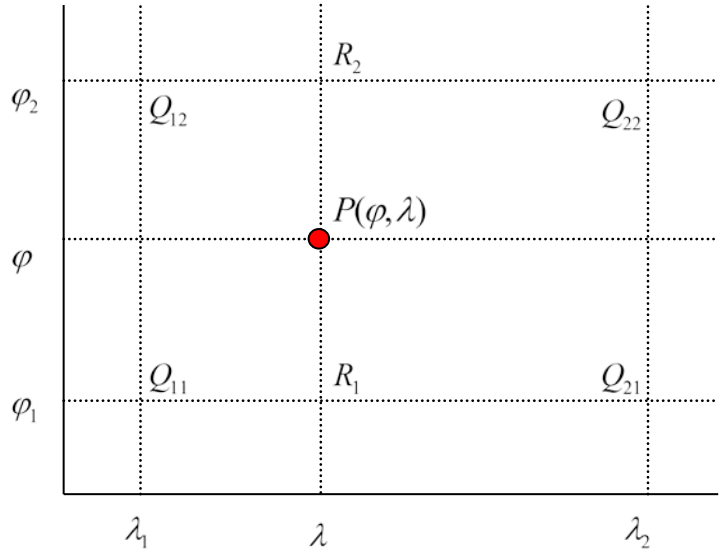

Figure 4.3 Bilinear interpolation of the gridded four parameters to the location (latitude φ and longitude λ) of the GNSS station. Algorithms are implemented in two directions: 1) in the longitude direction to obtain values at $R_1(\varphi_1,\lambda)$ and $R_2(\varphi_2,\lambda)$, and 2) in the latitude direction to obtain the values at the GNSS station.

Assume that 1) the station is $P(\varphi,\lambda)$; 2) the surrounding four grid points are $Q_{11}(\varphi_1,\lambda_1)$, $Q_{12}(\varphi_2,\lambda_1)$, $Q_{21}(\varphi_1,\lambda_2)$ and $Q_{22}(\varphi_2,\lambda_2)$; and 3) each parameter (a_h, a_w, z_h or z_w) at the four grid points are denoted as $f(Q_{11})$, $f(Q_{12})$, $f(Q_{21})$ and $f(Q_{22})$ respectively. The bilinear interpolation is first implemented in the longitude direction to obtain values at $R_1(\varphi_1,\lambda)$ and $R_2(\varphi_2,\lambda)$:

$$f(R_1)=\frac{\lambda_2-\lambda}{\lambda_2-\lambda_1}f(Q_{11})+\frac{\lambda-\lambda_1}{\lambda_2-\lambda_1}f(Q_{21}) \tag{4.29}$$

$$f(R_2) = \frac{\lambda_2 - \lambda}{\lambda_2 - \lambda_1} f(Q_{12}) + \frac{\lambda - \lambda_1}{\lambda_2 - \lambda_1} f(Q_{22}) \tag{4.30}$$

A further linear interpolation in latitude direction is followed to obtain the values $f(P)$ at station $P(\varphi, \lambda)$:

$$f(P) = \frac{\varphi_2 - \varphi}{\varphi_2 - \varphi_1} f(R_1) + \frac{\varphi_1 - \varphi}{\varphi_1 - \varphi_2} f(R_2) \tag{4.31}$$

4.5 GPT/GMF and GPT2

The implementation of VMF1-FC in real-time GNSS processing requires complex calculations and data downloading from the Internet. As a simplified model of VMF1, the Global Mapping Function (GMF) model is developed by the Vienna University of Technology [*Boehm et al.*, 2006a]. The coefficients of the GMF were obtained from an expansion of the VMF1 parameters into spherical harmonics on a global grid. The implementation of GMF is simple as only the station coordinates and DOY are needed as input.

Another simplification of VMF1 in terms of the determination of ZHD and ZWD is the empirical GPT model [*Boehm et al.*, 2007] which provides pressure and temperature at any site. ZHD can be determined accordingly using equation (4.9). GMF and GPT are often used together and proved to be ideal in real-time GNSS processing [*Kouba*, 2009; *Steigenberger et al.*, 2009].

An updated model of GPT/GMF called GPT2 is presented by *Lagler et al.* (2013). The updates mainly include more NWP data used, refined horizontal and height resolutions, refined temperature lapse rate, and extra semi-annual harmonics in order to better account for regions where very rainy periods or very dry periods dominate. It is stated that compared to GPT/GMF, GPT2 yields a 40% reduction of annual and semi-annual amplitude differences in station

heights [*Lagler et al.*, 2013]. The GPT2 subroutine is also provided (available at: *http://ggosatm.hg.tuwien.ac.at/DELAY/SOURCE/*) to calculate local values of ZHD, ZWD, hydrostatic and wet mapping functions. The input data includes the station coordinates and the observation epoch specified as the Modified Julian Date. It should be noted that the mapping function coefficients are already provided by GPT2. These mapping function coefficients are then input to the subroutine which is also used for VMF1-FC. More specifically, b_h, b_w, c_h and c_w for both GPT2 and VMF1-FC are the same, given by equation (4.24). a_h and a_w for GPT2 are derived from empirical models and those for VMF1-FC are derived from NWP data updated every six hours.

4.6 Validation of ZHD Using *In-situ* Meteorological Measurements

The calculation of ZHD is important in this study as it is implemented twice to retrieve PPP-PWV. Firstly, the *a priori* ZHD is indispensable for real-time PPP data processing. This requires that the model should be relatively less computationally demanding, as PPP processing needs to be implemented at high-resolutions and a large number of stations simultaneously, either for weather nowcasting or NWP models. In addition, for the conversion from ZTD to PWV, accurate ZHD is needed to obtain ZWD according to Section 3.3.2.

The ZHDs from the models mentioned above such as VMF1-FC, GPT2, UNB, Saastamoinen and Hopfield are validated using ZHDs derived from *in-situ* pressure measurements. Equations (4.5, 4.9, and 4.10) are used to calculate the reference ZHD data. Those pressure measurements are recorded in RINEX meteorological files and collected from the IGS stations where on-board barometers are available. For the period of September 2013, a total of 71 IGS stations meet this selection criterion and their distribution is displayed in Figure 4.4.

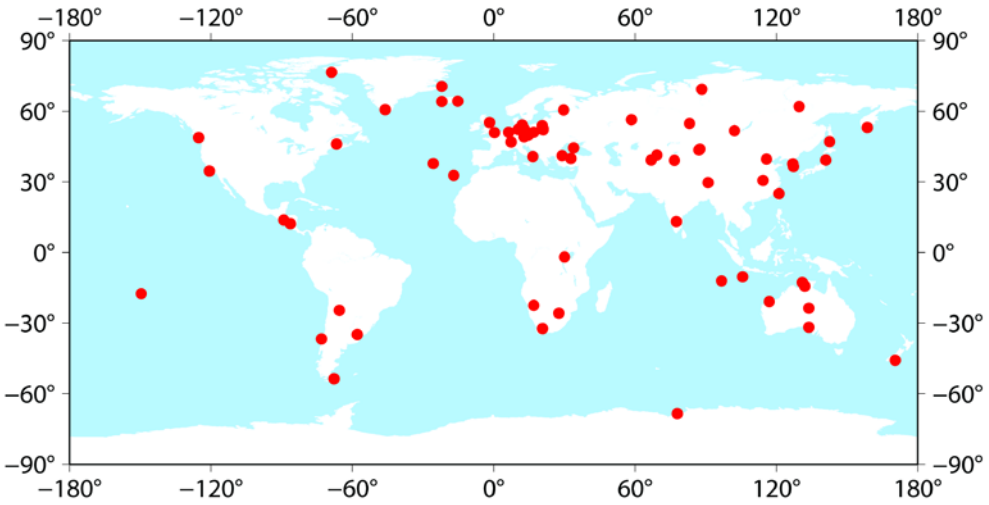

Figure 4.4 Global distribution of the IGS stations selected for the validation of ZHDs from various resources using *in-situ* pressure measurements in RINEX format

Comparisons of the ZHDs from various resources at two random stations are demonstrated in Figure 4.5. Since the UNB model is updated from [*Saastamoinen*, 1972] with improvements of ZHD determination, ZHDs from the Saastamoinen model have not been displayed. According to Figure 4.5, GPT2 is more accurate than the UNB and Hopfield models, while VMF1-FC derived ZHDs are the most accurate and show a good agreement with *in-situ* measurements.

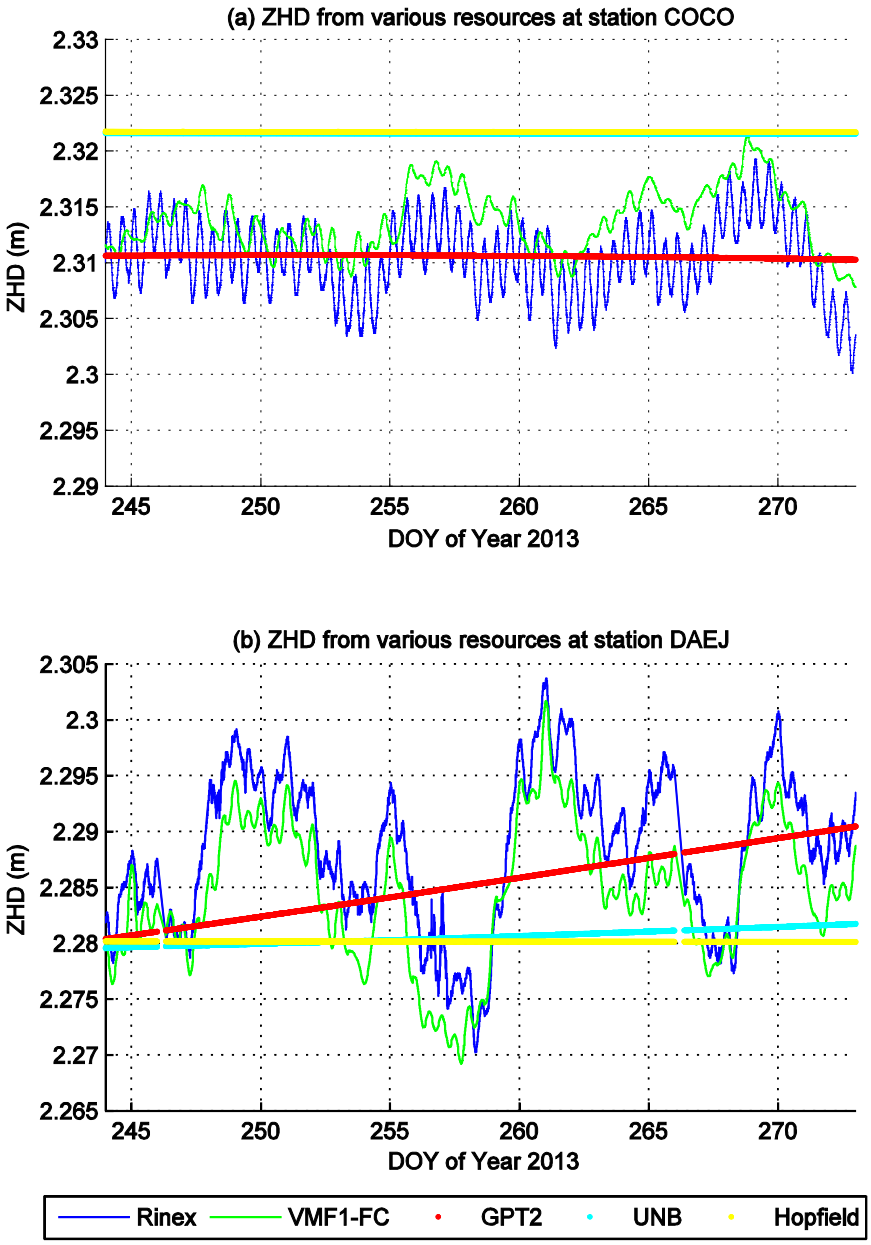

Figure 4.5 ZHDs derived from four models: VMF1-FC, GPT2, UNB and Hopfield and validated using *in-situ* pressure measurements at randomly selected two of the 71 IGS stations. It shows that GPT2 is more accurate than UNB and Hopfield, while the VMF1-FC derived ZHDs are the most accurate and show a good agreement with *in-situ* measurements.

A more detailed statistical analysis of cumulative distribution is demonstrated in Figure 4.6. As can be seen, VMF1-FC is the most accurate, followed by GPT2. For the VMF1-FC case, RMS

errors at all the selected stations are <20 mm. In addition, stations with RMS errors <15.3 mm account for 95% of the 71 stations.

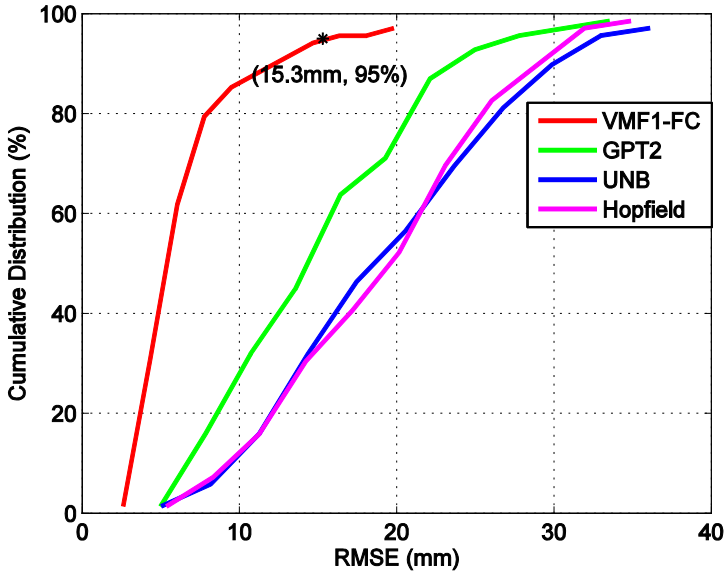

Figure 4.6 Cumulative distributions of RMS errors of the ZHDs derived from VMF1-FC, GPT2, UNB and Hopfield. Reference data taken as true values are derived using *in-situ* pressure measurements at 71 globally distributed IGS stations during September 2013. It shows that for VMF1-FC model, stations with RMS error <15.3 mm account for 95% of the 71 IGS stations.

4.7 Summary

This chapter focuses on the determination of zenith delays and mapping functions. Zenith delays include ZHD, ZWD and ZTD. They can be computed using external *in-situ* meteorological data from collocated meteorological sensors, weather stations, radiosondes, and NWP models. They can also be determined using a number of empirical models. For mapping functions, the modelling of zenith delays is treated in two different ways. One is using total mapping function while the other is the classical separation into hydrostatic and wet parts. The latter is ideal for the retrieval of PPP-PWV in this study as the rapid variation of the residual ZWD can be accounted for.

Two recently proposed mapping function models VMF1-FC and GPT2 and their implementation are described in detail in this chapter. Considering the significance of ZHD in this study, ZHDs derived from GPT2 and VMF1-FC, as well as other sources like UNB and Hopfield are validated using *in-situ* pressure measurements from 71 IGS stations. The validation proves that GPT2 and VMF1-FC can provide desirably accurate ZHDs. Both models are used in this research either as the *a priori* ZHD in PPP processing or in the conversion from ZWD to PWV. In addition, GPT2 not only provides the *a priori* ZHD but also the a_h and a_w coefficients which are indispensible for the determination of mapping functions. Compared with VMF1-FC, the implementation of GPT2 does not require a large amount of computational resources. Therefore, GPT2 is an ideal model for the modelling of tropospheric delays in PPP data processing.

Chapter 5. GPS PPP Algorithms

This chapter addresses the PPP algorithms used for parameter estimation. The widely used ionosphere-free observation is for the functional model of PPP after linearisation. For parameter estimation, Kalman filtering rather than the simple least square adjustment is used to make use of the information of previous epochs. The retrieval of ZTD is one of the high-accuracy applications of PPP hence error sources need to be carefully considered. This step of error correction is implemented in the process of linearisation. As the first-order of ionospheric delay can be eliminated by the ionosphere-free combination and the tropospheric delay is addressed in Chapter 4, this chapter introduces some other errors in PPP and the corresponding correction approaches in detail. Those errors include solid Earth tide, ocean tide loading, antenna phase centre offsets and variations on both satellites and receiver sides.

5.1 Linearisation of Ionosphere-free Observations

In equation (2.18), the combined ambiguity of ionosphere-free carrier phases for satellite p can be expressed as $N_{IF}^{*p} = \frac{c}{f_1^2 - f_2^2}\left(f_1 N_1^{*p} - f_2 N_2^{*p}\right)$. It is not an integer and treated as one parameter in the normal equation in this research.

According to the modelling of tropospheric delay in Chapter 4, $T^p(t) = z_h \cdot mf_h + z_w \cdot mf_w$. If an empirical ZHD model such as GPT2 or VMF1-FC is used then z_h, mf_h and mf_w are known values, with z_w left to be estimated. The Earth rotation effect $d_{rot}(t)$ can be corrected by applying the compensation of station displacements. The phase wind-up can be corrected using the model presented in [*Wu et al.*, 1992]. The relativistic effects can be eliminated as is discussed in [*Ashby*, 1993; *Ashby*, 1995]. Other error sources like antenna-related errors d_{ant}^p, ocean tide loading $d_{otl}(t)$, and solid Earth tide d_{set} can be eliminated using empirical models or

external datasets which will be discussed in Section 5.3. All those errors can be summarised as e_{Φ}^{p} and e_{P}^{p}:

$$e_{\Phi}^{p} = z_h \cdot mf_h - cdt^{p}(t) + d_{ant}^{p} + d_{rot}(t) + d_{rel}(t) + d_{otl}(t) + d_{set} + d_{windup} + \varepsilon_{\Phi 1,\Phi 2}^{p} \tag{5.1}$$

$$e_{P}^{p} = z_h \cdot mf_h - cdt^{p}(t) + d_{ant}^{p} + d_{rot}(t) + d_{rel}(t) + d_{otl}(t) + d_{set} + d_{windup} + \varepsilon_{P1,P2}^{p} \tag{5.2}$$

As such, equations (2.18) and (2.19) can be simplified as:

$$\Phi_{IF}^{p}(t) = \rho^{p}(t) + mf_w \cdot z_w + cdt(t) + N_{IF}^{*p} + e_{\Phi}^{p} \tag{5.3}$$

and

$$P_{IF}^{p}(t) = \rho^{p}(t) + mf_w \cdot z_w + cdt(t) + e_{P}^{p} \tag{5.4}$$

Assuming that at one GPS station, the number of successive epochs is m and the number of observed satellites is n, there will be $2mn$ ionosphere-free observation equations in total. The parameters to be estimated are

$$\hat{X} = \begin{bmatrix} x & y & z & z_w & dt & N^{*1} & \cdots & N^{*n} \end{bmatrix}^{T} \tag{5.5}$$

$(x\ y\ z)^{T}$ are receiver coordinates and the number is 3 (in static mode) or $3m$ (in kinematic mode); dt are receiver clock parameters and the number is m; $(N^{*1}\ \cdots\ N^{*n})^{T}$ are ambiguity parameters and the number is n if there are no cycle slips; z_w are zenith wet delay parameters and the number is m. For a specific epoch, the numbers of ionosphere-free observation equations and parameters are $2n$ and $5+n$ (three coordinate parameters, one zenith wet delay parameter, one receiver clock parameter and n ambiguity parameters), respectively. This

implies that the retrieval of PWV using the PPP approach is available as long as there are at least five GPS satellites in direct line-of-sight.

Let $\hat{X} = \hat{X}_0 + \hat{x}$ where $\hat{X}_0$ are the initial values and $\hat{x} = (\Delta x, \Delta y, \Delta z, \Delta z_w, \Delta dt, \Delta N^{*1}, \cdots, \Delta N^{*n})^T$ where $\hat{x}$ are the parameters to be directly estimated. Equations (5.3) and (5.4) can be linearised as

$$\hat{v} = B\hat{x} - l \tag{5.6}$$

B is called the coefficient matrix or design matrix; $\hat{v}$ is the observation residual matrix and l is the residual vector.

$$l = (\Phi_{IF}^1 - \Phi_0^1, P_{IF}^1 - P_0^1, \Phi_{IF}^2 - \Phi_0^2, P_{IF}^2 - P_0^2, \cdots, \Phi_{IF}^n - \Phi_0^n, P_{IF}^n - P_0^n)^T \tag{5.7}$$

$$B = \begin{bmatrix} \frac{\partial f_{\Phi_{IF}^1}}{\partial \mathbf{x}} & \frac{\partial f_{\Phi_{IF}^1}}{\partial \mathbf{y}} & \frac{\partial f_{\Phi_{IF}^1}}{\partial \mathbf{z}} & \frac{\partial f_{\Phi_{IF}^1}}{\partial \mathbf{z}_w} & \frac{\partial f_{\Phi_{IF}^1}}{\partial \mathbf{dt}\ (t)} & \frac{\partial f_{\Phi_{IF}^1}}{\partial \mathbf{N}^{*1}} & 0 & \cdots & 0 \\ \frac{\partial f_{P_{IF}^1}}{\partial \mathbf{x}} & \frac{\partial f_{P_{IF}^1}}{\partial \mathbf{y}} & \frac{\partial f_{P_{IF}^1}}{\partial \mathbf{z}} & \frac{\partial f_{P_{IF}^1}}{\partial \mathbf{z}_w} & \frac{\partial f_{P_{IF}^1}}{\partial \mathbf{dt}} & 0 & 0 & \cdots & 0 \\ \frac{\partial f_{\Phi_{IF}^2}}{\partial \mathbf{x}} & \frac{\partial f_{\Phi_{IF}^2}}{\partial \mathbf{y}} & \frac{\partial f_{\Phi_{IF}^2}}{\partial \mathbf{z}} & \frac{\partial f_{\Phi_{IF}^2}}{\partial \mathbf{z}_w} & \frac{\partial f_{\Phi_{IF}^2}}{\partial \mathbf{dt}} & 0 & \frac{\partial f_{\Phi_{IF}^2}}{\partial \mathbf{N}^{*2}} & \cdots & 0 \\ \frac{\partial f_{P_{IF}^2}}{\partial \mathbf{x}} & \frac{\partial f_{P_{IF}^2}}{\partial \mathbf{y}} & \frac{\partial f_{P_{IF}^2}}{\partial \mathbf{z}} & \frac{\partial f_{P_{IF}^2}}{\partial \mathbf{z}_w} & \frac{\partial f_{P_{IF}^2}}{\partial \mathbf{dt}} & 0 & 0 & \cdots & 0 \\ \vdots & \vdots & \vdots & \vdots & \vdots & \vdots & \vdots & \cdots & \vdots \\ \frac{\partial f_{\Phi_{IF}^n}}{\partial \mathbf{x}} & \frac{\partial f_{\Phi_{IF}^n}}{\partial \mathbf{y}} & \frac{\partial f_{\Phi_{IF}^n}}{\partial \mathbf{z}} & \frac{\partial f_{\Phi_{IF}^n}}{\partial \mathbf{z}_w} & \frac{\partial f_{\Phi_{IF}^n}}{\partial \mathbf{dt}} & 0 & 0 & \cdots & \frac{\partial f_{\Phi_{IF}^n}}{\partial \mathbf{N}^{*n}} \\ \frac{\partial f_{P_{IF}^n}}{\partial \mathbf{x}} & \frac{\partial f_{P_{IF}^n}}{\partial \mathbf{y}} & \frac{\partial f_{P_{IF}^n}}{\partial \mathbf{z}} & \frac{\partial f_{P_{IF}^n}}{\partial \mathbf{z}_w} & \frac{\partial f_{P_{IF}^n}}{\partial \mathbf{dt}} & 0 & 0 & \cdots & 0 \end{bmatrix} \tag{5.8}$$

According to equations (5.3) and (5.4), matrix *B* can be calculated using equation (2.9) which expresses the geometric distance between GPS satellite and receiver.

$$B=\begin{bmatrix} -\frac{X^1-X_0}{\rho^1} & -\frac{Y^1-Y_0}{\rho^1} & -\frac{Z^1-Z_0}{\rho^1} & mf_w^1 & c & 1 & 0 & \cdots & 0 \\ -\frac{X^1-X_0}{\rho^1} & -\frac{Y^1-Y_0}{\rho^1} & -\frac{Z^1-Z_0}{\rho^1} & mf_w^1 & c & 0 & 0 & \cdots & 0 \\ -\frac{X^2-X_0}{\rho^2} & -\frac{Y^2-Y_0}{\rho^2} & -\frac{Z^2-Z_0}{\rho^2} & mf_w^2 & c & 0 & 1 & \cdots & 0 \\ -\frac{X^2-X_0}{\rho^2} & -\frac{Y^2-Y_0}{\rho^2} & -\frac{Z^2-Z_0}{\rho^2} & mf_w^2 & c & 0 & 0 & \cdots & 0 \\ \vdots & \vdots & \vdots & \vdots & \vdots & \vdots & \vdots & \cdots & \vdots \\ -\frac{X^n-X_0}{\rho^n} & -\frac{Y^n-Y_0}{\rho^n} & -\frac{Z^n-Z_0}{\rho^n} & mf_w^n & c & 0 & 0 & \cdots & 1 \\ -\frac{X^n-X_0}{\rho^n} & -\frac{Y^n-Y_0}{\rho^n} & -\frac{Z^n-Z_0}{\rho^n} & mf_w^n & c & 0 & 0 & \cdots & 0 \end{bmatrix} \tag{5.9}$$

where superscripts *1*, *2* and n are the numbers of observed satellites.

5.2 Adjustment Procedures

5.2.1 Least Square Adjustment

Equation (5.6) forms the basic functional model which leads to the normal equations following the least squares principle [*Leick*, 2004]:

$$B^T PB\hat{x} = B^T Pl \tag{5.10}$$

where P is the weight matrix of the parameters. The parameters are solved as

$$\hat{x} = (B^T PB)^{-1} B^T Pl \tag{5.11}$$

The least square adjustment is simple and ideal to be implemented for batch processing, which has been widely used in previous GPS-MET studies. However it has disadvantages particularly for kinematic positioning or the retrieval of PWVs, as variances and covariances of the previous

epochs cannot be passed onto the current epoch.

5.2.2 Kalman Filtering

The Kalman Filter is a technique for the linear-quadratic problem of estimating the instantaneous state of a linear dynamic system perturbed by white noise. This is achieved by using measurements linearly related to the state but corrupted by white noise. The resulting estimator is statistically optimal with respect to any quadratic function of estimation error [*Grewal and Andrews*, 2001].

The basic process of this filter is conceptualised into two stages. The first stage is called the prediction stage using a system evolution prediction model to produce an *a priori* system state from the previous state. The second stage is called the update stage taking into account the new measurements to produce an *a posteriori* state by correcting the previous *a priori* state. This two-stage process starts with an initial estimated state and is repeated in a loop recursively until the filtering process ends [*Kalman*, 1960].

Assume the state equation at epoch $k+1$ in parameter estimation is

$$x_{k+1} = \Phi_{k+1,k} x_k + \omega_k \tag{5.12}$$

and the observation equation which is identical to equation (5.6) is rewritten as

$$z_{k+1} = H_{k+1} x_{k+1} + v_k \tag{5.13}$$

$\Phi_{k+1,k}$ in equation (5.12) is the state transition matrix for the system and ω_k is the noise vector. For a specific epoch $k+1$ from epoch k

$$\Phi_{k+1,k}=\begin{bmatrix}1 & & & & & & \\ & 1 & & & & & \\ & & 1 & & & & \\ & & & 1 & & & \\ & & & & 0 & & \\ & & & & & \phi_{N^*}^{p}=1(p=1,\cdots,n) & \end{bmatrix}_{5+n,5+n} \tag{5.14}$$

if the number of GPS satellites in view is n.

The computation of parameters at epoch k is composed of the following three steps. Step 1 is to predict the state vector $\hat{x}_k(-)$ and covariance matrix $P_k(-)$ ahead:

$$\hat{x}_k(-)=\Phi_{k,k-1}\hat{x}_{k-1}(+) \tag{5.15}$$

$$P_k(-)=\Phi_{k,k-1}P_{k-1}(+)\Phi^T_{k,k-1}+Q_{k-1} \tag{5.16}$$

(-) means the value is prior to the state update and (+) means the value is posterior to the state update. Q_{k-1} is the covariance matrix of the prediction stage noise, which somehow reflects the weight of the process estimates.

Step 2 is to compute the optimal Kalman gain matrix K and predicted residual v at epoch k:

$$K_k=P_k(-)H_k^T\left[H_kP_k(-)H_k^T+R_k\right]^{-1} \tag{5.17}$$

$$v_k=z_k-H_k\hat{x}_k(-) \tag{5.18}$$

R_k is the observation noise covariance matrix of the update stage, which reflects the degree of confidence in each one of the measurements. As there are only two types of measurements,

$$R_k = \begin{cases} (\sin(E)/0.001)^2 & (\textit{for carrier phase}) \\ (\sin(E)/0.1)^2 & (\textit{for P code}) \end{cases} \tag{5.19}$$

Prior to step 2, the ionosphere-free observations must be linearised using equations (5.6) – (5.9) to generate the design matrix H_k.

Step 3 is to update the parameters and corresponding covariance matrix using the predicted residual v_k:

$$\hat{x}_k(+) = \hat{x}_k(-) + K_k v_k \tag{5.20}$$

$$P_k(+) = (I - K_k H_k) P_k(-) \tag{5.21}$$

The Kalman filtering is repeated using the updated state $\hat{x}_k(+)$, the corresponding covariance $P_k(+)$ and new measurements z_{k+1} to compute the new state $\hat{x}_{k+1}(+)$ for epoch $k+1$. However, for the first epoch to start with, the initial values for both the system state and the covariance matrix are significant for the filtering convergence. In the modified BNC software for this study, the initial values for the three coordinate parameters and the receiver clock offset are obtained from the single point positioning using pseudorange observations. The initial ZWD is set to zero and the initial ambiguity is computed from the following equation

$$P_{IF}^p(0) = \lambda_{IF}(N^{*p}(0) + \Phi_{IF}^p(0)) \tag{5.22}$$

then

$$N^{*p}(0) = P_{IF}^p(0)/\lambda_{IF} - \Phi_{IF}^p(0) \tag{5.23}$$

The initial covariance matrix $P_{0/0}$ can be expressed as

$$P(0) = \begin{bmatrix} P_{xyz}(0) & & & \\ & P_{dt}(0) & & \\ & & P_{z_w}(0) & \\ & & & P_{N^*}(0) \end{bmatrix} \tag{5.24}$$

In the BNC software, $P(0)$ is set as

$$P_{xyz}(0) = \begin{bmatrix} 10^{-6}\ \mathrm{m}^2 & & \\ & 10^{-6}\ \mathrm{m}^2 & \\ & & 10^{-6}\ \mathrm{m}^2 \end{bmatrix} \tag{5.25}$$

$$P_{dt}(0) = 50000\ \mathrm{m}^2 \tag{5.26}$$

$$P_{z_w} = 1\ \mathrm{m}^2 \tag{5.27}$$

$$P_{N^*}^{p}(0) = 100\ \mathrm{m}^2 \tag{5.28}$$

5.3 Error Corrections for PPP

5.3.1 General Methodologies for Error Elimination or Mitigation

In the process of linearisation of observation equations, a number of error sources in equations (5.1) and (5.2) need to be removed or mitigated to obtain the high-accuracy residual vector l in equation (5.6). Those errors can be classified into the following three types.

- GPS satellite related: satellite orbit error, satellite clock offset, satellite antenna phase centre offset and variation, and phase wind-up, etc.

- Signal propagation related: ionospheric delay and tropospheric delay, etc.
- GPS receiver related: receiver clock offset, receiver antenna phase centre offset and variation, multipath effect, the Earth rotation, relativistic effects, solid Earth tide and ocean tide loading, etc.

In GPS positioning applications, there are normally five approaches to eliminate or alleviate the effects of those errors:

- to use better hardware for signal reception. A good example is to install a radome on GPS receiver (e.g. in snow conditions);
- to select a good location which is free of obstructions or away from large lakes (to alleviate the multipath effects) to setup the GPS receiver;
- to use combined observations as is introduced in the previous Sections;
- to set additional parameters such as the tropospheric delay parameter;
- to use the empirical models or external datasets.

It is noticeable that some of the errors are relatively large while some others are relatively small. Whether to implement corrections for those errors depends on the accuracy requirement of the applications. In the retrieval of PWV using the PPP approach all the error items listed in equations (5.1) – (5.2) must be carefully considered.

The PPP module of the original BNC software has limitations and has only been developed for demonstration. Some error sources like Earth rotation, relativistic effects and phase wind-up have already been considered, while some other errors are neglected. Those errors, including tropospheric delay, phase centre offset and variation of satellite antenna, phase centre offset and variation of receiver antenna, and ocean tide loading, need further corrections in this research. The modelling of tropospheric delay is introduced in detail in Chapter 4. The satellite orbit error depends on the source of orbit products hence the accuracy of the downloaded real-time orbits from BKG is further discussed in Chapter 6.

5.3.2 Corrections for Solid Earth Tide

It is common to see ocean tides which are caused by the pull of the Moon and the Sun on the ocean. However it is less well known that the solid Earth itself also responds to the Sun's and Moon's gravitational attractions. Variations of ocean tides in local sea level can exceed 10 meters, while the solid Earth tides often reach ±20 cm and can exceed ±30 cm.

The site displacements in Northing, Easting, and Vertical direction caused by tides can be represented by spherical harmonics of order n and degree m characterised by the Love number h_{nm} and the Shida number l_{nm} according to the IERS conventions [*Petit and Luzum*, 2010]. The effective values of these numbers weakly depend on station latitude and tidal frequency [*Wahr*, 1981]. It consists of a latitude dependent permanent displacement and a periodic part with predominantly semi-diurnal and diurnal periods of changing amplitudes. In real-time PPP processing, the permanent part which can reach up to 12 cm in mid-latitudes (along the radial direction) always exists; the periodic part cannot be averaged out as is done in static positioning over a 24-hour period. In addition, the orbit and clock corrections, either from IGS or BKG, do not include local effects like ocean loading or solid Earth tide. Therefore, such effects by other means should be corrected in the retrieval of PWV using GPS technique, especially considering that the effects of solid Earth tide are at least one order of magnitude larger than the accuracies currently achieved for GNSS-derived coordinates [*Dach et al.*, 2007].

The modelling of the solid Earth tide has already been considered in the original BNC software following the early version of the IERS conventions. The latest IERS 2010 model [*Petit and Luzum*, 2010] incorporates many enhancements including the effects of Love number dependence on tidal frequency and station latitude. An additional consideration is to take mantle inelasticity into account (at mm level). All those new features have been coded into the IERS 2010 conventions and ready for public use. Figure 5.1 demonstrates the station displacements in Easting, Northing and Up directions at stations MOBS and PERT. The horizontal displacements at both stations are below 10cm while the Up component can reach as high as 20cm.

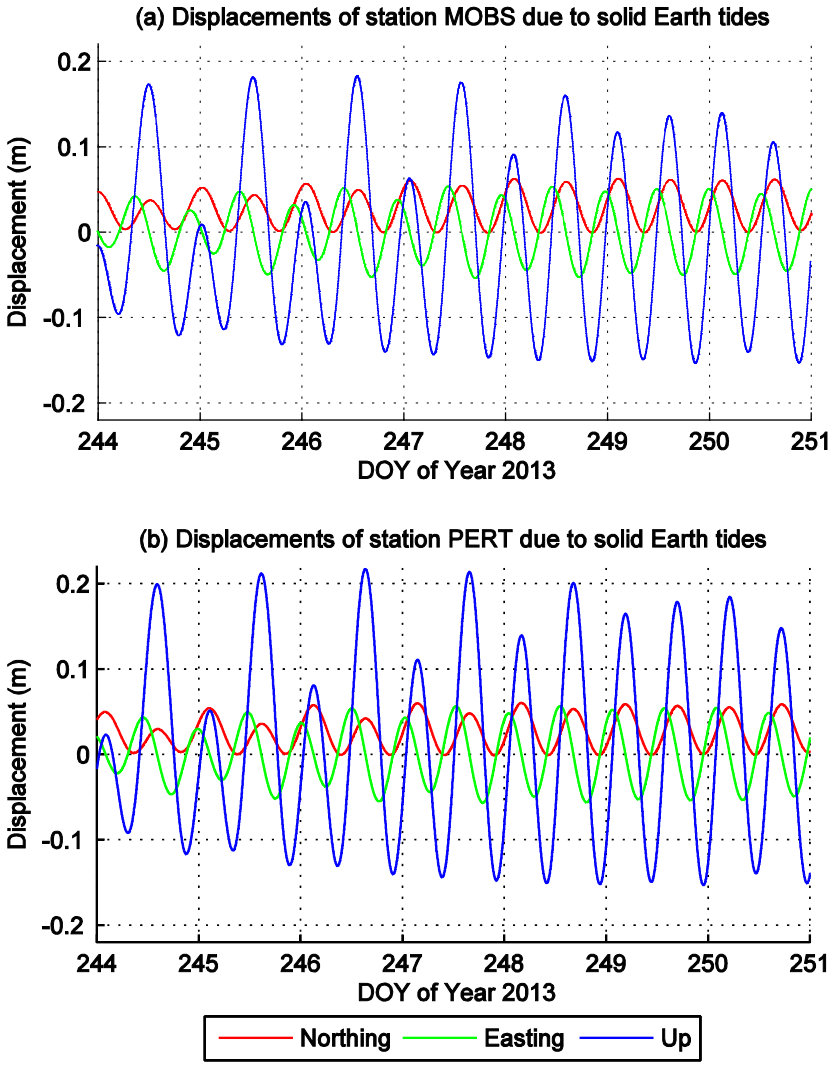

Figure 5.1 Displacements of station MOBS and PERT due to solid Earth tide following IERS 2010 conventions [*Petit and Luzum*, 2010]. The horizontal axes represent DOY from 244 to 251 of year 2013 while the vertical axes represent the station displacements in Easting, Northing and Up directions.

Two approaches are normally adopted to implement the corrections of solid Earth tide in PPP data processing. The first approach is to directly apply the correction vector $(\Delta X, \Delta Y, \Delta Z)^T$ to the Cartesian coordinates of station $(X_0, Y_0, Z_0)^T$, which is further used for the linearisation of ionosphere-free observation equations using equation (5.6). Another approach is to reduce the station displacement into range correction Δl, which is further added to the residual vector l in equation (5.7). Assuming $(X^p, Y^p, Z^p)^T$ are the ECEF coordinates of satellite p,

$$\Delta l = \sqrt{(X_0 + \Delta X - X^p)^2 + (Y_0 + \Delta Y - Y^p)^2 + (Z_0 + \Delta Z - Z^p)^2} - \sqrt{(X_0 - X^p)^2 + (Y_0 - Y^p)^2 + (Z_0 - Z^p)^2} \quad (5.29)$$

The latter approach is adopted in this study. Figure 5.2 demonstrates the range corrections due to solid Earth tide at station MOBS.

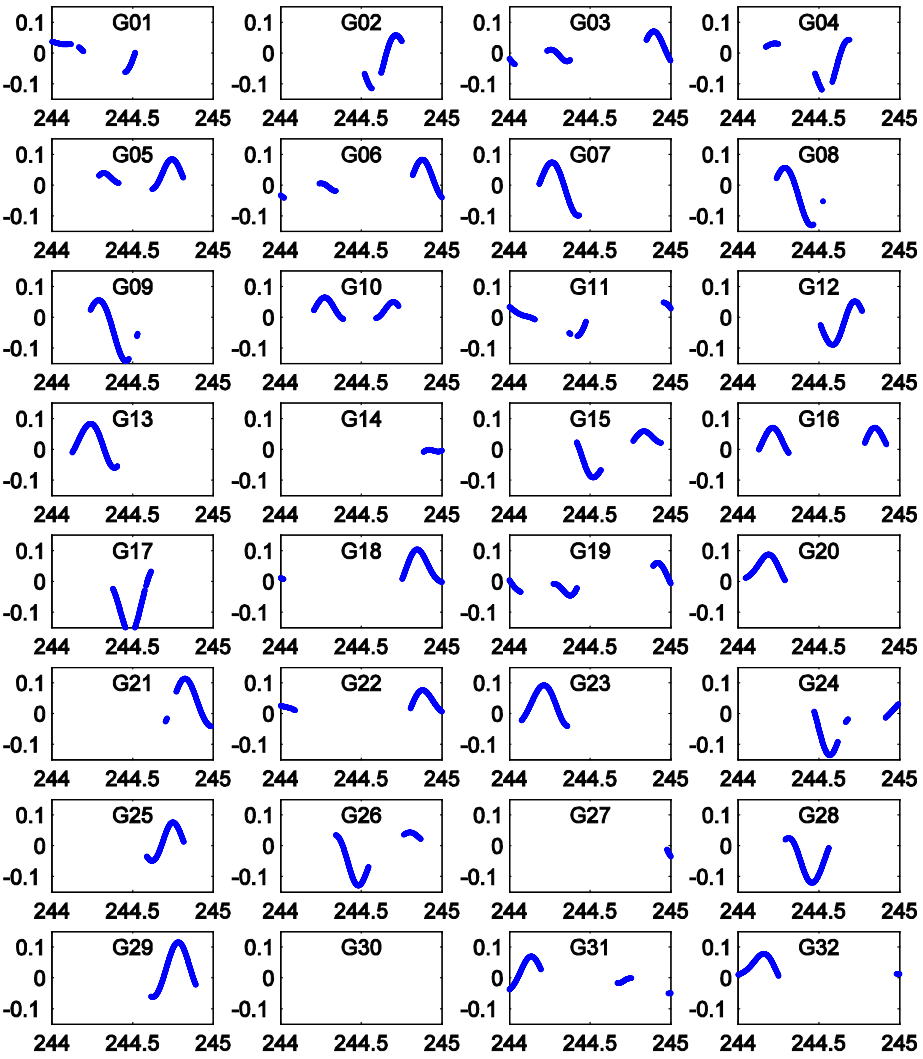

Figure 5.2 Effects of solid Earth tide at station MOBS following IERS 2010 conventions [*Petit and Luzum*, 2010]. The horizontal axis represents decimal DOYs in year 2013 while the vertical axis represents the reduced range corrections in metres, which are possible only when there are signals from the corresponding satellites.

5.3.3 Corrections for Ocean Tide Loading

The position of a GPS station is also affected by the load of ocean tides on top of the solid Earth tide, particularly if it is located in coastal regions. This is caused by the movement of the centre of mass (CoM) of the Earth due to ocean tides. If the Earth is taken as a combination of the solid Earth and the fluid masses without any external forces acting upon it, ocean tides can cause a temporal variation of the fluid mass distribution and the corresponding load on the crust. Consequently the CoM of the fluid masses moves periodically and must be compensated by an opposite motion of the CoM of the solid Earth. GPS positioning technique involves the dynamical motion of GPS satellites which is subject to the movement of the CoM of the Earth. Furthermore, the orbit and clock products which are used for high-accuracy data processing, either from IGS [*IGS*, 2014] or from BKG [*Mervart and Weber*, 2013], refer to the CoM of the Earth. In this context, ocean tide loading correction needs to be considered in GPS data processing to obtain higher-accuracy PWVs.

The magnitude of ocean tide loading can reach up to ±10 mm. This is almost an order of magnitude smaller than solid Earth tide as is discussed in Section 5.3.2. The influence of ocean tide loading on GPS data processing has been studied by *Dragert et al.* (2000). It is concluded that when ZTD are required, the ocean tide loading effects have to be taken into account even for a 24-hour static point positioning processing, unless the station is far (> 1000 km) from the nearest coast line. Otherwise, the effects will be mapped into the ZTD parameters.

The ocean tide loading has not been considered in the original version 2.8 of the BKG software. In the modified version, its correction is implemented following the latest IERS conventions [*Petit and Luzum*, 2010]. Let Δc denote a displacement component in Easting, Northing or Up directions at time t.

$$\Delta c = \sum_{k=1}^{11} f_k A_{ck} \cos(\chi_k(t) + \mu_k - \phi_{ck}) \tag{5.30}$$

Eleven main ocean tides in total are considered, including the semidiurnal M_2, S_2, N_2, K_2, the diurnal K_1, O_1, P_1, Q_1, and the long-period M_f, M_m and S_{sa}. $\chi_k(t)$ is the astronomical arguments for the 11 tides and can be calculated using the subroutine *ARG2.F* which is available on the IERS ftp; f_k and μ_k depend on the longitude of the lunar node. The amplitudes A_{ck} and phases ϕ_{ck} describe the loading response for the chosen site. It is notable that equation (5.30) gives a precision of about 0.1% [*Petit and Luzum*, 2010]. In this study the amplitude and phase coefficients are calculated by online service (by M.S. Bos and H.-G. Scherneck, available at: *http://holt.oso.chalmers.se/loading/index.html*). Figure 5.3 demonstrates these coefficients at two Australian stations MOBS and PERT. They are the output of this online service and used as input to equation (5.30). The calculated displacement components in Easting, Northing or Up directions are demonstrated in Figure 5.4.

```
$$
$$ COLUMN ORDER:  M2  S2  N2  K2  K1  O1  P1  Q1  MF  MM SSA
$$
$$ ROW ORDER:
$$ AMPLITUDES (m)
$$   RADIAL
$$   TANGENTL    EW
$$   TANGENTL    NS
$$ PHASES (degrees)
$$   RADIAL
$$   TANGENTL    EW
$$   TANGENTL    NS
$$
  MOBS
$$ GOT00.2_PP ID: 2013-09-05 16:00:21
$$ Computed by OLCMC/OLMPP by H G Scherneck, Onsala Space Observatory, 2013
$$ MOBS,                     RADI TANG  lon/lat:  144.9753  -37.8294   40.580
  .00563 .00179 .00156 .00036 .00312 .00422 .00110 .00122 .00051 .00033 .00009
  .00409 .00184 .00064 .00061 .00421 .00246 .00137 .00051 .00031 .00007 .00009
  .00414 .00106 .00075 .00028 .00541 .00345 .00177 .00078 .00023 .00010 .00017
   166.8  -21.0  129.4    5.9   51.0   31.8   48.4   26.6  -16.9   -8.6  -13.9
    94.7  129.7   93.1  123.1 -141.7 -160.4 -142.8 -166.3  116.6  114.9   11.2
    60.9  126.4   33.5  110.1  -95.0 -111.0  -96.1 -108.2   42.2   20.8    5.1
$$
  PERT
$$ GOT00.2_PP ID: 2013-09-05 16:05:29
$$ Computed by OLCMC/OLMPP by H G Scherneck, Onsala Space Observatory, 2013
$$ PERT,                     RADI TANG  lon/lat:  115.8853  -31.8020   12.670
  .00293 .00026 .00091 .00006 .00976 .00730 .00324 .00161 .00003 .00010 .00005
  .00259 .00125 .00050 .00021 .00373 .00232 .00122 .00046 .00037 .00010 .00020
  .00193 .00021 .00056 .00002 .00428 .00299 .00141 .00071 .00025 .00013 .00013
    88.5   43.3   47.5  162.2   -3.8   -2.7   -3.7  -11.5  -87.1  -22.7 -164.8
  -158.8  -97.1 -178.0 -109.2 -166.0  178.8 -167.2  177.6  100.9  107.1    9.2
   153.7 -141.2  143.2  142.1  -74.6  -88.1  -75.5  -85.2   11.1    3.0    2.5
$$
```

Figure 5.3 The amplitude and phase coefficients for the calculation of ocean tide loading at two Australian stations MOBS and PERT. The coefficients are used as input to calculate the displacement components in Easting, Northing and Up directions.

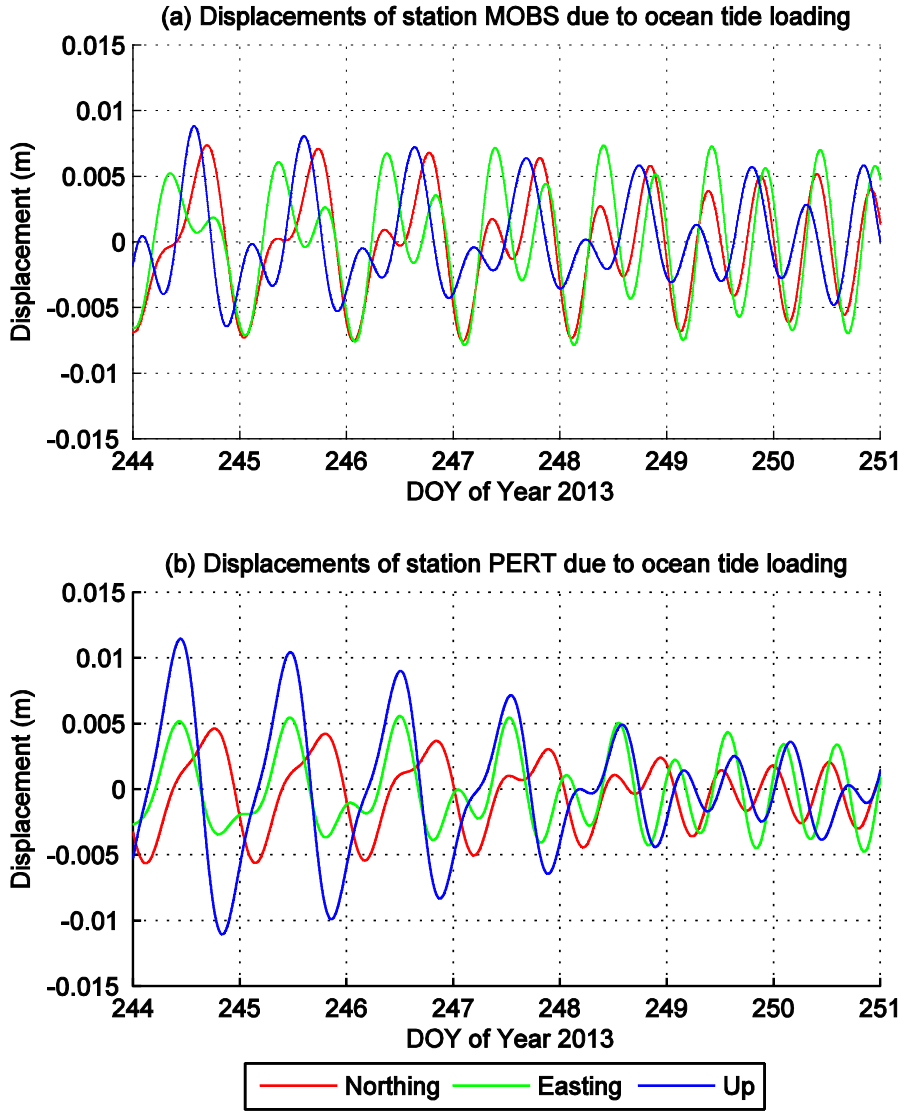

Figure 5.4 Displacements of station MOBS and PERT due to ocean tide loading following IERS 2010 conventions [*Petit and Luzum*, 2010]. The horizontal axes represent DOY from 244 to 251 of year 2013 while the vertical axes represent the station displacements in Easting, Northing and Up directions.

Let $(\Delta E, \Delta N, \Delta U)^T$ denote the topocentric station displacements in Easting, Northing and Up directions; Let $(\Delta X, \Delta Y, \Delta Z)^T$ denote the Cartesian station displacements. To transform the topocentric displacements into the Cartesian system which is ideal for PPP processing, two rotations are needed. One is the clockwise rotation over east-axis by an angle $\pi/2 - \varphi$ (where φ is the station latitude) to align the up-axis with the z-axis, which is denoted as

$R_1[-(\pi/2-\varphi)]$. Another rotation is the clockwise rotation over the z-axis by an angle $\pi/2+\lambda$ (where λ is the station longitude) to align the east-axis with the x-axis, which is denoted as $R_3[-(\pi/2+\lambda)]$ [*Xu*, 2007].

$$\begin{bmatrix}\Delta X\\ \Delta Y\\ \Delta Z\end{bmatrix} = R_1[-(\pi/2-\varphi)]R_3[-(\pi/2+\lambda)]\begin{bmatrix}\Delta E\\ \Delta N\\ \Delta U\end{bmatrix} \tag{5.31}$$

$$R_1[-(\pi/2-\varphi)]R_3[-(\pi/2+\lambda)] = \begin{pmatrix}-\sin\lambda & \cos\lambda & 0\\ -\sin\varphi\cos\lambda & -\sin\varphi\sin\lambda & \cos\varphi\\ \cos\varphi\cos\lambda & \cos\varphi\sin\lambda & \sin\varphi\end{pmatrix} \tag{5.32}$$

In the modified BNC software, the Cartesian displacements are reduced to the range corrections between a GPS station and the corresponding GPS satellites as is done for solid Earth tide. Figure 5.5 clearly demonstrates the range corrections between station MOBS and 32 corresponding GPS satellites. Compared to the effects of solid Earth tide shown in Figure 5.2, ocean tide loading at this station is almost an order of magnitude smaller.

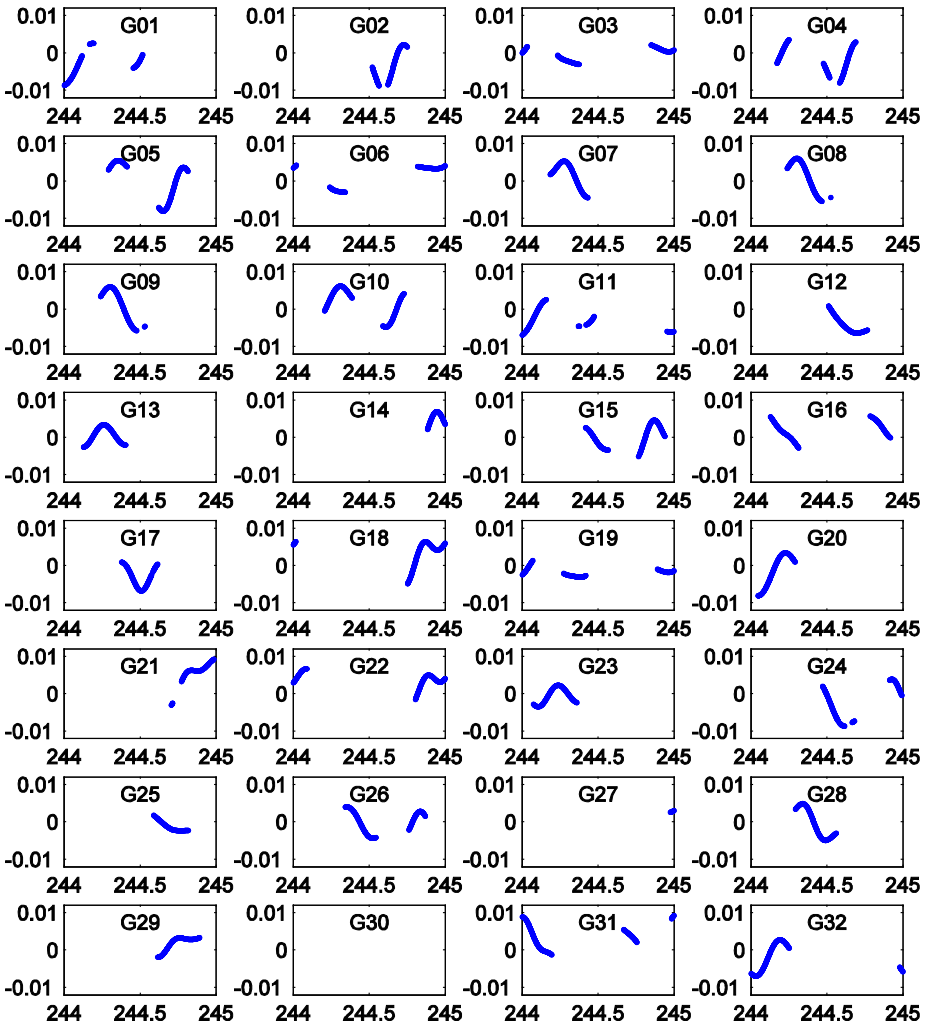

Figure 5.5 Effects of ocean tide loading at station MOBS following IERS 2010 conventions [*Petit and Luzum*, 2010]. The horizontal axis represents decimal DOYs in year 2013 while the vertical axis represents the reduced range corrections in metres, which are possible only when there are signals from the corresponding satellites.

5.3.4 Satellite Antenna PCO and PCV

The GPS measurements are made to the antenna phase centres of the receiver and GPS satellites. In other words, the geometric distance $\rho^p(t)$ in equations (5.3) and (5.4) in fact

refers to the phase centre rather than to the CoM of satellite antenna. If the post-processed GPS orbit and clock products refer to CoM of GPS satellites, corrections must be implemented to compensate for this separation. IGS has been conventionally using the absolute phase centre correction model [*Schmid and Rothacher*, 2003; *Schmid et al.*, 2007; *Rothacher and Schmid*, 2014]. In this model these corrections comprise mean offsets of the electrical antenna phase centre (PCOs), as well as phase centre variations (PCVs) as a function of the nadir angles.

The IGS model igs08.atx (available online: *http://igscb.jpl.nasa.gov/igscb/station/general/igs08.atx*) is used to determine the phase centre corrections in this study. Since the real-time orbit and clock products from BKG are referred to the satellite's antenna phase centre, PCO corrections are not needed in this study while PCV corrections are necessary. The PCV corrections involve the interpolation of nadir angles of GPS satellites. Figure 5.6 shows the geometry of GPS receiver and satellite, the elevation of GPS satellite and the nadir angle.

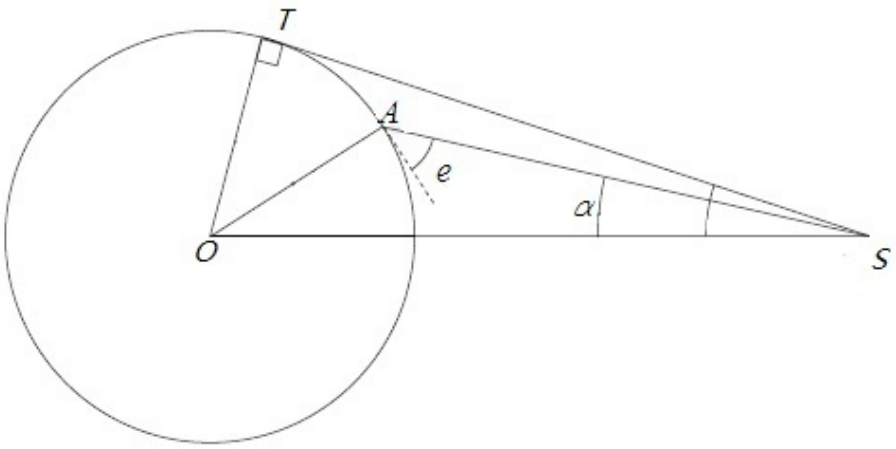

Figure 5.6 The geometry of a GPS receiver. *A* is the receiver, *S* is a GNSS satellite. *O* is the CoM of the Earth. e is the elevation of GPS satellite. α is the nadir angle which is used for the interpolation of satellite PCV.

5.3.5 Receiver Antenna PCO and PCV

Receiver antenna phase centre offsets and variations also need to be taken into account to obtain high-accuracy PWVs, using the same model IGS08.atx. The receiver PCO is given in a topocentric left-handed system with Easting, Northing and Up components, which can be denoted as $(\Delta E, \Delta N, \Delta U)^T$. The corresponding PCO corrections in Cartesian coordinate system $(\Delta X, \Delta Y, \Delta Z)^T$ can be calculated using equations (5.31) and (5.32).

The calculation of receiver PCV is more complex than that of satellite, although it is given as a range correction between GPS station and satellite. Firstly, receiver PCVs at L1 and L2 are independent. Furthermore, for each frequency it comprises two parts. The first part is elevation-dependent, which requires an interpolation of satellite elevation between 0 and 90°. The second part depends not only on the satellite elevation, but also on the satellite azimuth which counts clockwise from the North toward the East. Bilinear interpolation of both satellite elevation and station azimuth is implemented in this study to obtain the second part. If the receiver PCVs on L1 and L2 are denoted as Δl_{pcv1} and Δl_{pcv2} respectively, the receiver PCV correction for the ionosphere-free model is

$$\Delta l_{pcv} = \frac{f_1^{\,2}}{f_1^{\,2} - f_2^{\,2}} \Delta l_{pcv1} - \frac{f_2^{\,2}}{f_1^{\,2} - f_2^{\,2}} \Delta l_{pcv2} \tag{5.33}$$

5.4 Summary

In this chapter the PPP algorithms used for parameter estimation is introduced. The ionosphere-free combination of pseudoranges and carrier phases are used in this study as it eliminates the first order of ionospheric delay. When it comes to parameter estimation, the least squares adjustment and Kalman filtering are two widely-used approaches. The latter is continuously updated using the previous epochs and it is implemented in the original BNC

software package. To pass the update information of the previous epochs to the current epoch in Kalman filtering, two steps are needed for a specific epoch. The first step “prediction” is to produce an *a priori* system state using a system evolution prediction model. The second step “update” is to produce an *a posteriori* state by correcting the previous *a priori* state and taking into account the new measurements.

The retrieval of ZTD requires high-accuracy error corrections. The magnitude of solid Earth tide can reach ±20 cm while the magnitude of ocean tide loading is almost one order of magnitude smaller. Both effects in this research are corrected using the latest IERS conventions. The antenna-related errors actually include the following four parts:

- satellite PCO which is taken into account in the generation of orbits and clocks in BKG;
- satellite PCV which involves the interpolation of nadir angles of GPS satellites;
- receiver PCO which is given in a topocentric left-handed system with Easting, Northing and Up components;
- receiver PCV which requires interpolations of satellite elevation and station azimuth.

For PPP processing in this research, since the real-time orbits and clocks from BKG are referred to the satellite's antenna phase centre, satellite PCO corrections are not needed. However the other three parts, i.e., satellite PCV, receiver PCO and receiver PCV, will significantly degrade the accuracy of PPP processing and need to be corrected carefully.

Based on the PPP algorithms discussed in this chapter, the next chapter will show the experimental results of real-time retrievals of atmospheric delays, along with details of data selection and result validation.

Chapter 6. Real-time Retrievals of Atmospheric Delays Using GPS Data

This chapter mainly presents the experimental results of real-time retrieval of ZTD using the PPP approach. The software platform used in this study is BNC which was originally developed by BKG for the processing of real-time GNSS data stream in terms of simultaneously retrieving, decoding, converting and PPP processing. This complicated software package has a PPP module dedicated for demonstration. However, to cater for the high-accuracy retrieval of ZTD, substantial improvements on this module are indispensable. This chapter explains the selection of data to be processed and the ration behind that. The validation of the retrieved ZTD is vital in this research as it will be used further to derive PWV. For this purpose, two sets of IGS tropospheric products from USNO and CODE are used as reference data.

6.1 BNC Software for Real-time PPP Processing

6.1.1 Introduction of BNC

BNC has been developed under GNU General Public License (GPL) and within the framework of the IAG sub-commission for the EUREF and the IGS. This means that source code is available from subversion software archive i.e. *http://software.rtcm-ntrip.org/svn/trunk/BNC*. Users may download and modify the source code for various applications as is stated in [*Mervart and Weber*, 2013]:

- To retrieve real-time GNSS observations via the NTRIP or serial port;
- To generate high-rate RINEX observations and broadcast ephemeris to support near real-time or real-time GNSS applications;
- To generate orbit and clock corrections to broadcast ephemeris through an IP port to support real-time PPP applications;

- To combine unsynchronised or synchronised orbit and clock corrections coming simultaneously from various correction providers;
- To monitor the performance of a network of real-time GNSS data streams to generate advisory notes in case of outages or corrupted streams;
- To feed a stream into a GNSS receiver via serial communication link;
- To produce, encode and upload combined broadcast corrections;
- To implement PPP and plot the RMS errors in Easting, Northing and Up directions. A typical flow chart of PPP processing using BNC is demonstrated in Figure 6.1. 'Ntrip caster' in this figure represents real-time observation and correction providers such as *http://www.euref-ip.net/home*, *http://www.igs-ip.net/home*, and *http://products.igs-ip.net/home*. GNSS engine can be a GNSS receiver or NTRIP caster.

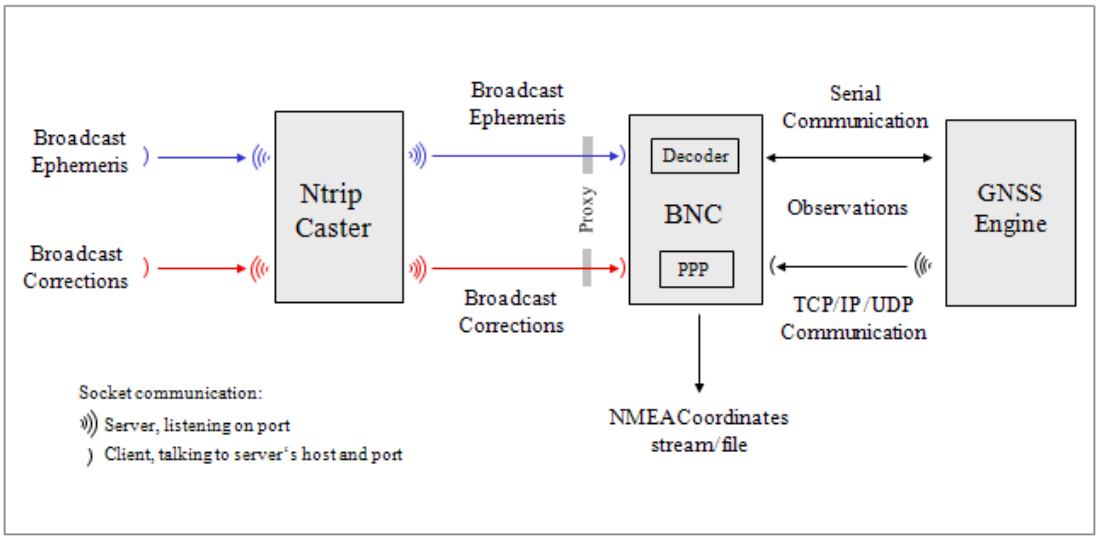

Figure 6.1 A typical flow chart of PPP processing using BNC [*Mervart and Weber*, 2013].

6.1.2 Modifications on BNC

The real-time PPP processing for the retrievals of PWVs is implemented in the BNC software Version 2.8 under Red Hat Enterprise Linux 6. However, the PPP module of the original BNC software has limitations and has only been developed for demonstration, which means that some of the errors mentioned previously are not considered. Our extensive testing revealed that

substantial improvements of the PPP module have to be coded. The main refinement and new development include

1) error corrections of solid Earth tide. The original correction model is based on the early IERS conventions and relatively simple. In the modified version, the latest IERS conventions are implemented.

2) error corrections of ocean tide loading which significantly improve the accuracy of ZTD [*Dragert et al.*, 2000]. In the modified version, this correction is implemented following the latest IERS conventions as is demonstrated in equation (5.33). The amplitude and phase coefficients are calculated by the online service (by M.S. Bos and H.-G. Scherneck, available at: *http://holt.oso.chalmers.se/loading/index.html*). The calculated Cartesian displacements in Easting, Northing and Up directions are reduced to the range corrections between a GPS station and the corresponding GPS satellites.

3) PCO and PCV corrections for satellites and receivers. This involves a number of steps which include:

- The satellite PCO correction is not necessary in this study, as the real-time orbit and clock products from BKG are referred to satellite antenna phase centre.
- The satellite PCV correction needs to be implemented, which involves the interpolation of nadir angles of GPS satellites and the absolute phase centre correction model [*Schmid et al.*, 2007; *Rothacher and Schmid*, 2014] as is discussed in Section 5.4.4.
- The receiver PCO and PCV corrections are implemented together using the IGS model igs08.atx (available online *http://igscb.jpl.nasa.gov/igscb/station/general/igs08.atx*). The receiver PCO correction involves a topocentric left-handed system which is transformed to Cartesian coordinate system and then added to the Cartesian coordinates of the receiver. The receiver PCV correction involves two parts. The first part is elevation-dependent but azimuth-independent, which requires an interpolation of satellite elevation between 0 and 90°. The second part depends not only on satellite

elevation, but also on station azimuth which counts clockwise from the North toward the East.

4) the modelling of tropospheric delays. Different model combinations of *a priori* ZHDs and mapping functions are implemented and tested in PPP algorithms. It should be noted that the derived ZTDs using VMF1-FC and GPT2 are within small differences (<2 mm). While the implementation of VMF1-FC is much more computational resources demanding and dependent on a continuously updated external dataset, the GPT2 model is used to provide the *a priori* ZHDs to retrieve the PPP-ZTDs and to further retrieve the PPP-PWVs. In addition, the Kalman filtering for epoch-by-epoch processing is adopted. Random walk is assumed sufficient for the stochastic modelling of ZTD estimation. A random walk sigma of $3e^{-6}\ m/\sqrt{s}$ is expected to address the tropospheric variations, which means that the tropospheric effect may vary for $3600\times 3e^{-6}\approx 0.01\ m/h$. The initial coordinates for the Kalman filtering are either from the mean values of the first few hours or from external sources, e.g., IGS daily solutions (available at: ftp://cddis.gsfc.nasa.gov/pub/gps/products/) as is the case in this study. Figure 6.2 shows a typical case of real-time retrieval of ZTD using BNC Version 2.8 at station MOBS. It shows that for real-time PPP positioning, three sorts of data are required: 1) the real-time GPS observations termed MOBS0 (from Ntrip caster www.igs-ip.net:2101, account and password applied), 2) the GPS broadcast ephemerides termed RTCM3EPH (from Ntrip caster products.igs-ip.net:2101), and 3) the GPS orbit and clock corrections to the broadcast ephemerides (termed IGS02, from Ntrip caster products.igs-ip.net:2101). The coordinate biases in Easting, Northing and Up directions displayed are close to zero, implying that tight constraints are applied on the station coordinates.

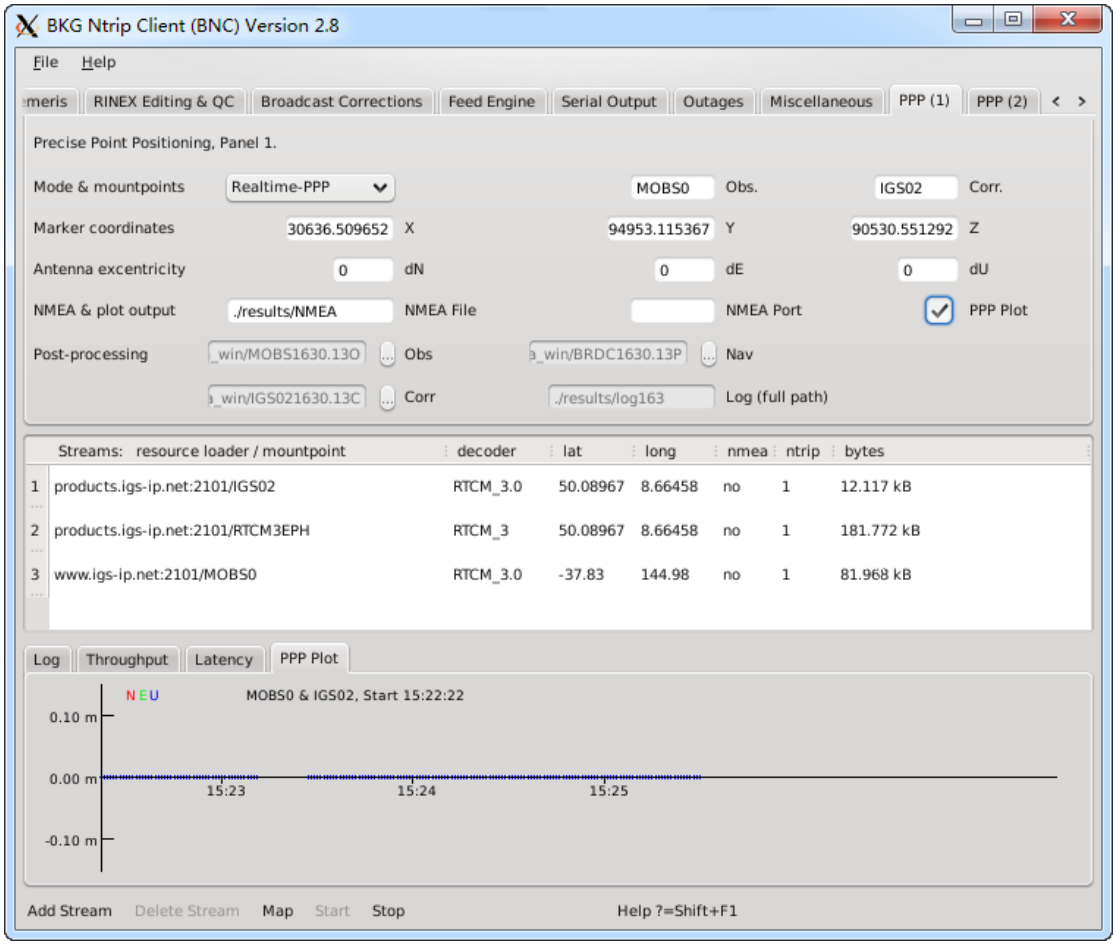

Figure 6.2 Real-time retrieval of ZTD using BNC Version 2.8 at station MOBS

6.2 Data Selection

6.2.1 Real-time Observations from 20 Global Stations

The GPS observations from 20 IGS stations for September 2013 (DOY 244-273) are selected for testing, based on the following criteria: 1) GPS observations are available; 2) dataset covers different climatic regions; 3) reference data from CODE and USNO (see Section 6.2.3) is available to validate the derived ZTDs; 4) radiosonde stations within 60 km distance of the IGS stations are available to validate the derived PWVs. GPS data from each station is collected at a sampling rate of 1 /s. ZTDs can be estimated at the same interval, which has a very high demand of computational resources. In this context GPS data is processed every 30 seconds. Therefore approximately 86400 PPP epoch-solutions are available for each station in the period of 30

days, which is considered sufficient for this investigation. The distribution of the selected stations is demonstrated in Figure 6.3.

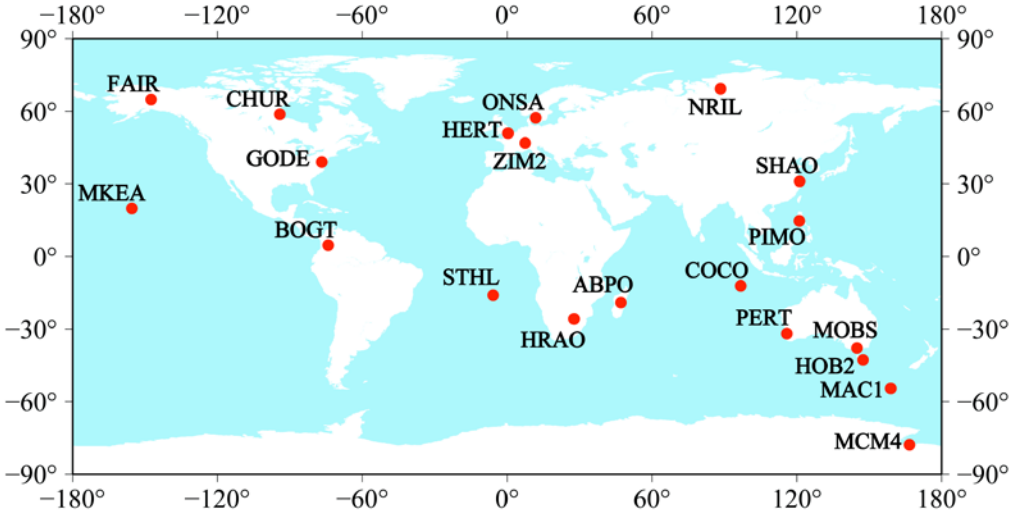

Figure 6.3 Global distribution of the IGS stations selected for the retrieval of PWV using GPS data. For these stations the collected data includes GPS real-time measurements, ZTD products (as references from USNO and CODE) and radiosonde data (as references from radiosonde sites within 60 km distance).

6.2.2 Real-time Corrections of Clocks and Orbits

Currently there are 10 Analysis Centres providing real-time product streams through NTRIP protocol [*Dow et al.*, 2009]. The European Space Operations Centre (ESOC) of ESA and BKG provide the combination of products, known as the IGS01/IGC01, IGS02 and IGS03 corrections. IGS01 is the single epoch combination produced using the software package developed by ESA/ESOC. The orbit and clock corrections at different epochs are completely independent of each other. IGS01 and IGC01 contain the same orbit and clock corrections. The only difference is that IGS01 is referred to the satellite antenna phase centre, while IGC01 is referred to the satellite centre of mass. IGS02 is a combination based on Kalman filtering using the BNC software. So the accuracy of the corrections at different epochs is stable once the filter converges after a few minutes. IGS03 is produced following the same approach as IGS02. The major difference is that both GLONASS and GPS corrections are included in IGS03. The orbit

and clock corrections are given as offsets to the broadcast ephemeris. Two streams of broadcast ephemeris: RTCM3EPH and RTCM3EPH01 are provided. The former is produced using the BNC software by BKG while the latter is produced using the RETICLE software from the German Aerospace Centre [*Mervart and Weber*, 2011; *Caissy et al.*, 2012]. According to SSR conventions, message 1019 represents GPS broadcast ephemerides; Message 1057 represents GPS orbit corrections to broadcast ephemeris; Message 1058 represents GPS clock corrections to broadcast ephemeris.

The quality of orbits and clocks is monitored by the IGS Real-time Analysis Centre Coordinator (monitoring reports are available and updated at: *http://rts.igs.org/monitor/*). Currently the accuracies of the clock corrections vary from 0.1 ns to 0.15 ns, which is demonstrated by Figure 6.4. The accuracies of the orbits are approximately 5 cm, which is demonstrated by Figure 6.5. This is at the same accuracy level as IGU (predicted half part) products, while the real-time corrections are provided at high temporal resolutions (10 second intervals for clocks and 60 second intervals for orbits) and are particularly useful for the real-time PPP applications.

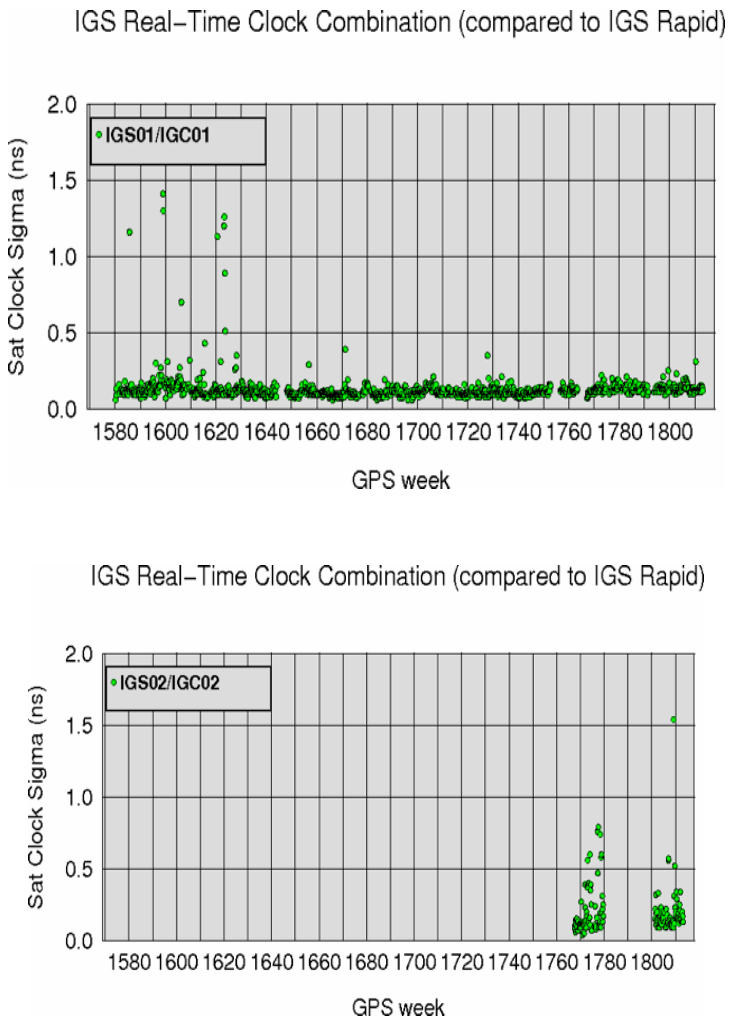

Figure 6.4 Quality motoring of IGS01/IGC01 and IGS02/IGC02 clocks performed daily against the IGS rapid solution monitored by the IGS Real-time Analysis Centre Coordinator (monitoring reports are available and updated routinely at: *http://rts.igs.org/monitor*). It shows that the accuracies of both clock correction streams vary from 0.1 ns to 0.15 ns.

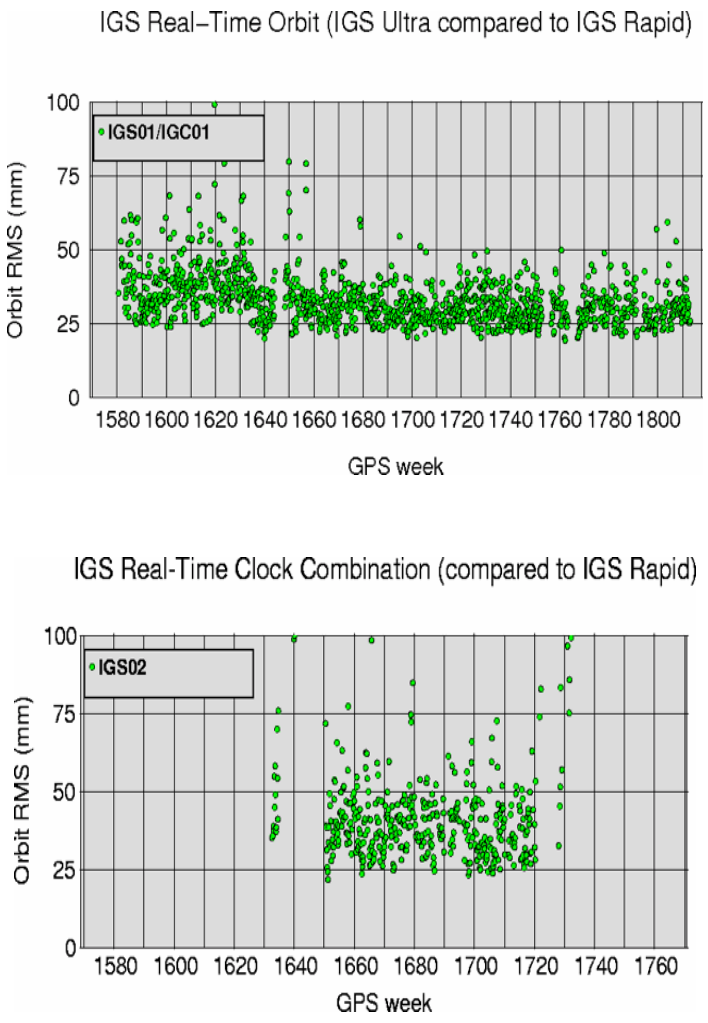

Figure 6.5 Quality motoring of IGS01/IGC01 and IGS02 orbits performed daily against the IGS rapid solution monitored by the IGS Real-time Analysis Centre Coordinator (monitoring reports are available and updated routinely at: *http://rts.igs.org/monitor*). It shows that the accuracies of both orbit correction streams are approximately 5 cm.

The three streams of corrections (listed in Table 6.1) generated using BNC are used for this investigation as our PPP algorithms are tested using the same software.

Table 6.1 Real-time clocks and orbits from BKG for the retrieval of PWV

Caster IP: Port	Mount point	Message	Content
products.igs-ip.net:2101	RTCM3EPH	1019	GPS broadcast ephemerides
products.igs-ip.net:2101	IGS02	1057	GPS orbit corrections to broadcast ephemerides
products.igs-ip.net:2101	IGS02	1058	GPS clock corrections to broadcast ephemerides

6.2.3 IGS Tropospheric Products from CODE and USNO

The IGS ACs routinely release ZTD products derived from the GPS observations based on the final orbit and clock products. The current accuracy of these ZTD products is at the level of 4 mm [*Dow et al.*, 2009] in terms of RMS, depending on different data processing strategies and solutions. The ZTD products used in this study are obtained from CODE and USNO as both datasets are released to the public. The CODE products are estimated by the Bernese software [*Dach et al.*, 2007] with an interval of two hours for more than 200 globally distributed GPS stations. GPT and GMF are used for the modelling of tropospheric delays [*Dach et al.*, 2009; *Teke et al.*, 2011]. The ZTDs from USNO are officially announced as the IGS tropospheric products since July 2011. They are calculated by the PPP approach using Bernese software with an interval of 5 minutes and latency around 3 weeks. The GMF mapping functions and the dry Niell *a priori* ZHD are adopted for the modelling of tropospheric delays [*Byram and Hackman*, 2012].

6.3 Real-time PPP-ZTD Results and Validation

The real-time PPP retrieved ZTDs (denoted as PPP-ZTDs) are compared with the IGS products from USNO and CODE. Since interpolation of USNO & CODE ZTDs and averaging process of real-time PPP-ZTDs may introduce new biases, only ZTDs with explicit values at the same epochs from these three sources are used for comparison. Differences of ZTDs are analysed in terms of mean bias, standard deviation (STD) and RMS error assuming that the IGS products are true values.

PPP algorithms in this research are implemented and tested based on different combinations of *a priori* ZHDs and mapping functions. Results show that the PPP-ZTDs are more likely to be influenced by the mapping functions rather than by the *a priori* ZHDs. More specifically, PPP-ZTDs based on [*Hopfield*, 1971] and [*Saastamoinen*, 1972] are similar if the same NMF is used. PPP-ZTDs based on GPT2 and VMF1-FC are within 1-2mm differences. As such,

PPP-ZTD results presented here are based on three tropospheric model combinations: 1) [*Saastamoinen*, 1972] derived ZHD and NMF derived mapping functions, 2) UNB derived ZHD and mapping functions, and 3) GPT2 derived ZHD and mapping functions. Tables 6.2 – 6.4 show the cross-comparison of ZTDs between the three resources: real-time PPP, USNO and CODE.

Table 6.2 Mean bias (mm), STD (mm), RMS (mm) and percentage of values below 20 mm of the differences between CODE-ZTDs and USNO-ZTDs during September 2013.

Sites	*bias*	*STD*	*RMS*[a]	*<20*[b]
ABPO	1.0	4.4	4.5	100
BOGT	1.3	5.8	5.9	99
CHUR	-1.0	3.3	3.4	99
COCO	0.1	4.7	4.7	99
FAIR	-2.3	3.4	4.1	99
GODE	0.1	4.3	4.3	99
HERT	-0.3	4.6	4.6	100
HOB2	-0.7	4.3	4.4	100
HRAO	0.6	4.8	4.9	99
MAC1	-2.0	3.5	4.1	100
MCM4	-6.2	2.8	6.8	100
MKEA	-0.9	5.0	5.0	99
MOBS	-0.1	4.3	4.3	100
NRIL	-2.7	2.7	3.8	100
ONSA	0	4.1	4.1	100
PERT	-1.0	4.3	4.4	100
PIMO	-2.2	7.2	7.5	98
SHAO	-1.5	4.7	4.9	99
STHL	1.9	4.6	5.0	100
ZIM2	-1.3	4.1	4.3	100

[a]This column shows that the RMS errors between the CODE and USNO ZTDs vary from 3.4 mm to 7.5 mm. Hence these two sets of ZTDs are considered quite stable and sufficiently accurate as the reference data for the validation of PPP-ZTDs.

[b]The threshold value for weather nowcasting as is suggested by [*De Haan*, 2006].

Table 6.3 Mean Bias (mm), STD (mm), RMS (mm) and percentage of values below 20 mm of the differences between real-time PPP-ZTDs and CODE-ZTDs under three ZHD and mapping function combinations during September 2013

Sites	1) Saastamoinen, NMF[a]				2) UNB[a]				3) GPT2[a]			
	Bias	*STD*	*RMS*[b]	*<20*	*Bias*	*STD*	*RMS*[b]	*<20*	*Bias*	*STD*	*RMS*[b]	*<20*
ABPO	0.4	6.3	6.3	99	3.5	8.0	8.8	97	-2.6	7.9	8.3	97
BOGT	10.9	8.5	13.9	84	2.0	9.8	10.0	94	0.1	9	9	97
CHUR	5.5	7.6	9.4	98	3.1	9.9	10.4	93	0.7	8.8	8.8	96
COCO	16	11.7	19.9	69	6.1	11.4	12.9	89	3.4	10.4	11	94
FAIR	9.9	7.5	12.4	90	2.0	6.9	7.2	98	1.7	7.1	7.3	98
GODE	8	11.1	13.7	87	2.4	15.7	15.9	88	0.6	11.5	11.6	95
HERT	5.4	7.8	9.5	96	2.8	14.1	14.4	91	0.8	10.5	10.5	95
HOB2	7.1	7.3	10.2	96	6.3	9.9	11.7	93	1.2	9.5	9.6	95
HRAO	2.8	6.8	7.3	98	2.9	8.9	9.3	95	2.3	9	9.3	95
MAC1	2.3	5.7	6.1	99	-1.5	7.3	7.5	97	-0.1	7.2	7.2	99
MCM4	0.5	4.7	4.8	100	-6.5	5.1	8.3	99	-1.2	5.5	5.6	99
MKEA	1.6	6.1	6.4	100	6.4	6.8	9.3	97	5.1	6.4	8.1	98
MOBS	2.2	7.5	7.8	98	1.5	10.7	10.8	94	-0.3	9.6	9.6	94
NRIL	-0.4	6.6	6.6	99	-4.2	5.3	6.7	99	-2.8	5	5.7	99
ONSA	4.3	7.3	8.4	99	3.0	9.2	9.7	95	1.3	8.4	8.5	97
PERT	8.6	10.7	13.7	84	2.2	11.1	11.3	93	-1.2	10.2	10.2	94
PIMO	19.1	11.4	22.2	57	13.4	11.5	17.7	73	0.8	11.6	11.6	90
SHAO	8	8.2	11.5	92	4.8	12.6	13.5	88	-1.3	11.1	11.2	92
STHL	13.6	5.9	14.8	84	10.7	7.0	12.8	90	9.8	6.8	11.9	92
ZIM2	6.5	6.7	9.3	97	2.8	8.7	9.2	97	-1.1	8.1	8.1	96

[a]PPP algorithms are implemented based on three different combinations of *a priori* ZHDs and mapping functions: 1) [*Saastamoinen*, 1972] derived ZHD and NMF derived mapping functions, 2) UNB derived ZHD and mapping functions, and 3) GPT2 derived ZHD and mapping functions.

[b]The three RMS columns show that the accuracies of PPP-ZTDs based on GPT2 are the best and <12 mm assuming that CODE ZTDs are the true values.

Table 6.4 Mean Bias (mm), STD (mm), RMS (mm) and percentage of values below 20 mm of the differences between real-time PPP-ZTDs and USNO-ZTDs under three ZHD and mapping function combinations during September 2013

Sites	1) Saastamoinen, NMF[a]				2) UNB[a]				3) GPT2[a]			
	Bias	*STD*	*RMS*[b]	*<20*	*Bias*	*STD*	*RMS*[b]	*<20*	*Bias*	*STD*	*RMS*[b]	*<20*
ABPO	-0.3	6.4	6.4	100	3.3	9.7	10.2	94	-2.8	8.8	9.2	96
BOGT	10	9.3	13.7	85	0.9	10.4	10.5	94	-1.2	9.6	9.6	95
CHUR	6.2	8.3	10.4	96	4.1	10.7	11.4	93	1.4	9.4	9.5	95
COCO	14.5	11.4	18.4	75	5.8	12.2	13.5	87	3.2	11.1	11.5	91
FAIR	10.6	8.3	13.4	89	4.7	7.3	8.6	97	4.4	7.4	8.6	97
GODE	8	11.5	14	87	2.7	16.2	16.4	86	1.2	11.6	11.7	92
HERT	6.1	8	10.1	96	3.0	14.9	15.1	89	1.1	11.8	11.8	94
HOB2	7	9.3	11.6	93	6.2	11.0	12.6	89	1.1	10.6	10.7	93
HRAO	2.9	7.5	8	99	2.5	9.1	9.4	95	1.8	8.9	9.1	96
MAC1	3	6.6	7.2	99	-0.4	7.9	7.9	97	0.8	7.5	7.6	98
MCM4	4	5.2	6.5	100	-1.0	4.9	5.0	99	4.3	5.2	6.8	99
MKEA	6.5	6.6	9.3	98	6.9	7.0	9.8	96	5.5	6.5	8.5	98
MOBS	2.1	8.4	8.7	98	0.9	12.3	12.3	91	-1	10.8	10.9	93
NRIL	0.9	6.1	6.2	99	-1.8	5.7	6.0	99	-0.4	5.7	5.7	99
ONSA	5.3	7.6	9.3	98	3.2	10.0	10.5	94	1.4	9.1	9.2	96
PERT	8.6	12.3	15	79	3.3	12.6	13	89	0.3	11.4	11.4	92
PIMO	22.4	13.5	26.1	45	16.0	12.9	20.6	66	2.5	12.5	12.7	88
SHAO	9.7	9.2	13.4	86	5.9	13.0	14.3	87	-0.4	11.4	11.4	93
STHL	11.9	7.7	14.2	83	7.4	8.6	11.3	92	6.4	7.9	10.2	95
ZIM2	7.9	6.8	10.4	97	4.3	8.8	9.8	96	0.3	8.4	8.4	97

[a]PPP algorithms are implemented based on three different combinations of *a priori* ZHDs and mapping functions: 1) [*Saastamoinen*, 1972] derived ZHD and NMF derived mapping functions, 2) UNB derived ZHD and mapping functions, and 3) GPT2 derived ZHD and mapping functions.

[b]The three RMS columns show that the accuracies of PPP-ZTDs based on GPT2 are again the best and <12.7 mm assuming that USNO ZTDs are the true values.

According to Table 6.2, the RMS errors between the CODE ZTDs and the USNO ZTDs vary from 3.4 mm to 7.5 mm, showing a good consistency. This implies that these two sets of ZTDs are quite stable and sufficiently accurate as the reference data for the validation of PPP-ZTDs. Table 6.3 and Table 6.4 show that GPT2 derived GPS-PPPs are more accurate than those derived using NMF and UNB models. For all 20 stations, the STD and RMS values of PPP-ZTDs GPT2 based on are <12 mm with respect to the CODE ZTDs (refer to Table 6.3) and <12.7 mm with respect to the USNO ZTDs (refer to Table 6.4). Note that a threshold of 15 mm of the retrieved ZTDs is considered to be accurate enough as input to NWP models [*De Haan*, 2006]. Also note that for most stations except PIMO, more than 90% of the real-time epoch-solutions are found within the 20 mm RMS range. According to equation (3.22), 20 mm error in ZTD or ZWD will result in an error of approximately 3 mm in PWV (assuming $\Pi \approx 0.15$). 3 mm is the threshold accuracy for PWV in weather nowcasting [*De Haan*, 2006].

The three stations located in the tropics or subtropics, i.e., COCO, PIMO and SHAO, tend to show larger RMS errors in ZTDs with respect to the reference data as is revealed in Table 6.3 and Table 6.4. Also as is demonstrated in Figure 6.6(e), the PPP-ZTD values (black) at PIMO are obviously smaller than the CODE ZTDs (blue) and USNO ZTDs (red) after DOY 256. This implies that the retrieval of ZTDs in this region is more challenging than in other places, which is also confirmed in the literature [*Dousa and Bennitt*, 2013].

One issue in the retrieval of ZTDs is the internet stability affecting both the GPS data processing centre and the GPS stations, as our data processing highly depends on the real-time collected observations and corrections. If the internet connection of the data processing centre discontinues, the clock and orbit corrections in the offline period will be missing even when the internet is connected again. In addition, the internet stability of the GPS station is also important to provide the real-time observations. The outages of 4.7 h, 2.7 h, 43 h and 11.5 h occur at stations GODE, HERT, STHL and ZIM2, respectively. The internet issue is a key factor contributing to notably larger RMS errors of PPP-ZTDs at these four stations as is shown in Table 6.3 and Table 6.4. There are two solutions if an outage occurs: to retain the variance-covariance matrix in the Kalman filtering, or to enforce BNC software to re-initialize

the processing. The former approach is implemented in this research and demonstrated at station HERT in DOY 255 and 256 shown in Figure 6.6(b) and Figure 6.7. As the variance-covariance matrix is retained, the measurement residual when GPS data resumes is reasonably small hence the corresponding retrieved PPP-ZTD is almost identical to the value at the internet outage.

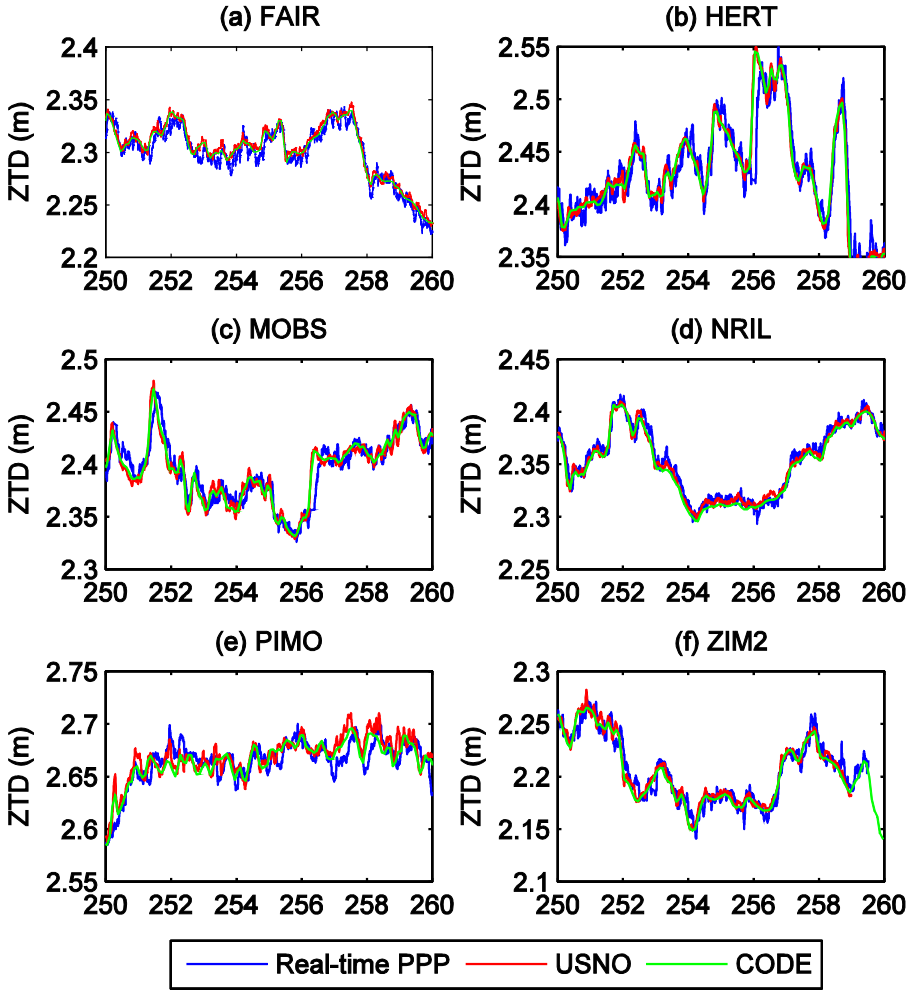

Figure 6.6 ZTDs from real-time PPP, USNO and CODE at six IGS stations during DOY 250-260, 2013. PIMO is a station where PPP-ZTDs show poorer agreement with the reference data. HERT is a station where real-time GPS data suffers from internet instability at the end of DOY 255. The other four stations are presented here for comparison.

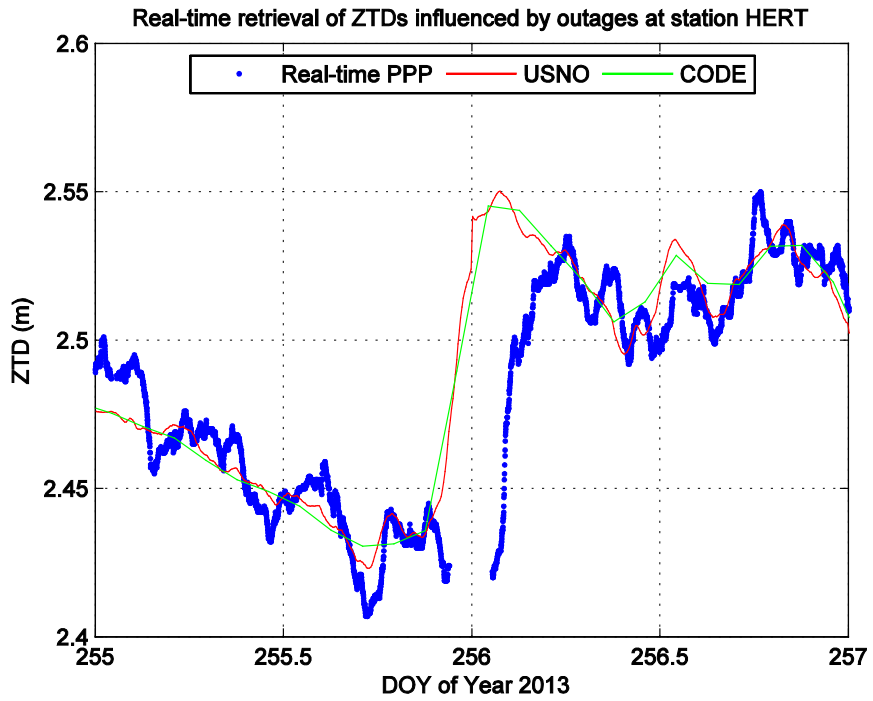

Figure 6.7 Real-time retrieval of PPP-ZTDs at station HERT during DOY 255-257, 2013. An outage of 2.7 hours is found at the end of DOY 255.

6.4 Summary

This chapter presents the experimental results of real-time retrieval of PPP-ZTD. The BNC software used for PPP processing and the corresponding modifications in this research are introduced in detail. These modifications include ocean tide loading corrections, phase centre offset and variation corrections in terms of both satellite and receiver antennas, and the modelling of the tropospheric delays. The real-time observations are collected from 20 global IGS stations using several dedicated selection criteria. The real-time corrections of clocks and orbits from BKG are used. The retrieved ZTDs are compared with IGS tropospheric products from CODE and USNO respectively. It is concluded that PPP-ZTDs are sufficiently accurate and meet the threshold of NWP input requirements and are ready for the conversion to PWVs. The next chapter will deal with this conversion from PPP-ZTD to PPP-PWV.

Chapter 7. Conversion from ZTD to PWV

This chapter mainly presents the experimental results of real-time retrieval of PPP-PWV. PPP-PWV is converted from the previously determined and validated PPP-ZTD by multiplying a factor Π, which is dependent on the weighted mean temperature T_m. There are several models for the determination of T_m. Those models will be compared and the best model will be investigated for its usages in this real-time conversion from ZTD to PWV. In addition, error analyses are conducted to assess the potential accuracy of PPP-PWV in different temperature and humidity conditions.

7.1 Flow Chart of Real-time Retrieval of PPP-PWV

The modelling of the tropospheric delay in this study is based on the classical separation into hydrostatic and wet parts. This will allow ZWD parameters to be estimated from the PPP processing. However, these estimates are not directly converted to PWVs. Instead, a two-step approach is adopted as is demonstrated in the flow chart of PWV retrieval (Figure 7.1). In the first step, the *a priori* ZHDs are used in PPP to retrieve ZTDs. The ZTDs minus accurate ZHDs gives ZWDs which are ready for conversion to PWVs in the second step. There are several considerations for this approach.

1) for weather forecasting, nowcasting or NWP purposes, the PPP processing is implemented at high-resolutions and at many stations simultaneously. This requires that the PPP algorithms particularly the *a priori* ZHD part not being computationally demanding. The GPT2 model is ideal for this purpose, while the VMF1-FC model and the external operational NWP data needs much more computational resources to provide the *a priori* ZHDs particularly at high-resolutions and at many stations simultaneously.

2) any errors in the *a priori* ZHDs derived from GPT2 will be absorbed into the ZWD estimates

in PPP. These ZWD estimates are not accurate enough to provide PWVs if they are directly multiplied by a dimensionless proportionality Π . On the other hand, the ZTDs are accurate i.e. the STD and RMS values of GPT2 based PPP-ZTDs are <12 mm with respect to the CODE ZTDs and <12.7 mm with respect to the USNO ZTDs, respectively. In this context, more accurate ZHDs derived using VMF1-FC can be used and subtracted from ZTDs after PPP processing to obtain the ZWDs.

3) GPS ZTDs rather than ZWDs are typically used in data assimilations. This is optimal as consistent mean temperatures are used [*Bennitt and Jupp*, 2012].

4) ZTD can also provide a long term pressure reference, in particular for dry and polar regions where ZWD is small.

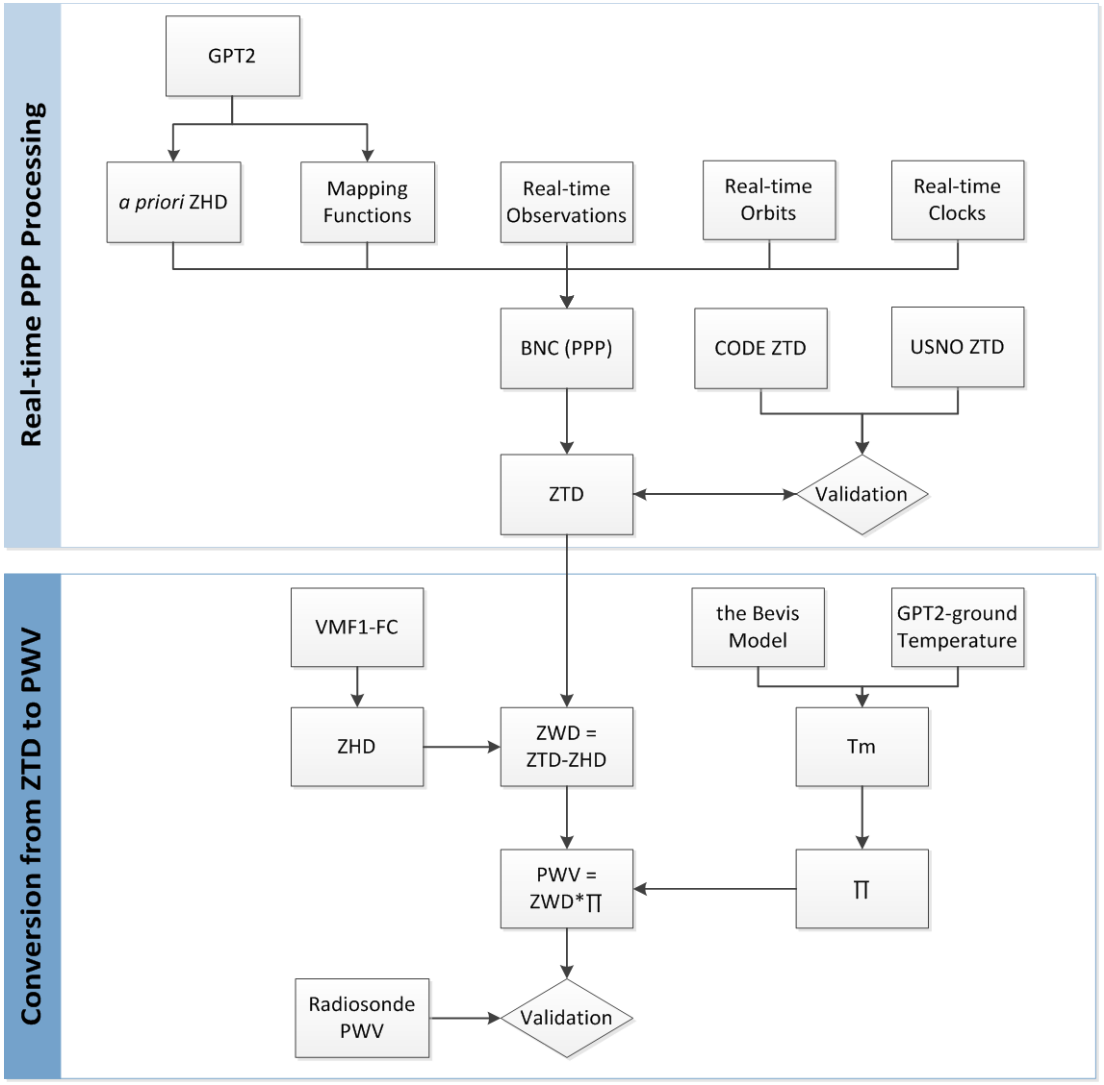

Figure 7.1 Flow chart of real-time retrieval of PWV using the PPP technique. The retrieval is conducted in two steps. The first step is to estimate PPP-ZTD using the modified BNC software and the second step is to convert the retrieved PPP-ZTD to PWV.

As is discussed in Section 3.2.2, the dimensionless constant of proportionality Π for the conversion from ZWD to PWV depends on the weighted mean temperature T_m. Accurate calculation of T_m requires the vertical profiles of water vapour and temperature [*Davis et al.*, 1985]. However, the partial pressure of water vapour and temperature of each profile normally come from radiosondes or NWP models, which is not available for this study on a global scale and in a real-time mode. Instead, two empirical models are tested for the calculation of T_m and then PWV.

7.2 Determination of Weighted Mean Temperature

7.2.1 Relationship Between T_m and T_0

The empirical model presented in [*Bevis et al.*, 1992] is used (denoted as the Bevis model thereafter):

$$T_m \approx 70.2 + 0.72T_0 \tag{7.1}$$

which defines the relationship between T_m and temperature T_0 in Kelvin near the Earth's surface. An RMS error of T_m less than 2% is achievable providing T_0 is available. The surface temperature can be obtained from an empirical model or external meteorological data. The latter is not available hence it needs to be provided by empirical model GPT2. GPT2 provides not only the *a priori* ZHD and mapping functions for PPP processing, but also the temperature near the Earth's surface [*Lagler et al.*, 2013].

Errors in equation (7.1) are affected by two factors: the surface temperature T_0 from GPT2 and the Bevis model for the relationship between T_0 and T_m. GPT2 was developed based on monthly mean profiles in the period of 2001-2010 from ECMWF Re-Analysis (ERA-Interim) [*Dee et al.*, 2011]. Diurnal and sub-diurnal variations which are crucial for high-temporal-resolution applications are not considered. Therefore, the derived T_0 may show a bias in some specific regions and time slots. Similarly the Bevis model also shows a bias in some regions as it was determined from the analysis of 8718 radiosonde profiles between 1989 and 1991 in America [*Bevis et al.*, 1992]. In addition, the Bevis model is developed assuming that there is a strong correlation between T_0 and T_m. However, the correlation is weak for tropical stations and is generally less than 0.5, indicating that variations in T_m are driven by

factors other than just T_0 [*Ross and Rosenfeld*, 1997].

7.2.2 The GTm-III Model

GTm-III is a global empirical model [*Yao et al.*, 2014] to calculate weighted mean temperature T_m based on the previous GTm-I [*Yao et al.*, 2012] and GTm-II [*Yao et al.*, 2013]. GTm-III takes the semi-annual and diurnal variations in T_m into account and takes the initial phase of the cycles as parameters. Its expression is as follows

$$T_m = \alpha_1 + \alpha_2 h + \alpha_3 \cos(\frac{DOY - C_1}{365.25} 2\pi) + \alpha_4 \cos(\frac{DOY - C_2}{365.25} 4\pi) + \alpha_5 \cos(\frac{T_{utc} - C_3}{24} 2\pi) \qquad (7.2)$$

where C_1, C_2 and C_3 are the initial phases of annual, semi-annual and diurnal periodicity, respectively; h is ellipsoid height; T_{utc} is the UTC time; Coefficients $\alpha_1 \sim \alpha_5$ are determined using high-precision Global Geodetic Observing System (GGOS) atmosphere T_m grid data (available: *http://ggosatm.hg.tuwien.ac.at/*).

[*Yao et al.*, 2014] validates the GTm-III model using radiosonde data of year 2012 from 461 globally distributed stations. The mean daily RMS errors are compared in Figure 7.2, which indicates that results from the three models are quite close.

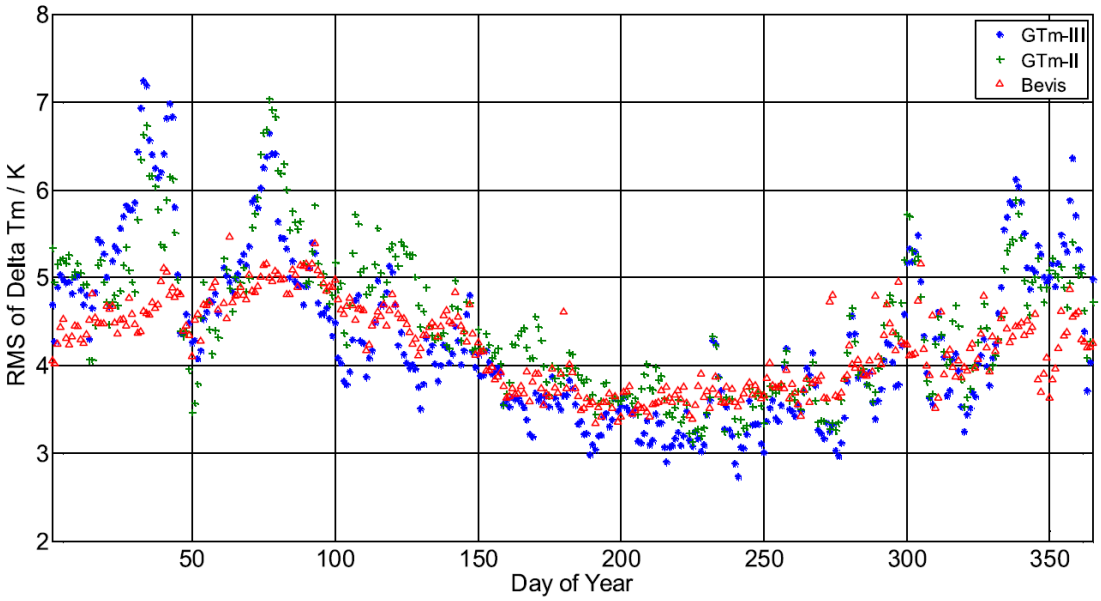

Figure 7.2 Comparison of the selected three models in terms of the mean daily RMS [*Yao et al.,* 2014]. RMS errors are calculated using radiosonde data of 2012 from 461 globally distributed stations. The results show that the calculated weighted mean temperatures are close to each other.

The Bevis and GTm-III models are compared and validated using radiosonde data at the selected 15 IGS stations during September 2013. According to Figure 7.3, the accuracy of GTm-III is better than that of the Bevis and GPT2 combination at most stations. However, the RMS error of GTm-III at the Antarctic station MCM4 is 7.696 K according to [*Yao et al.*, 2014], which means that the performance of GTm-III is unstable at some locations. Hence it is difficult to determine which one of two models (Bevis & GPT2, GTm-III) is superior to the other. When the weighted mean temperatures from the two models are used to compute PPP-PWVs, only small differences (<1 mm) in the resultant PPP-PWVs are found. On the other hand, the results from VMF1 (discussed later) are the most accurate, with RMS <3 K at all the selected 15 stations.

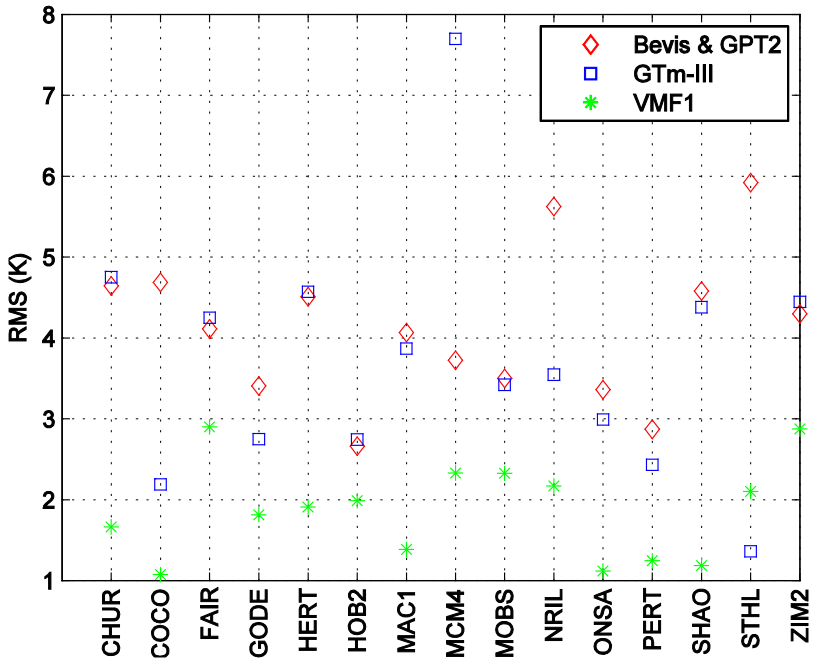

Figure 7.3 RMS errors of the weighted mean temperature (to radiosonde data) derived from the Bevis & GPT2 combination, GTm-III and VMF1 at the selected 15 IGS stations during September 2013.

7.2.3 VMF1 Weighted Mean Temperature for Near Real-time Applications

Recently the Vienna University of Technology announced the VMF1 near real-time mean temperature products (available online: *http://ggosatm.hg.tuwien.ac.at/DELAY/ETC/TMEAN/*). These products are continuously updated based on ECMWF data and can be used as references to investigate the achievable most accurate PPP-PWVs.

Like VMF1-FC, the VMF1 mean temperatures are provided on a global grid (2.0° x 2.5°). A bilinear interpolation based on geodetic coordinates (latitude φ and longitude λ) using neighbouring four grid points is needed. Corrections to the ellipsoidal heights given in the file *orography_ell* (available online: *http://ggosatm.hg.tuwien.ac.at/DELAY/GRID/orography_ell*) are also required. Both considerations have been discussed in Section 4.4.4.

The VMF1 mean temperatures are more accurate than those derived from the Bevis model and

GTm-III as is demonstrated in Figure 7.3. Compared to the radiosonde data during September 2013, RMS valus <3 K from VMF1 mean temperatures at all the selected 15 stations. A more detailed comparison in terms of mean bias, STD and RMS is demonstrated in Figure 7.4. Clearly the RMS error of T_m from Bevis & GPT2 range from 2.6 K at station HOB2 to 5.9 K at STHL, while the RMS error of VMF1 T_m are much smaller and <3 K at all 15 stations.

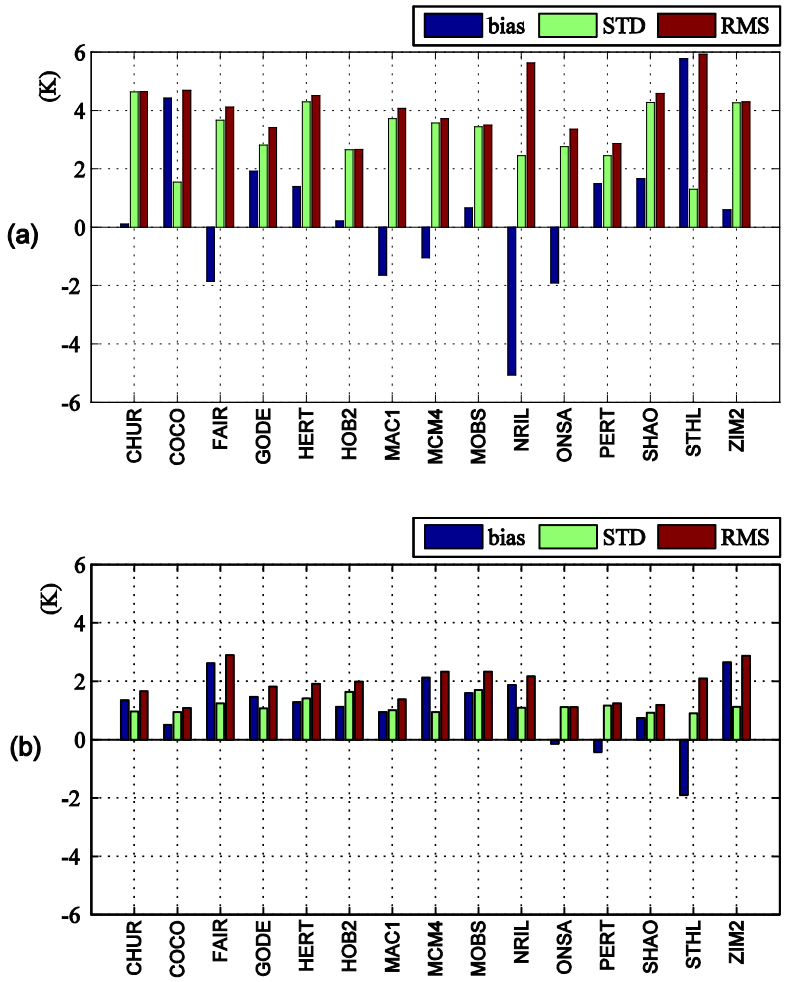

Figure 7.4 Mean bias, STD and RMS errors of the mean temperature T_m derived from the Bevis and GPT2 combination (a), and from VMF1 dataset (b) at the selected 15 IGS stations during September 2013. T_m is validated using the nearby radiosonde data.

7.3 PPP-PWV Results and Validation

7.3.1 Radiosonde Reference Data

The reference data for the validation of PPP-PWVs is retrieved from the radiosonde profiles. The radiosonde balloons are released two to four times per day in multiple locations. *In-situ* atmospheric parameters are collected as the balloons ascend. The radiosonde data is available from a repository of atmosphere profiles provided by NOAA (URL: *http://www.esrl.noaa.gov/raobs/*). Pressure P, temperature T and partial pressure e of water vapour from the radiosonde profiles are used to calculate PWVs. The elevations of the radiosonde sites are converted from the geopotential heights to the ellipsoidal heights using the global geoid model as is provided with GPT [*Boehm et al.*, 2007]. The ZWD z_w along the balloon path is calculated using the equation by *Thayer* (1974):

$$z_w = 10^{-6} \sum N_w ds \tag{7.3}$$

where N_w is a wet refractivity at the particular point (depends only on temperature T and water vapour partial pressure e) in the vertical interpolation model. ds is a vertical distance between consecutive layers of the interpolation model (from the IGS station to the top of the troposphere). N_w is computed using equation (3.15) assuming that the compressibility factor of water vapour Z_v is 1.0. That is

$$N_w = (k_2 - k_1 \frac{M_w}{M_d}) \frac{e}{T} + k_3 \frac{e}{T^2} \tag{7.4}$$

The vertical interpolation model (with 88 layers, from the ground level to 20 km) was set up to consistently validate and interpolate the profile data P, T and e. Wherever the GPS station is located above the co-located radiosonde site, only the observations from the levels above the

GPS receivers are taken into account to calculate ZWD. In the opposite case (GPS receiver below the radiosonde launching site) the levels below the radiosonde site are taken into account by linear extrapolation as PWV is quite linear near the surface [*Li et al.*, 2003]. The radiosonde data was screened for outliers and inconsistencies between the observations. The radiosonde based PWV (denoted as radiosonde-PWV) is obtained using equation (3.22) where z_w is derived from equation (7.4) and the weighted mean temperature T_m is derived from e and T according to equation (3.24) [*Davis et al.*, 1985]. As shown in many GNSS meteorology studies the radiosondes are currently one of the most reliable *in-situ* measurements of pressure, temperature and water vapour [*Rocken et al.*, 1997; *Niell et al.*, 2001; *Revercomb et al.*, 2003]. The accuracy of radiosonde-PWV is better than 1.5 mm according to [*Tregoning et al.*, 1998]. Hence it is an ideal reference for the validation of PPP-PWVs.

7.3.2 PPP-PWVs Validated by Radiosonde Data

The comparison of PWVs between real-time PPP and radiosondes is complicated due to the height issue. Although the surface distance between IGS and radiosonde stations are considered when the IGS stations are selected, the height difference still has a substantial impact on the comparisons. Radiosonde data for nearby IGS stations located at high altitudes (i.e., ABPO, BOGT, HRAO and MKEA. See Table 7.1) tends to provide insufficient information. In addition, if the GPS station is located much lower than the radiosonde one, i.e., PIMO, there would be a significant data gap between the two stations. These radiosonde stations with height issues are regarded as “dubious” and listed in the bottom part of Table 7.1.

Table 7.1 Mean Bias (mm), STD (mm) and RMS (mm) of the differences in PWVs between real-time PPP and radiosonde data during September 2013

IGS Site	GPS Ht[a]	RS. Ht[b]	Dista-nce[c]	PWV[d] (mm)			PWV[e] (mm)		
				Bias	*STD*	*RMS*[f]	*Bias*	*STD*	*RMS*[f]
CHUR	-19	-10	1	0.0	1.5	1.5	0.1	1.5	1.5
COCO	-35	-40	2	0.4	1.9	2.0	0.0	2.0	2.0
FAIR	319	140	25	-0.7	1.4	1.6	-0.5	1.4	1.5
GODE	14	41	56	1.0	1.9	2.2	0.9	1.9	2.1
HERT	83	102	4	0.5	1.8	1.8	0.5	1.6	1.7
HOB2	41	22	4	-0.8	2.1	2.3	-0.7	2.1	2.3
MAC1	-7	-22	2	-0.4	1.5	1.5	-0.3	1.5	1.5
MCM4	98	-22	1	-2.2	0.8	2.4	-2.2	0.8	2.3
MOBS	41	143	22	0.2	1.8	1.8	0.2	1.8	1.8
NRIL	48	43	11	-1.4	0.8	1.6	-1.1	0.7	1.3
ONSA	46	193	38	-0.6	1.7	1.8	-0.5	1.7	1.8
PERT	13	-6	15	-0.1	2.0	2.0	-0.2	2.0	2.0
SHAO	22	11	42	-0.6	2.9	3.0	-0.7	2.7	2.8
STHL	453	447	5	0.2	1.2	1.2	-0.2	1.3	1.3
ZIM2	956	534	40	-1.9	2.1	2.8	-1.7	2.0	2.6
ABPO[g]	1553	1263	36	-2.5	3	3.9	-2.9	3.1	4.2
BOGT	2576	2549	9	-2.3	1.7	2.8	-2.4	1.7	2.9
HRAO	1414	1519	54	-2.1	2.6	3.3	-2.2	2.7	3.5
MKEA	3755	11	41	-4.7	2.1	5.1	-5.5	2.1	5.9
PIMO	96	651	33	3.6	2.9	4.7	3.8	3.0	4.8

[a]Height of IGS stations in metres.

[b]Height of radiosonde stations in metres.

[c]Surface distance in kilometres between IGS and radiosonde stations.

[d]Using T_m derived from GPT2 and the Bevis model in conversion from ZTD to PWV.

[e]Using T_m derived from the VMF1 mean temperature in conversion from ZTD to PWV.

[f]Accuracies of both sets of PPP-PWVs using T_m derived from empirical models and post-processed products, respectively, are at the level of 3 mm.

[g]The five stations at the bottom part of the table are less conclusive due to the height issues.

Two sets of PPP-PWVs are calculated based on different T_m in conversion from ZTD to PWV. According to Table 7.1, the RMS errors of both sets of PPP-PWVs are encouraging, if the five suspicious stations with height issues are excluded from analyses. The corresponding STD and

RMS values at all other 15 stations are found to be ≤3 mm which meets the accuracy requirement of weather nowcasting.

It is interesting that minor differences of RMS errors (below 10%) in PPP-PWVs are observed if different T_m is used. Only at station NRIL, an approximately 20% improvement of RMS error is demonstrated if the more accurate VMF1 mean temperatures are used. However, T_m seems to have a larger impact on mean bias than on STD, particularly at stations COCO, FAIR, NRIL and ZIM2. The impact of T_m on the accuracy of the retrieved PPP-PWVs is discussed further in the followed Section 7.4.

7.4 Error Analyses

7.4.1 Error Budget

In our retrieval of PWVs, a number of models and datasets are used. Each step of the process is performed with a certain degree of accuracy and can also introduce its own instrumental or computational errors. It is therefore important to analyse the errors of the retrieved PWVs from different sources. According to equations (3.32) and (3.33), let $k_2^{'} = k_2 - k_1 \frac{M_w}{M_d}$,

$$PWV = (z_t - z_h) \cdot \frac{10^6 M_w}{\rho R \left(k_2^{'} + \frac{k_3}{T_m} \right)} \tag{7.5}$$

where ρ, R, M_w, M_d, k_1, k_2 and k_3 are constants. Assuming the RMS error of z_t (σ_t), z_h (σ_h) and T_m (σ_{T_m}) are Gaussian and independent from each other, the RMS error of PWV is

$$\sigma_{PWV} = \sqrt{\left(\frac{10^6 M_w}{\rho R\left(k_2' + \frac{k_3}{T_m}\right)}\right)^2 \left(\sigma_t^2 + \sigma_h^2\right) + \left(\frac{10^6 M_w k_3}{\rho R\left(k_2' T_m + k_3\right)^2}\right)^2 z_w^2 \sigma_{T_m}^2} \tag{7.6}$$

The RMS errors from different error sources need to be quantified to further quantify the magnitude of their influence on the resultant PPP-PWVs. From the above validation of PPP-ZTDs at 20 global stations in the period of 30 days, RMS errors of PPP-ZTDs range from 5.6 mm at MCM4 to 11.9 mm at STHL, with a median value of 10.2 mm at PERT if CODE ZTDs are compared. According to the validation using radiosonde data in Figure 7.4, the RMS errors of T_m from GPT2 and Bevis model range from 2.6 K at station HOB2 to 5.9 K at STHL, while the RMS errors of VMF1 T_m are much smaller and <3 K at all 15 stations.

ZHD exerts the same level of effect as PPP-ZTD on PWV according to equation (7.6). The very accurate ZHD is usually calculated based on pressure data which is obtained from *in-situ* barometers, interpolated synoptic data or NWP models. Variation of 1 hPa in surface pressure is supposed to introduce 2.3 mm accuracy loss in ZHD. If *in-situ* pressure data is not available then the RMS error of ZHD (σ_h) using empirical models tends to be larger. According to the validation of ZHDs in Section 4.6, stations with RMS errors <15.3 mm account for 95% of the 71 stations if VMF1-FC is used. Therefore, the previous discussions demonstrate that

$$\begin{cases} \sigma_t < 12\,mm & (to\ CODE\ ZTDs) \\ \sigma_h < 15.3\,mm & (VMF1-FC, 95\%\ stations) \\ \sigma_{T_m} < 6\,K & (GPT2\ and\ the\ Bevis\ model) \end{cases} \tag{7.7}$$

In addition, T_m derived from the radiosonde data in September 2013 varies from 238 K at MCM4 to 294 K at SHAO with a median value of 277 K at MOBS, while ZWD varies from 0.003 m at MCM4 to 0.383 m at SHAO with a median value of 0.097 m at NRIL.

7.4.2 Theoretical Accuracy of PPP-PWV in Different Climatic Conditions

Equation (7.6) is a strictly increasing function of variables z_w, σ_t, σ_h and σ_{T_m}. To clarify the relationship between the RMS errors of PPP-PWVs and the variations of T_m, we take the first order partial derivative of σ_{PWV} with respect to T_m:

$$\frac{\partial \sigma_{PWV}}{\partial T_m} = \frac{10^{12} k_3 M_w^2}{\rho^2 R^2 \left(k_2' T_m + k_3\right)^5 \sigma_{PWV}} \left(T_m \left(k_2' T_m + k_3\right)^2 \left(\sigma_t^2 + \sigma_h^2\right) - 2 k_2' k_3 z_w^2 \sigma_{T_m}^2 \right) \tag{7.8}$$

Simulations prove that $\frac{\partial \sigma_{PWV}}{\partial T_m}$ is constantly positive in a typical retrieval of PPP-PWV, assuming that $z_w \in [0,\ 0.6]$ m, $T_m \in [273-40,\ 273+40]$ K, $\sigma_t \in [3,\ 12]$ mm, $\sigma_h \in [1,\ 15.3]$ mm, and $\sigma_{T_m} \in [0,\ 6]$ K. These assumptions are reasonable according to previous discussions. This reveals that equation (7.6) is a strictly increasing function of variable T_m. In other words, the retrieval of PPP-PWV is more challenging in conditions of higher weighted mean temperatures.

To thoroughly investigate the magnitude of the errors in PWV introduced by PPP-ZTDs, VMF-FC derived ZHDs and T_m, three different temperature and humidity conditions defined by T_m and ZWD are tested: 1) $T_m = 238\,K$ and $z_w = 0.003\,m$ in polar regions like station MCM4, where it is cold and dry, 2) $T_m = 294\,K$ and $z_w = 0.4\,m$ in the tropics or subtropics like stations SHAO and COCO, where it is hot and humid, and 3) $T_m = 277\,K$ and $z_w = 0.1\,m$ in moderate conditions like CHUR, HERT, MOBS, ONSA, PERT, and ZIM2.

Figures 7.5(a) – 5(c) show the theoretical accuracies of PPP-PWVs in the three different conditions, assuming that PPP-ZTDs are at the accuracy level of 12 mm. In polar regions where

the air is extremely dry, the accuracy of ZHD dominates the magnitude of σ_{PWV} while the accuracy of T_m has little influence. With the increase of mean temperature T_m, the error component of T_m increases correspondingly. In Figure 7.5(c) for tropical or subtropical regions, the T_m component accounts for more than the ZHD component does. This implies that in the tropics or subtropics, the mean temperature T_m derived from GPT2 and the Bevis model shows its disadvantages of insufficient accuracy for the conversion from ZTD to PWV.

Assuming that the RMS error of T_m and ZHD are small or even negligible, the retrievable accurate PWV is then determined by factor Π which is further determined by T_m. T_m values of 238 K (polar), 277 K (moderate) and 294 K (tropical or subtropical) lead to Π values of 0.135, 0.157 and 0.167, corresponding to achievable PPP-PWV accuracies of 1.6 mm, 1.9 mm and 2.0 mm if PPP-ZTDs are at the accuracy level of 12 mm.

Note in polar regions the RMS error of PPP-ZTDs is relatively small (below 8 mm according to Section 6.3). Hence the derived PWV in Figure 7.5(d) is more optimistic than in Figure 7.5(a). On the contrary, the RMS error of PPP-ZTDs in the tropics or subtropics tends to be bigger; hence, the retrieval of PWVs is rather challenging as is discussed previously and shown in Figure 7.5(e). The contour lines in Figure 7.5 clearly show the accuracy requirements of T_m and ZHD for different accuracy levels of PPP-PWVs. In polar condition (Figure 7.5(a) and Figure 7.5(d)) and moderate condition (Figure 7.5(b)), it is not challenging to obtain PWV at an accuracy level of 3 mm even if the accuracy of T_m is very poor. Most of the 20 selected stations in this investigation belong to these two cases. This may explain why only minor differences are demonstrated in the retrieved PPP-PWVs when different sets of T_m are used. However, in high temperature and humidity conditions (Figure 7.5(c) and Figure 7.5(e)), all the three components PPP-ZTD, ZHD and mean temperature T_m should be computed accurately.

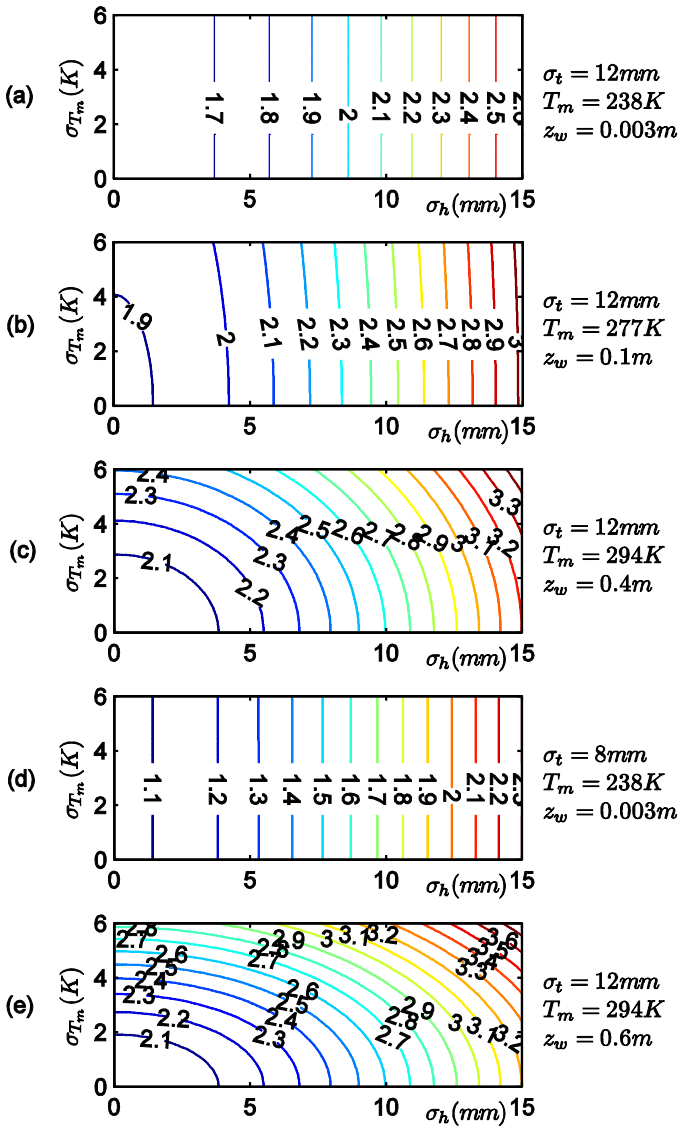

Figure 7.5 The theoretical accuracies of PPP-PWVs in different climatic conditions defined by σ_t (RMS error of PPP-ZTDs), T_m (weighted mean temperature) and z_w (ZWD): (a and d) polar regions where it is cold and dry; (c and e) tropical or subtropical regions where it is hot and humid; and (b) moderate conditions. Figure 7.5(d) differs from Figure 7.5(a) assuming PPP-ZTDs are more accurate (smaller σ_t), while Figure 7.5(e) differs from Figure 7.5(c) assuming higher relative humidity (larger z_w). The contour lines also show the accuracy requirements of T_m and ZHD for different accuracy levels of PWVs.

7.5 Summary

This chapter presents the experimental results of PPP-PWVs converted from the retrieved PPP-ZTDs. The conversion depends on the determination of weighted mean temperature which can be determined using models: the combination of GPT2 and the Bevis model, GTm-III and VMF1. After comparisons between these models, the combination of GPT2 and the Bevis model is proved sufficiently accurate, easily implemented and hence ideal for this research.

It is shown that the retrieved PPP-PWVs in comparison with radiosonde data are at the accuracy level of 3 mm, which can meet the need of weather nowcasting. The 3 mm accuracy-level is also theoretically proved to be achievable according to error analyses. In this chapter the theoretical accuracy of PPP-PWV in various conditions of temperature and humidity are also discussed. It is concluded that the RMS error of PWV is a strictly increasing function of ZWD and weighted mean temperature. Hence the retrieval of PPP-PWV is more challenging in higher temperature and humidity conditions.

All these analyses are based on GPS measurements. The next chapter will deal with the retrievals of ZTDs under a multi-GNSS scenario.

Chapter 8. Real-time Retrieval of PPP-ZTD Using Multi-GNSS Data

This chapter mainly presents the experimental results of real-time retrieval of PPP-ZTD using current multi-GNSS observations and products. As a preliminary study, observations of GPS and GLONASS are taken into account. The functional model will be setup, which is slightly different from that of the satellite positioning using a sole GPS constellation due to the inter-system bias. As the number of satellites in view increases when GLONASS is included, the PDOP and GDOP indices are improved accordingly. Therefore, it is expected that the accuracy of PPP-ZTD will be improved. However, the experimental results at the selected 12 stations indicate that adding GLONASS data degrades the accuracy of PPP-ZTD. As such, the potential sources of this accuracy degradation need to be investigated.

8.1 Observation Equations Using GPS and GLONASS Observations

The observation equations of GLONASS or other GNSSes are similar to those of GPS which have been discussed in Section 2.5. Therefore, the pseudorange and phase observations on one frequency such as L1, i.e., equations (2.5) and (2.7), can be re-expressed for a specific GNSS system

$$\begin{aligned}\Phi_1^i(t) = {} & \rho^i(t) + cdt_{rcv}^i(t) - cdt_{sat}^i(t) + d_{ant}^i + d_{rot}(t) \\ & + d_{rel}(t) + d_{otl}(t) + d_{set} + T^i(t) - I^i(t) + \frac{c}{f_1} N_1^i + d_{windup}^i + \varepsilon_{\Phi 1}^i\end{aligned} \tag{8.1}$$

and

$$\begin{aligned}P_1^i(t) = {} & \rho^i(t) + cdt_{rcv}^i(t) - cdt_{sat}^i(t) + d_{ant}^i + d_{rot}(t) \\ & + d_{rel}(t) + d_{otl}(t) + d_{set} + T^i(t) + I^i(t) + \varepsilon_{P1}^i\end{aligned} \tag{8.2}$$

where superscript ^{i} indicates the specific GNSS constellation, i.e. *G* represents GPS, *R* represents GLONASS, *C* represent BDS and *E* represents Galileo [*Leick*, 2004; *Xu*, 2007]. Taking the modelling of tropospheric delay into account, the corresponding ionosphere-free combinations on L1 and L2 are

$$\Phi_{IF}^{i}(t) = \rho^{i}(t) + mf_{w}^{i} \cdot z_{w} + cdt_{rcv}^{i}(t) + N_{IF}^{i} + e_{\Phi}^{i} \tag{8.3}$$

$$P_{IF}^{i}(t) = \rho^{i}(t) + mf_{w}^{i} \cdot z_{w} + cdt_{rcv}^{i}(t) + e_{P}^{i} \tag{8.4}$$

where e_{P}^{i} and e_{Φ}^{i} contain the effects of the Earth rotation, ocean tide loading, solid Earth tide, the satellite phase wind up, etc. Equations (8.3) and (8.4) constitute the functional model of multi-GNSS PPP processing used in BNC. In previous studies [*Chen et al.*, 2013; *Montenbruck*, 2014] it is concluded that GNSS signals are influenced by biases induced by satellite and receiver hardware when they are transmitted and received through corresponding channels. Those hardware delays are dependent on the signal frequencies and receiver hardware. For a pseudorange and phase observation, hardware delay includes a satellite-related part and receiver-related part. The good news for this research is that the receiver-related part, either in a pseudorange or phase observation, can be absorbed in clock offset item $cdt_{rcv}^{i}(t)$. The satellite-related part in a phase observation can be absorbed by ambiguity N_{IF}^{i}, while the satellite-related part in a pseudorange is relatively small and can be neglected considering the code observations are assigned much smaller weighting [*Cai and Gao*, 2013; *Cai et al.*, 2014]. Therefore, equations (8.3) and (8.4) still holds for the retrieval of PPP-ZTD using multi-GNSS data.

Note that the receiver clock offsets $dt_{rcv}^{i}(t)$ for GPS and GLONASS are different, which leads to ISB. In other words, in multi-GNSS PPP another parameter in addition to the GPS clock offset has to be introduced to address the GLONASS clock offset. In this research, the GLONASS clock offset is directly estimated together with station coordinates and ambiguities.

Hence the corresponding parameters to be estimated at each epoch in multi-GNSS PPP are

$$\hat{X} = \begin{bmatrix} x & y & z & z_w & dt_G & N^{*1}_G & \cdots & N^{*m}_G & dt_R & N^{*1}_R & \cdots & N^{*n}_R \end{bmatrix}^T \tag{8.5}$$

as contrast to the parameters in the GPS-only scenario, i.e., equation (5.5). In equation (8.5) m and n represent the numbers of GPS and GLONASS satellites, respectively; dt_G and dt_R represent GPS and GLONASS receiver clock parameters, respectively; $N^{*1}_G \cdots N^{*m}_G$ and $N^{*1}_R \cdots N^{*n}_R$ represent corresponding ambiguity parameters.

This approach of addressing ISB is easily to be implemented. It actually takes phase IFB into account as well. As introduced in Table 2.1 in Section 2.2, GLONASS uses a FDMA technique to distinguish the signals coming from different satellites. The GLONASS L1 and L2 bands are divided into 14 sub-bands, and each satellite transmits in one of these sub-bands. IFB are the errors due to frequency differences. *Chen et al.* (2013) demonstrate that in GLONASS data processing, the positioning accuracy will slightly be influenced if IFB is not taken into account. In this research phase IFB is virtually absorbed into the corresponding ambiguity parameters according to equations (8.3) – (8.5).

8.2 Dilution of Precision in the Context of Multi-GNSS

One prominent advantage of multi-GNSS against the GPS-only constellation is the improved availability of visible satellites. To illustrate this improvement, five global stations located in polar, equatorial, and middle-latitude regions are selected for tests. The distribution of these stations is shown in Figure 8.1, with satellite availabilities displayed in Figure 8.2. The five stations in Figure 8.2 are located geographically from north to south. Stations NYA1 and CAS1 are located at the polar regions; Stations WUHN and MOBS are located at the middle-latitude regions and NTUS is located at the equatorial regions. As can be seen in Figure 8.2, each station has an average of 8-12 GPS satellites visible. If GLONASS satellites are considered, the

average number of satellites visible increases to 14-22 when the cutoff elevation angle is set to 10°. Particularly in polar regions, there are up to 25 satellites visible at some epochs.

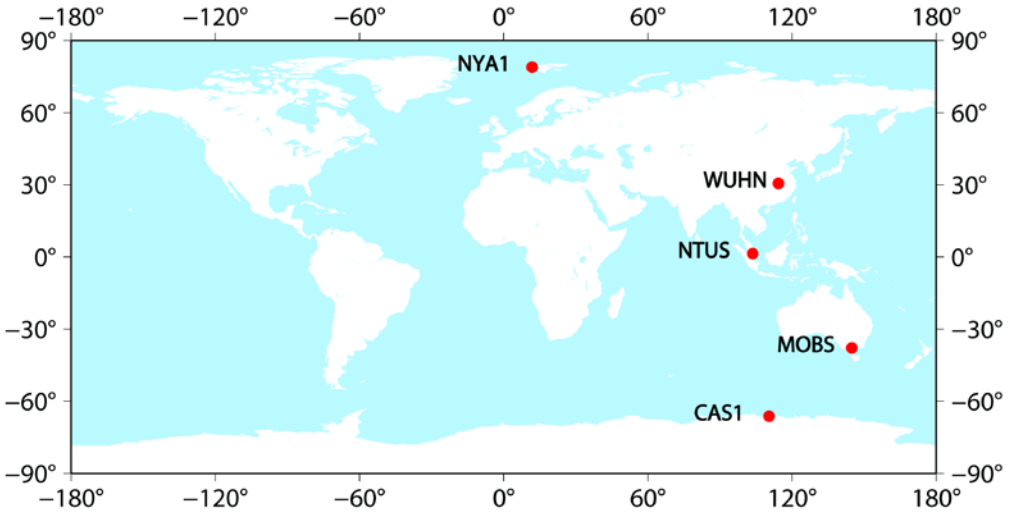

Figure 8.1 Distribution of the five IGS stations selected for the demonstration of satellite visibility. These five stations are located at the polar, equatorial, and middle-latitude regions, respectively.

DOP is a concept used to see how errors in the measurement affect the final state estimation. Two DOP indices: PDOP and GDOP are typically used. The PDOP index is the combination of both the horizontal and vertical components of position error caused by satellite geometry, while GDOP also addresses the receiver clock offset [*Langley*, 1999]. The calculation of DOP values is based on a design matrix in terms of four unknowns, namely three position components and one receiver clock offset [*Chen et al.*, 2011]. Formulate covariance matrix Q :

$$Q = (A^T A)^{-1} = \begin{bmatrix} \sigma_x^2 & \sigma_{xy} & \sigma_{xz} & \sigma_{xt} \\ \sigma_{xy} & \sigma_y^2 & \sigma_{yz} & \sigma_{yt} \\ \sigma_{xz} & \sigma_{yz} & \sigma_z^2 & \sigma_{zt} \\ \sigma_{xt} & \sigma_{yt} & \sigma_{zt} & \sigma_t^2 \end{bmatrix} \tag{8.6}$$

where (x, y, z, t) are four unknowns. Then

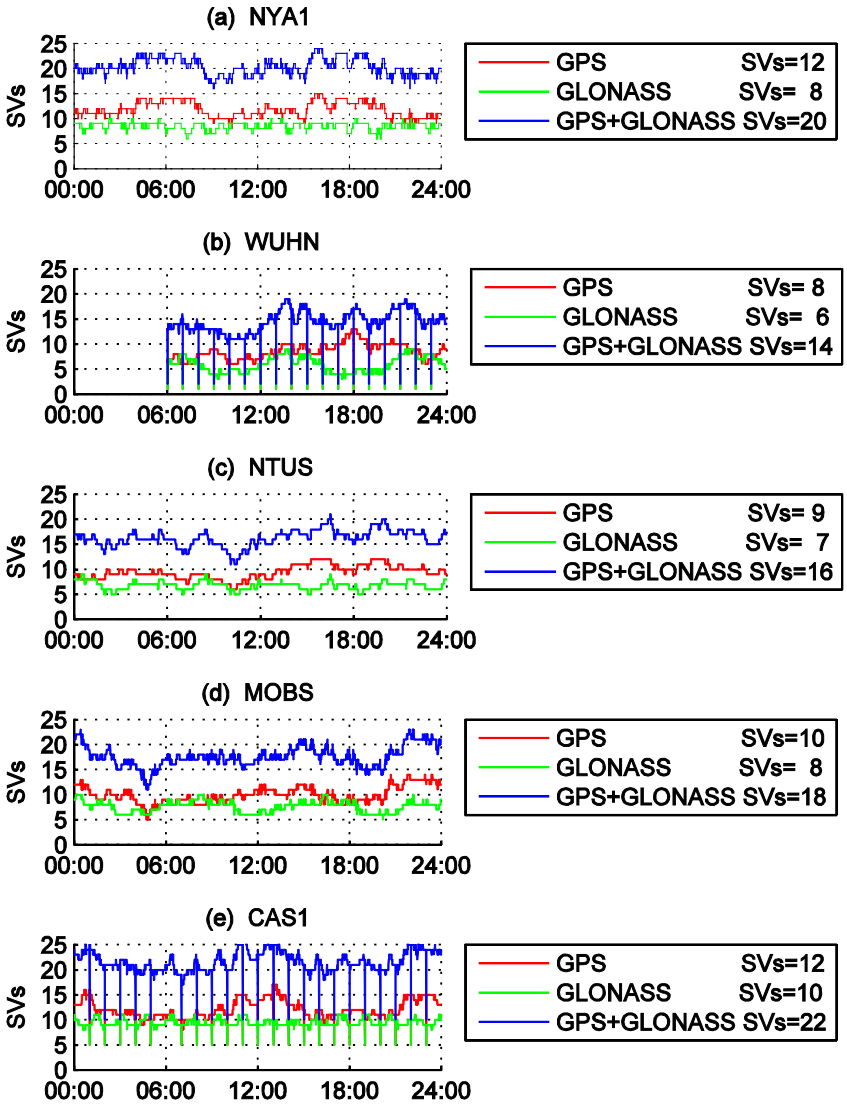

Figure 8.2 Satellite availability in terms of GPS only, GLONASS only and GPS+GLONASS at five IGS stations. The horizontal axes represent the UTC time of DOY 012, 2014 while the vertical axes represent the numbers of satellites visible (SVs). Average SVs are displayed in the legends. The drop-outs at stations WUHN and CAS1 are due to the lack of observations.

$$PDOP = \sqrt{\sigma_x^2 + \sigma_y^2 + \sigma_z^2} \tag{8.7}$$

$$GDOP = \sqrt{\sigma_x^2 + \sigma_y^2 + \sigma_z^2 + \sigma_t^2} \tag{8.8}$$

The DOP values at the selected five stations are shown in Figure 8.3. As can be seen in this figure, DOP values at most epochs are <2 if GLONASS observations are included. According to [*Texas Tech University*, 2014], DOP <2 are ranked as “excellent”, indicating that positional measurements are considered accurate enough to meet all but the most sensitive applications. On the contrary, the GPS-only scenarios lead to much higher DOP values, indicating that at some epochs, the corresponding data processing is not reliable or there are even not enough observations for processing. This can be further proved by Figure 8.2. Particularly at mid-altitude stations WUHN and MOBS, there are approximately five GPS satellites visible at some epochs. If observations from one or two satellites are taken as outliers, there would not be enough observations for the estimation of three coordinate parameters, one receiver clock offset, one ZWD parameter, and ambiguities which are as many as used satellites.

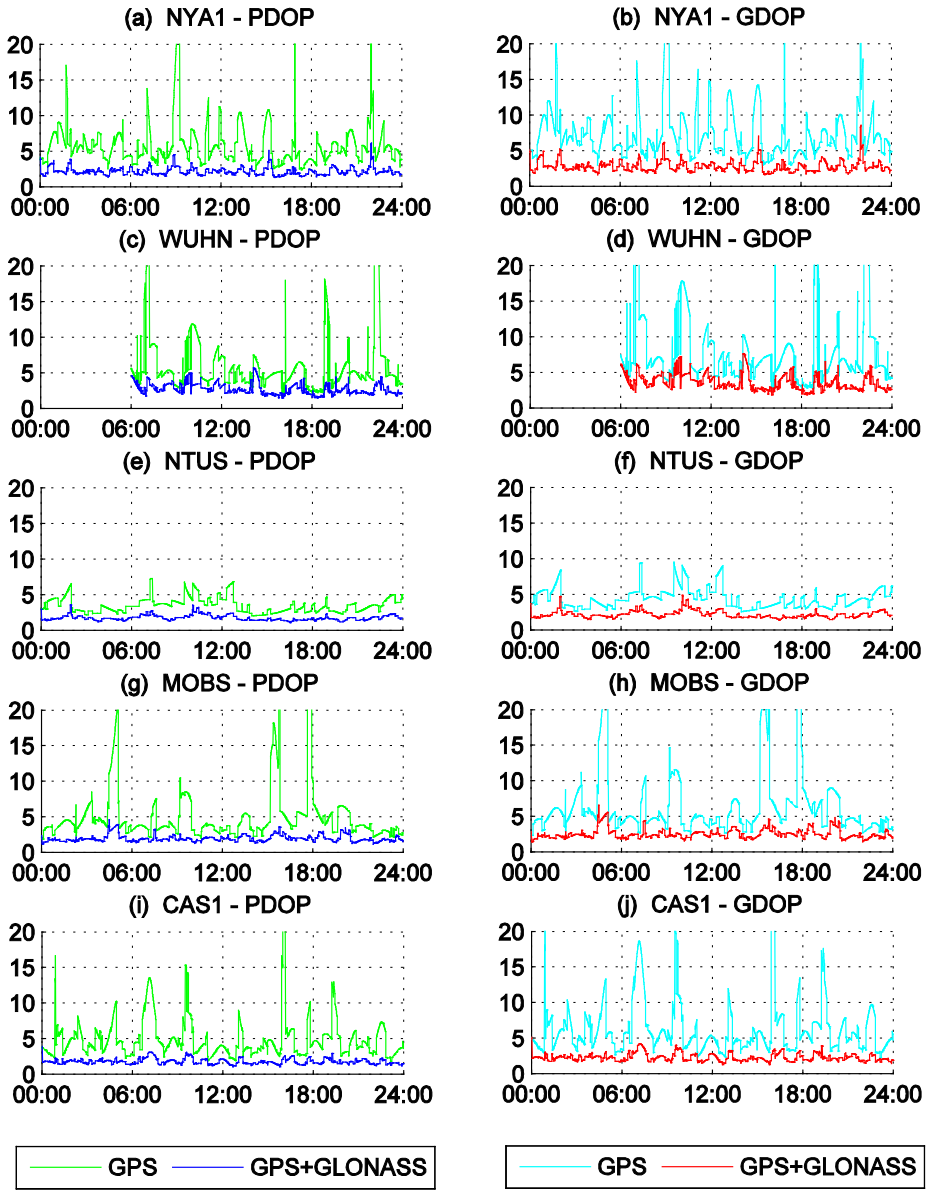

Figure 8.3 PDOP and GDOP indices with a cutoff elevation angle of 10° at the selected five stations during DOY 012, 2013.

8.3 Real-time Corrections

In Chapter 6 for the retrieval of PPP-ZTD using GPS observations, two types of SSR messages i.e. 1057 and 1058 are used to account for the orbit and clock corrections. If GLONASS observations are also considered to retrieve PPP-ZTD, extra orbit and clock corrections for

GLONASS are needed. GLONASS orbit and clock corrections can be provided in messages 1063 and 1064, or in message 1066 with combined corrections to GLONASS ephemeris.

Currently there are a number of correction streams made available as a common effort of EUREF and IGS. Table 8.1 summarises the correction streams that can be used for the retrieval of PPP-ZTD using GPS and GLONASS observations. It should be noted that the IGS03 corrections are derived using BNC using the same approach as is implemented for IGS02. Hence the IGS03 corrections are selected for this multi-GNSS PPP processing.

Table 8.1 Current correction streams which 1) include both GPS and GLONASS corrections, and 2) are referred to Antenna Phase Centre (APC) rather than CoM

Caster IP:Port	Mountpoint & Input Streams	Messages	Analysis Centre & Software
products.igs-ip.net:2101	IGS03	1057,1058,1059 1063,1064,1065	KF Combination BNC
www.euref-ip.net:2101	EUREF02	1057,1058,1059 1063,1064,1065	KF Combination BNC
products.igs-ip.net:2101	CLK11	1059,1060 1065,1066	BKG RTNet + BNC
products.igs-ip.net:2101	NAD8302	1057,1058,1059 1063,1064,1065	BKG RTNet + BNC
products.igs-ip.net:2101	GDA9402	1057,1058,1059 1063,1064,1065	BKG RTNet + BNC
products.igs-ip.net:2101	SIRGAS200002	1057,1058,1059 1063,1064,1065	BKG RTNet + BNC
products.igs-ip.net:2101	SIRGAS9502	1057,1058,1059 1063,1064,1065	BKG RTNet + BNC
www.gref-ip.de:2101	DREF9102	1057,1058,1059 1063,1064,1065	KF Combination BNC
products.igs-ip.net:2101	CLK91	1059,1060 1065,1066	CNES PPP-Wizard + BNC
wox.geopp.de:2101	RTCMSSR	1057,1058,1059 1063,1064,1065	Geo++ GNSMART
wox.geopp.de:2101	RTCMSSR1060	1059,1060 1065,1066	Geo++ GNSMART

8.4 Real-time PPP-ZTDs Using Multi-GNSS Observations

For the retrieval and variation of PPP-ZTD using GPS observations, 20 globally distributed IGS stations are selected. However, GLONASS observations are not available at some stations. Hence for the retrieval tests using multi-GNSS observations, another set of 12 globally distributed IGS stations are used. When it comes to different signals and different GNSSes in data processing, the weighing of individual signals is still an issue up to date [*Montenbruck*, 2014]. The original weighting of GPS signals vs. GLONASS signals in BNC is 5:1, assuming that the noises of GLONASS observations are five times as big as GPS observations. It would also be interesting to see the experimental results if weighting is set as 1:1, assuming that the accuracies of GLONASS and GPS observations are similar. Both sets of weighing are tested in this research. Figure 8.4 shows the comparisons of ZTDs from real-time PPP, USNO and CODE at the selected four stations. As can be seen in this figure, the PPP-ZTDs derived from GPS only agree well with reference data from USNO and CODE. Those derived from multi-GNSS with weighing 5:1 are slightly less accurate. When the weighting is set as 1:1, the PPP-ZTDs from multi-GNSS deviate much more, indicating that adding GLONASS observations degrades the accuracies of PPP-ZTDs.

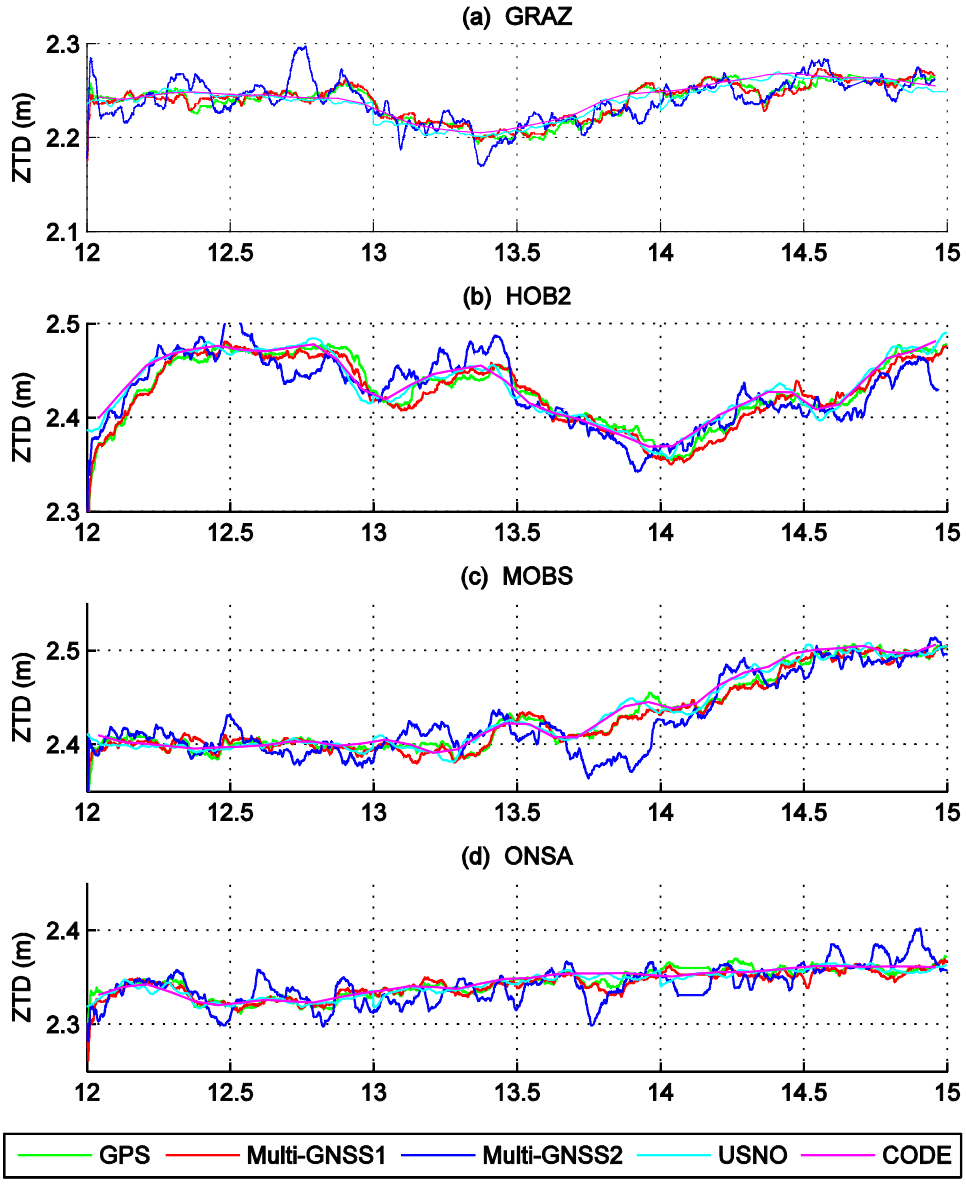

Figure 8.4 ZTDs derived using real-time observations from GPS only and GPS+GLONASS as validated using tropospheric products from USNO and CODE. Multi-GNSS1 represent the results using weighing 5:1 while Multi-GNSS2 represent the results using weighing 1:1. The horizontal axes represent DOY 012-014, 2014, while the vertical axes represent the PPP-ZTDs. This figure shows that the inclusion of GLONASS observations degrades the accuracies of PPP-ZTDs.

A more detailed statistical analysis is demonstrated in Table 8.2 and Table 8.3. As is expected,

the RMS errors of PPP-ZTDs using GPS only are similar to those discussed in Section 6.3. RMS errors at most stations are <10 mm. Only at stations TOW2 and PERT, RMS errors reach 11.6 mm and 13.2 mm, respectively. However, RMS errors increase to up to 20 mm if GLONASS observations are included and taken as accurate as the GPS ones. That is why in multi-GNSS data processing, the GLONASS observations are usually down-weighted [*Xu*, 2007; *Dach et al.*, 2010]. According to the 'Bias' and 'STD' columns, these degraded accuracies suffer from higher STDs while the biases contribute less.

Table 8.2 Mean Bias (mm), STD (mm) and RMS (mm) of the differences between real-time PPP-ZTDs and CODE-ZTDs during DOY 012-014, 2014

Sites	1) GPS only[a]			2) Multi-GNSS[b]			3) Multi-GNSS[c]		
	Bias	*STD*	*RMS*	*Bias*	*STD*	*RMS*	*Bias*	*STD*	*RMS*
ALIC	1.6	7.8	8	2.5	8	8.4	-1.8	15	15.1
COCO	3.1	7.4	8	1	8.8	8.9	1	8.8	8.9
DAV1	1.5	6.1	6.3	2.6	6.3	6.9	-2	11.6	11.8
GRAZ	2.9	8.7	9.2	2.2	10.5	10.8	2.9	13.8	14.1
HERT	1.6	9.8	9.9	0.5	9.7	9.7	1.4	11.9	11.9
HOB2	2.5	9.5	9.8	6.2	10.8	12.5	5.3	18	18.8
MOBS	4	7.4	8.4	6.5	7.6	10	7.6	19.2	20.6
NTUS	3.1	7.5	8.1	-1.5	7.6	7.7	1.8	10.5	10.6
ONSA	1.5	5.5	5.7	3.2	6.2	7	2.6	13.9	14.1
PERT	-7.4	10.9	13.2	-1.8	9.5	9.7	5.1	15.7	16.5
STHL	-0.8	9.6	9.6	-1.1	9.8	9.8	-3.5	15.2	15.6
TOW2	2	11.4	11.6	-1.1	10.5	10.6	-2	15.7	15.8

[a]PPP algorithms are implemented using observations from GPS only.

[b]PPP algorithms are implemented using GPS and GLONASS observations with weighting 5:1.

[c]PPP algorithms are implemented using GPS and GLONASS observations with weighting 1:1.

Table 8.3 Mean Bias (mm), STD (mm) and RMS (mm) of the differences between real-time PPP-ZTDs and USNO-ZTDs during DOY 012-014, 2014

Sites	1) GPS only[a]			2) Multi-GNSS[b]			3) Multi-GNSS[c]		
	Bias	*STD*	*RMS*	*Bias*	*STD*	*RMS*	*Bias*	*STD*	*RMS*
ALIC	2.4	8.7	9	2.6	9.4	9.8	-1.9	15.5	15.6
COCO	4.4	8.5	9.6	1.4	10.4	10.5	1.4	10.4	10.5
DAV1	7.3	7.4	10.3	8.1	6.4	10.3	4.7	11.9	12.7
GRAZ	0.3	9.3	9.3	-1	10.1	10.2	-0.1	15.5	15.5
HERT	1.2	10	10.1	-0.1	10	10	1.5	11	11.1
HOB2	1.9	10.1	10.3	4.8	11.6	12.6	3.9	18.6	19.1
MOBS	2	8	8.3	3.6	8.4	9.1	6.1	20.8	21.7
NTUS	5.7	8.6	10.3	0.6	9.1	9.1	2.3	10.9	11.1
ONSA	0.4	5.1	5.1	2.2	6.1	6.5	1.7	15.2	15.3
PERT	-6.4	10.7	12.5	-1.4	10.4	10.5	2.7	17.1	17.3
STHL	-0.6	10.8	10.8	-0.2	9.7	9.7	-2.3	18.2	18.3
TOW2	3.9	12.2	12.8	0.3	11.7	11.7	-0.6	15.4	15.4

[a]PPP algorithms are implemented using observations from GPS only.

[b]PPP algorithms are implemented using GPS and GLONASS observations with weighting 5:1.

[c]PPP algorithms are implemented using GPS and GLONASS observations with weighting 1:1.

8.5 Sources of the Accuracy Degradation

8.5.1 Deficiencies in the Functional Model

In theory the nearly doubled number of visible satellites and the significantly improved DOP values are expected to improve the accuracies of PPP-ZTDs. However, the retrieved PPP-ZTDs using multi-GNSS observations are less accurate with RMS errors up to 20 mm. The potential sources of the relatively lower accuracy of multi-GNSS ZTDs include deficiencies in the functional model and less accurate GLONASS orbits and clocks.

The functional model using equations (8.3) and (8.4) contains two clock offsets per epoch: one

for GPS and another for GLONASS. Both are taken as white noises in the Kalman filtering. In some other studies [*Cai and Gao*, 2013; *Chen et al.*, 2013], an ISB parameter indicating the difference of receiver clocks between two GNSSes is introduced:

$$dt_{rcv}^{R}(t) = dt_{rcv}^{G}(t) + t_{ISB} \tag{8.9}$$

where GLONASS receiver clock offset $dt_{rcv}^{R}(t)$ is expressed as the sum of GPS receiver clock offset $dt_{rcv}^{G}(t)$ and the system time difference t_{ISB} between GPS and GLONASS. Consequently, equations (8.3) and (8.4) for GPS are kept unchanged while for GLONASS are re-written as

$$\Phi_{IF}^{R}(t) = \rho^{R}(t) + mf_{w}^{R} \cdot z_{w} + cdt_{rcv}^{G}(t) + t_{ISB} + N_{IF}^{R} + e_{\Phi}^{R} \tag{8.10}$$

and

$$P_{IF}^{R}(t) = \rho^{R}(t) + mf_{w}^{R} \cdot z_{w} + cdt_{rcv}^{G}(t) + t_{ISB} + e_{P}^{R} \tag{8.11}$$

The introduction of ISB assumes that ISB for the interval of processing (e.g., one day) is a constant. Only one additional parameter per station and per GLONASS satellite is required in PPP processing. This approach will significantly reduce the rank of the design matrix and potentially makes parameter estimation more accurate and reliable. This is an advantage against the approach used in this research. Actually both extreme approaches have their own advantages and disadvantages. As stated by *Dach et al.* (2010), the disadvantage of estimating GLONASS clock offsets directly is many more additional parameters to be estimated while the disadvantage of introducing ISB parameters is the requirement of stable ISBs during the entire processing period. As a compromise, *Dach et al.* (2010) suggests that introducing piece-wise linear ISBs with a resolution of, e.g., one hour is ideal.

Equation (8.5) virtually addresses the phase IFB between GPS and GLONASS hence it can be

fully absorbed into corresponding ambiguity parameters. However the pseudorange IFB has not been taken into account. The accurate modelling of pseudorange IFB, which requires additional parameters, will be investigated in future research.

8.5.2 Less Accurate GLONASS Orbits and Clocks

The IGS03 stream used in this study is combined using orbit and clock corrections from other ACs. *Agrotis et al.* (2014) compared IGS03 products with the IGS and ESA rapid solutions. Their statistics analyses of GPS and GLONASS corrections are summarised in Table 8.4. It is evident that the GLONASS corrections are not as accurate as their GPS counterparts. This conclusion is also supported by another research [*Hadas and Bosy*, 2014], where real-time correction data of 1-week period is compared with ESA/ESOC final products. The comparison indicates that the accuracies of real-time orbits and clocks are: 5 cm for GPS orbits, 8 cm for GPS clocks, 13 cm for GLONASS orbits and 24 cm for GLONASS clocks. In other words, the RMS errors of real-time GLONASS products are three times as large as their GPS counterparts. With quality improvement of GLONASS products in future, the accuracy of PPP-ZTD using multi-GNSS data is expected to be improved accordingly.

Table 8.4 Performance statistics of GPS and GLONASS corrections [*Agrotis et al.,* 2014]

Case	GPS Orbit 1-D RMS[a] (mm)	GPS Clock STD[a] (ns)	GLONASS Orbit 1-D RMS[b] (mm)	GLONASS Clock STD[b] (ns)
MGEX testing (31/8/2014)	21.3	0.09	35.4	0.15
RT MGEX (21/5/2014)	39.9	0.10	62.5	0.21
RT MGEX (22/5/2014)	42.6	0.13	65.1	0.21

[a]Against IGS rapid products.

[b]Against ESA rapid products.

8.6 Increase of GLONASS Parameters in Multi-GNSS Data Processing

The benefits of including GLONASS observations are demonstrated in Figure 8.2 and Figure 8.3. However, on the other side, it will also increase the number of new ambiguities which is equal to the number of GLONASS satellites at each epoch. In this research while multi-GNSS data is being processed epoch by epoch, the number of observations and parameters are also counted. As can be seen in Table 8.5, although the amount of observations increases by 67%-83% at the selected five stations, the corresponding number of GLONASS ambiguity parameters increases by 46%-59%. The increase of parameters to be estimated significantly weakens the benefits brought by the inclusion of GLONASS observations. This again requires the refinement of the functional model used in multi-GNSS PPP data processing.

Table 8.5 Increase in the number of observations and parameters in terms of GPS-only and GPS+GLONASS scenarios during DOY 012-014, 2014

Station	GPS SVs	GLONASS SVs	Multi-GNSS SVs	Number of observations increased (%)	Number of parameters increased (%)
NYA1	12	8	20	67	47
WUHN	8	6	14	75	46
NTUS	9	7	16	78	50
MOBS	10	8	18	80	53
CAS1	12	10	22	83	59

8.7 Summary

Observation equations using multi-GNSS observations are derived in this chapter. PDOP and GDOP indices are also computed based on the design matrix. The DOP values are significantly improved if GLONASS observations are also taken into account. However, the retrievals of

PPP-ZTDs using multi-GNSS data show that adding GLONASS data degrades the accuracies of PPP-ZTDs. The accuracy degradation is likely caused by at least two factors. The first factor refers to the deficiency in the functional model. Currently there are two extreme approaches to address ISB. One is to setup an additional parameter per station, per epoch and per satellite. Another is to setup an ISB parameter per station and per satellite during the whole processing period. The first approach suffers from a large number of additional GLONASS clock offset parameters while the latter makes sense as long as the ISB is reasonably stable during the whole processing time slot. A compromised approach using piece-wise linear ISB parameters would be beneficial in this context. Secondly, the quality of current real-time GLONASS orbit and clock corrections is not as good as the GPS counterpart. In that case, the GLONASS observations are usually down-weighted in multi-GNSS data processing. The post-processed ZTDs using multi-GNSS data have been proved to be accurate as is discussed in Section 1.2. However, the retrieval of ZTDs in real-time scenarios is still challenging. According to the discussions in this chapter, the real-time retrieval can be improved with the further refinement of functional model and real-time GLONASS products.

Chapter 9. Summary, Conclusions and Recommendations

9.1 Summary

This research investigates the real-time, high-accuracy and high-resolution retrievals of ZTD and PWV using GPS and GLONASS observations. Its realisation is based on substantial modifications on the BNC software package. The retrieved ZTDs and PWVs are fully validated using IGS ZTD products and radiosonde data, respectively. These ZTDs and PWVs are proved to be sufficiently accurate and meet the threshold values as input to NWP models and weather nowcasting, respectively. More specific investigations can be summarised as follows:

- Several tropospheric delay models have been compared using 71 globally distributed IGS stations which have collocated meteorological sensors. Two recently released models, i.e., GPT2 and VMF1-FC are proved to be ideal for this research and then implemented in the realisation of real-time retrievals.
- A reasonable flow chart for the real-time retrieval of PWV has been developed based on a number of empirical models which have been tested in this research. The implementation of GNSS-MET is ready to provide ZTD and PWV for NWP models and weather nowcasting, respectively. It also takes into account the high accuracy of PPP-PWVs and the reasonably low demand of computational resources.
- Error corrections for solid Earth tide, ocean tide loading, antenna PCO and PCV in PPP data processing. These corrections are essential to achieve the high accuracy of PPP-ZTD.
- A comprehensive validation of the retrieved ZTD and PWV. Stations are carefully selected so that 1) there are sufficient stations and these stations are located in different climatic regions; 2) the processing time slot for tests at each station is long enough; 3) there are reference tropospheric products from CODE and USNO to validate the derived ZTDs; 4) there are radiosonde stations in the vicinities to validate the derived

PWVs.

- A theoretical analysis of the achievable accuracy of PPP-PWV in different climatic regions based on the PPP-ZTD, various humidity and temperature conditions. How accuracies of several variables (i.e., PPP-ZTD, weighted mean temperature, ZWD and ZHD) influence the resultant PPP-PWV is also discussed in detail.
- The retrieval of PWV using multi-GNSS observations and real-time products currently available. Different weighting of GPS and GLONASS observations are tested. Different models to deal with ISB and IFB and the quality of current multi-GNSS products are also discussed.

9.2 Conclusions

The modelling of tropospheric delay in PPP processing is essential to obtain accurate ZTD or ZWD which is further used to derive PWV. One approach is to have the signal path delay mapped from ZTD using a total mapping function. However, the rapid variation of the residual ZWD will not be accounted for as the total mapping function is usually close to the corresponding hydrostatic mapping function. Apparently this approach is not ideal for GNSS-MET. Instead another approach based on the classical separation of hydrostatic and wet parts is widely used. This separation will cause a hydrostatic/wet mapping separation error [*Kouba*, 2009] as the hydrostatic mapping function usually is not identical to the corresponding wet mapping function for a specific epoch. The hydrostatic/wet mapping separation error will be deteriorated particularly at low elevation angles. This again can be clarified if we look at the normal equation of PPP as is discussed in Section 5.1. As the receiver clock offset and ZWD are highly correlated, the modelling of the *a priori* ZHD should be fairly accurate. Otherwise any error in the *a priori* ZHD cannot be fully absorbed into the ZWD parameter. Consequently, the retrieved ZTD, station coordinates and receiver clocks will not be accurate.

There are a number of empirical ZHD models that were proposed many years ago by [*Hopfield*, 1969; *Hopfield*, 1971; *Saastamoinen*, 1972; *Saastamoinen*, 1973; *Davis et al.*, 1985; *Leandro et*

al., 2006]. Recently another two new models, i.e., GPT2 and VMF1-FC have been developed by the Vienna University of Technology. All those ZHD models are compared with the reference data derived from *in-situ* pressure measurements at 71 IGS stations. The comparison reveals that GPT2 and VMF1 are superior to other empirical models. When GPT2 and VMF1-FC are implemented in PPP processing, the retrieved PPP-ZTDs are within small differences (<2 mm). Considering that VMF1-FC is dependent on external data which is continuously updated and the implementation of VMF1-FC needs a lot more computational resources, consequently the GPT2 model is used for the modelling of the *a priori* ZHD in PPP in this research.

If VMF1-FC is used in PPP then the estimated ZWD can be directly used for the conversion into PWV. Since GPT2 is used instead to save PPP processing time and computational resources, the error in the relatively coarse *a priori* ZHD will be absorbed into parameter ZWD. Hence in theory, the sum of ZHD and ZWD in PPP, i.e., ZTD is more reliable than ZWD which is directly estimated. In other words, ZTD is the final result at the end of PPP data processing in this research. The ZWD used for the conversion into PWV is then subtracted from ZTD using more accurate ZHD, which is derived using VMF1-FC. This process of GNSS-MET ensures the high-accuracies of PPP-ZTDs and PPP-PWVs while the computational resources for high-resolution PPP processing are not highly required.

Proper stochastic model for the modelling of tropospheric delays in PPP is investigated in this research. As random walk process is assumed, different values are tested and a random walk sigma of $3e^{-6}\ m/\sqrt{s}$ is proved to be ideal to follow the tropospheric variations. This means that the tropospheric effect may vary for $3600 \times 3e^{-6} \approx 0.01\ m/h$.

Solid Earth tide and ocean tide loading are two important error sources in PPP data processing. The former is caused by the Sun's and Moon's gravitational attractions, while the latter is caused by the movement of the CoM of the Earth due to ocean tides. The magnitude of the former error is at a centimetre level while the latter is one order of magnitude smaller. Both

need to be mitigated to obtain accurate ZTD. In this research these corrections are implemented following IERS 2010 conventions [*Petit and Luzum*, 2010]. There are two approaches to implement these corrections. One is to directly apply the correction to the Cartesian coordinates of station. Another approach is to reduce the station displacement into the correction in range between satellite and station. Both approaches are easily implemented.

Antenna-related corrections are also essential to obtain accurate PPP-ZTD. This involves two types of antennas (satellite and receiver) and errors (PCO and PCV). The satellite antenna PCO does not need corrections as the real-time orbits and clocks i.e., IGS02 and IGS03 used in this research are referred to satellite antenna phase centre. However, this correction is indispensable if the IGC01 stream is used. The satellite antenna PCV needs to be corrected based on the interpolation of nadir angles of GPS satellites and the absolute phase centre correction model as is discussed in Section 5.3.4. The receiver antenna PCO and PCV also need to be addressed. Those corrections have been coded into BNC and significantly improve the PPP data processing.

The retrievals of PPP-ZTDs and PPP-PWVs are validated using 20 global IGS stations. The PPP-ZTDs are compared to the reference data from USNO and CODE while the PPP-PWVs are compared to the radiosonde data which is available from a repository of atmosphere profiles provided by NOAA. The comparisons reveal that an accuracy of 12 mm is achievable for PPP-ZTD and an accuracy of 3 mm is achievable for PPP-PWV. The PPP-ZTDs and PPP-PWVs are proved to be sufficiently accurate for NWP and weather nowcasting, respectively. Note they are also with little latency and at high resolutions.

The theoretical accuracy of PPP-PWV in different climatic conditions is discussed in Section 7.4. The RMS error of PWV expressed in Equation (7.6) is proved to be a strictly increasing function of variables z_w (PPP-ZWD), T_m (weighted mean temperature), σ_t (the RMS error of PPP-ZTD), σ_h (the RMS error of ZHD for the conversion from PPP-ZTD to PPP-PWV) and σ_{T_m} (the RMS error of T_m), under reasonable assumptions. This indicates that the retrieval of

PPP-PWV is more challenging in higher temperature and humidity conditions. The good news is that even in those poor retrieval conditions (e.g. ZWD is 0.6 m and T_m is 294K), an accuracy of PPP-PWV at 3 mm level is still achievable using the real-time PPP-ZTD and the relatively coarse empirical models for T_m (a combination of GPT2 to provide surface pressure T_0 and the Bevis model for the relationship between T_0 and T_m).

The real-time retrieval of PWV using multi-GNSS data is also investigated and validated. Unfortunately the accuracy of PPP-ZTD using multi-GNSS data is lower than that uses GPS data only. However, the multi-GNSS PPP technique is still promising in future research, if piece-wise linear inter-system bias (ISB) parameters as well as inter-frequency bias (IFB) parameters are considered. Furthermore, with the quality improvement of GLONASS orbits and clocks, the accuracy of PPP-ZTD using multi-GNSS data is expected to be improved accordingly.

9.3 Recommendations

This thesis presents a comprehensive study of the real-time retrievals of ZTD and PWV using the PPP technique. The retrieved ZTD and PWV are sufficiently accurate, along with another two advantages, i.e., high resolutions and little latency. The implementation of these retrievals is applicable using the substantially modified BNC software. It is expected that the real-time PPP technique will show its promising applications in meteorology in future. Follow-on research can be conducted in terms of the following three aspects.

1) Local case studies if a national operational NWP model (e.g. the Australian ACCESS model) is available. This model is likely to improve the accuracy of PPP-PWV by providing more accurate

- the *a priori* ZHD in PPP processing;

- NWP-based a_h and a_w coefficients and the accordingly improved hydrostatic and wet mapping functions in PPP processing;
- weighted mean temperature which can be easily obtained from gridded temperature values in vertical direction. This will significantly minimise the accuracy loss at the stage of conversion of PPP-PWV from PPP-ZTD.

2) A more accurate model for multi-GNSS data processing by taking ISB and IFB into account. In this context, a piece-wise linear ISB parameter per station and per satellite can be introduced for a specific processing time slot (e.g. per hour) following equations (8.10) and (8.11). This will significantly decrease the number of additional parameters while the PPP processing is not likely to be influenced by ISB even if it is not stable.

3) Assimilation of PPP-ZTD and PPP-PWV in weather forecasting and nowcasting. Up to date, the PWV in atmosphere is still difficult to estimate using conventional sounding techniques, while the PWVs retrieved from PPP can be provided on large spatial and temporal scales. For example, in the state of Victoria, Australia, there are approximately 120 CORS stations which are likely to provide real-time PPP-PWVs at high resolutions. It would be interesting to see the improvements of weather forecasting and nowcasting when high-resolution real-time products are assimilated in the national NWP model.

References

ABC News (2014), Look back at the 2011 Queensland floods, Web Page, URL: *http://www.abc.net.au/news/2011-08-01/flood-inquiry-report-released/2819106*, Accessed on June 3, 2014.

Agrotis, L., W. Enderle, R. Zandbergen, and T. Springer (2014), Real time multi-GNSS processing at ESOC, Poster Presentation at IGS Workshop 2014, Pasadena, California, USA.

Ashby, N. (1993), Relativity and GPS, GPS World, 4(11), 42-47.

Ashby, N. (1995), Relativistic effects in the global positioning system, Journal of Systems Engineering and Electronics, 6(4), 199-237.

Askne, J., and H. Nordius (1987), Estimation of tropospheric delay for microwaves from surface weather data, Radio Science, 22(3), 379-386.

Baby, H. B., P. Golé, and J. Lavergnat (1988), A model for the tropospheric excess path length of radio waves from surface meteorological measurements, Radio Science, 23(6), 1023-1038.

Bennitt, G. V., and A. Jupp (2012), Operational assimilation of GPS zenith total delay observations into the met office numerical weather prediction models, Monthly Weather Review, 140(8), 2706-2719.

Bevis, M., S. Businger, T. A. Herring, C. Rocken, R. A. Anthes, and R. H. Ware (1992), GPS meteorology: remote sensing of atmospheric water vapor using the global positioning system, Journal of Geophysical Research, 97(D14), 15,787-715,801.

Bevis, M., S. Businger, and S. Chiswell (1994), GPS meteorology: mapping zenith wet delays onto precipitable water, Journal of Applied Meteorology, 33(3), 379-386.

Boehm, J., and H. Schuh (2004), Vienna mapping functions in VLBI analyses, Geophysical Research Letters, 31(1), L01603.

Boehm, J., A. Niell, P. Tregoning, and H. Schuh (2006a), Global Mapping Function (GMF): A new empirical mapping function based on numerical weather model data, Geophysical Research Letters, 33(7).

Boehm, J., B. Werl, and H. Schuh (2006b), Troposphere mapping functions for GPS and very long baseline interferometry from European Centre for Medium-Range Weather Forecasts operational analysis data, Journal of Geophysical Research B: Solid Earth, 111(2), B02406.

Boehm, J., R. Heinkelmann, and H. Schuh (2007), Short note: A global model of pressure and temperature for geodetic applications, Journal of Geodesy, 81(10), 679-683.

Boehm, J., and H. Schuh (2013), Atmospheric Effects in Space Geodesy, p. 243, Springer Berlin Heidelberg.

Boniface, K., V. Ducrocq, G. Jaubert, X. Yan, P. Brousseau, F. Masson, C. Champollion, J. Chéry, and E. Doerflinger (2009), Impact of high-resolution data assimilation of GPS zenith delay on Mediterranean heavy rainfall forecasting, Annales Geophysicae, 27(7), 2739-2753.

Bosy, J., J. Kaplon, W. Rohm, J. Sierny, and T. Hadas (2012), Near real-time estimation of water vapour in the troposphere using ground GNSS and the meteorological data, Annales Geophysicae, 30(9), 1379-1391.

Boudouris, G. (1963), On the index of refraction of air, the absorption and dispersion of centimeterwaves by gases, Journal of Research of the National Bureau of Standards - D. Radio Propagation, 67D(6), 631.

Bruyninx, C. (2007), Comparing GPS-only with GPS + GLONASS positioning in a regional permanent GNSS network, GPS Solutions, 11(2), 97-106.

Byram, S., and C. Hackman (2012), High-precision GNSS orbit, clock and EOP estimation at the United States Naval Observatory, Position Location and Navigation Symposium (PLANS), 2012 IEEE/ION, pp. 659-663, Myrtle Beach, SC, April 23-26, 2012.

Cai, C., and Y. Gao (2013), Modeling and assessment of combined GPS/GLONASS precise point positioning, GPS Solutions, 17(2), 223-236.

Cai, C., X. M. Luo, and J. J. Zhu (2014), Modified algorithm of combined GPS/GLONASS precise point positioning for applications in open-pit mines, Transactions of Nonferrous Metals Society of China (English Edition), 24(5), 1547-1553.

Cai, W., and P. van Rensch (2012), The 2011 southeast Queensland extreme summer rainfall: A confirmation of a negative Pacific Decadal Oscillation phase?, Geophysical Research

Letters, 39(8), L08702.

Caissy, M., L. Agrotis, G. Weber, M. Hernandez-Pajares, and U. Hugentobler (2012), The International GNSS Real-Time Service, GPS World, 23(6), 52-58.

Chao, C. C. (1974), The troposphere calibration model for mariner mars 1971, Technical Report 32-1587, pp. 61-76, NASA JPL, Pasadena, CA.

Chen, C.-S., J.-M. Lin, W.-H. Liu, and C.-L. Chi (2011), Dilution of position calculation for MS location improvement in wireless communication systems, Journal of Networks, 6(10), 1452-1458.

Chen, J., P. Xiao, Y. Zhang, and B. Wu (2013), GPS/GLONASS system bias estimation and application in GPS/GLONASS combined positioning, in China Satellite Navigation Conference (CSNC) 2013 Proceedings, edited by J. Sun, W. Jiao, H. Wu and C. Shi, pp. 323-333, Springer Berlin Heidelberg, ISBN 978-3-642-37403-6

China Satellite Navigation Office (2013a), BeiDou Navigation Satellite System Open Service Performance Standard, Technical Report, pp. 6, Beijing, China.

China Satellite Navigation Office (2013b), BeiDou Navigation Satellite System Signal In Space Interface Control Document, Technical Report, pp. 8-9, Beijing, China.

Choy, S., K. Harima, Y. Li, M. Choudhury, C. Rizos, Y. Wakabayashi, and S. Kogure (2015), GPS Precise Point Positioning with the Japanese Quasi-Zenith Satellite System LEX Augmentation Corrections, Journal of Navigation, 68(04), 769-783.

Dach, R., U. Hugentobler, P. Fridez, and M. Meindl (2007), Bernese GPS Software Version 5.0, Astronomical Institute, University of Bern, Bern, Switzerland.

Dach, R., E. Brockmann, S. Schaer, G. Beutler, M. Meindl, L. Prange, H. Bock, A. Jäggi, and L. Ostini (2009), GNSS processing at CODE: status report, Journal of Geodesy, 83(3-4), 353-365.

Dach, R., S. Lutz, M. Meindl, S. Schaer, P. Steigenberger, and G. Beutler (2010), Combining the observations from different GNSS, EGU General Assembly 2010, Vienna, Austria, May 2-7, 2010.

Davis, J. L., T. A. Herring, I. I. Shapiro, A. E. E. Rogers, and G. Elgered (1985), Geodesy by radio interferometry effects of atmospheric modeling errors on estimates of baseline length, Radio Science, 20(6), 1593-1607.

De Haan, S. (2006), National/regional operational procedures of GPS water vapour networks and agreed international procedures, Technical Report WMO/TD-No. 1340, KNMI, Netherlands.

Dee, D. P., et al. (2011), The ERA-Interim reanalysis: Configuration and performance of the data assimilation system, Quarterly Journal of the Royal Meteorological Society, 137(656), 553-597.

Dettmering, D., C. Waese, and G. Weber (2006), Networked transport of RTCM via internet protocol, NTRIP, version 1.0, Federal Agency for Cartography and Geodesy (BKG), Frankfurt, Germany.

Dousa, J., and G. V. Bennitt (2013), Estimation and evaluation of hourly updated global GPS Zenith Total Delays over ten months, GPS Solutions, 17(4), 453-464.

Dousa, J., and P. Vaclavovic (2014), Real-time zenith tropospheric delays in support of numerical weather prediction applications, Advances in Space Research, 53(9), 1347-1358.

Dow, J. M., R. E. Neilan, and C. Rizos (2009), The International GNSS Service in a changing landscape of Global Navigation Satellite Systems, Journal of Geodesy, 83(3-4), 191-198.

Dragert, H., T. S. James, and A. Lambert (2000), Ocean loading corrections for continuous GPS: A case study at the Canadian coastal site Holberg, Geophysical Research Letters, 27(14), 2045-2048.

Duan, J., et al. (1996), GPS meteorology: Direct estimation of the absolute value of precipitable water, Journal of Applied Meteorology, 35(6), 830-838.

E-GVAP (2014), E-GVAP: The EUMETNET EIG GNSS water vapour programme, Web Page, URL: *http://egvap.dmi.dk/*, Accessed on August 5, 2014.

European GNSS Programmes (2010), European GNSS (Galileo) Open Service Signal In Space Interface Control Document, Technical Report OD SIS ICD, Issue 1.1, pp. 1-2, Publications Office of the European Union, Luxembourg.

Foelsche, U., and G. Kirchengast (2001), Tropospheric water vapor imaging by combination of ground-based and spaceborne GNSS sounding data, Journal of Geophysical Research D: Atmospheres, 106(D21), 27221-27231.

Fund, F., L. Morel, and A. Mocquet (2009), Discussion and recommendations about the height

correction for a priori zenith hydrostatic delays derived from ECMWF data, Web Page, URL: *www.hg.tuwien.ac.at/~ecmwf1/Reducing_ECMWF_ZHDs.pdf*, Accessed on November 6, 2012.

Geoscience Australia (2014), Global Navigation Satellite System Networks, Web Page, URL: *http://www.ga.gov.au/earth-monitoring/geodesy/gnss-networks.html*, Accessed on November 8, 2014.

Gibbons, G. (2014), Munich Summit Charts Progress of GPS, GLONASS, Galileo, Beidou GNSSes, Web Page, URL: *http://www.insidegnss.com/node/2981*, Accessed on November 8, 2014.

GLONASS IAC (2015), Information analytical centre of GLONASS and GPS controlling, Web Page, URL: *http://glonass-iac.ru*, Accessed on January 6, 2015.

GPS Directorate (2011), GPS Interface Specification, Navstar GPS Space Segment/Navigation User Segment Interfaces, Technical Report IS-GPS-200G, pp. 112-117.

Grewal, M. S., and A. P. Andrews (2001), Kalman filtering, theory and practice using MATLAB, pp. 10-12, John Wiley & Sons, Hoboken, NJ.

Gurtner, W., and L. Estey (2009), RINEX The Receiver Independent Exchange Format Version 3.01, Technical Report, UNAVCO.

Hadas, T., and J. Bosy (2014), IGS RTS precise orbits and clocks verification and quality degradation over time, GPS Solutions, 1-13.

Hagemann, S., L. Bengtsson, and G. Gendt (2003), On the determination of atmospheric water vapor from GPS measurements, Journal of Geophysical Research D: Atmospheres, 108(21), ACL 11-11 - ACL 11-14.

Hall, M. P. M., B. L. W., and H. M. T. (1996), Propagation of radiowaves, Institution of Electrical Engineers, London.

Hauschild, A., P. Steigenberger, and C. Rodriguez-Solano (2012), Signal, orbit and attitude analysis of Japan's first QZSS satellite Michibiki, GPS Solutions, 16(1), 127-133.

Hausler, G., and P. Collier (2013), National Positioning Infrastructure: Where are we now?, IGNSS Symposium 2013, Outrigger Gold Coast, Australia.

Herring, T. A. (1992), Modelling atmospheric delays in the analysis of space geodetic data, in

Symposium on Refraction of Transatmospheric Signals in Geodesy, edited by J. C. DeMunkand and T. A. Spoelstra, pp. 157-164, Netherlands Geod. Comm., Delft, Netherlands.

Ho, S.-p., X. Yue, Z. Zeng, C. O. Ao, C.-Y. Huang, E. R. Kursinski, and Y.-H. Kuo (2014), Applications of COSMIC radio occultation data from the troposphere to ionosphere and potential impacts of COSMIC-2 data, Bulletin of the American Meteorological Society, 95(1), ES18-ES22.

Hopfield, H. S. (1969), Two-quartic tropospheric refractivity profile for correcting satellite data, Journal of Geophysical Research, 74(18), 4487-4499.

Hopfield, H. S. (1971), Tropospheric effect on electromagnetically measured range. Prediction from surface weather data, Radio Science, 6(3), 357-367.

IGS (2014), IGS-International GNSS Service, Web Page, URL: *http://www.igs.org/*, Accessed on November 8, 2014.

IGS (2015), Real-time Service, Web Page, URL: *http://igs.org/rts/products*, Accessed on January 2, 2015.

Kalman, R. E. (1960), A aew approach to linear filtering and prediction problems, Journal of Fluids Engineering, 82(1), 35-45.

Kishimoto, M., H. Hase, A. Matsumoto, T. Tsuruta, S. Kogure, N. Inaba, M. Sawabe, T. Kawanishi, S. Yoshitomi, and K. Terada (2007), QZSS system design and its performance, the 2007 National Technical Meeting of The Institute of Navigation, pp. 405-410, San Diego, CA.

Kleijer, F. (2004), Troposphere modeling and filtering for precise GPS leveling, Delft University of Technology, Delft, The Netherlands.

Kouba, J., and P. Heroux (2001), Precise point positioning using IGS orbit and clock products, GPS Solutions, 5(2), 12-28.

Kouba, J. (2008), Implementation and testing of the gridded Vienna mapping function 1 (VMF1), Journal of Geodesy, 82(4-5), 193-205.

Kouba, J. (2009), Testing of global pressure/temperature (GPT) model and global mapping function (GMF) in GPS analyses, Journal of Geodesy, 83(3-4), 199-208.

Kuo, Y.-H., Y.-R. Guo, and E. R. Westwater (1993), Assimilation of precipitable water measurements into a mesoscale numerical model, Monthly Weather Review, 121(4), 1215-1238.

Kuo, Y.-H., X. Zou, and Y.-R. Guo (1996), Variational assimilation of precipitable water using a nonhydrostatic mesoscale adjoint model. Part I: Moisture retrieval and sensitivity experiments, Monthly Weather Review, 124(1), 122-147.

Kursinski, E., G. Hajj, J. Schofield, R. Linfield, and K. R. Hardy (1997), Observing Earth's atmosphere with radio occultation measurements using the Global Positioning System, Journal of Geophysical Research: Atmospheres (1984–2012), 102(D19), 23429-23465.

Lagler, K., M. Schindelegger, J. Böhm, H. Krásná, and T. Nilsson (2013), GPT2: Empirical slant delay model for radio space geodetic techniques, Geophysical Research Letters, 40(6), 1069-1073.

Langley, R. B. (1999), Dilution of precision, GPS World, 1999(5), 52-59.

Le Marshall, J., Y. Xiao, R. Norman, K. Zhang, A. Rea, L. Cucurull, R. Seecamp, P. Steinle, K. Puri, and T. Le (2010), The beneficial impact of radio occultation observations on Australian region forecasts, Australian Meteorological and Oceanographic Journal, 60, 121-125.

Le Marshall, J., Y. Xiao, R. Norman, K. Zhang, A. Rea, L. Cucurull, R. Seecamp, P. Steinle, K. Puri, and E. Fu (2012), The application of radio occultation observations for climate monitoring and numerical weather prediction in the Australian Region, Australian Meteorological and Oceanographic Journal, 62(4), 323-334.

Leandro, R., M. Santos, and R. B. Langley (2006), UNB neutral atmosphere models: Development and performance, Proceedings of ION NTM, pp. 564-573, Monterey, CA.

Leandro, R. F., R. B. Langley, and M. C. Santos (2008), UNB3m_pack: A neutral atmosphere delay package for radiometric space techniques, GPS Solutions, 12(1), 65-70.

Lee, S. W., J. Kouba, B. Schutz, D. H. Kim, and Y. J. Lee (2013), Monitoring precipitable water vapor in real-time using global navigation satellite systems, Journal of Geodesy, 87(10-12), 1-12.

Leick, A. (2004), GPS Satellite Surveying, 3rd ed., John Wiley & Sons, Hoboken, NJ.

Li, X., M. Ge, H. Zhang, T. Nischan, and J. Wickert (2013), The GFZ real-time GNSS precise

positioning service system and its adaption for COMPASS, Advances in Space Research, 51(6), 1008-1018.

Li, X., G. Dick, C. Lu, M. Ge, T. Nilsson, N. Tong, J. Wickert, and H. Schuh (2015), Multi-GNSS Meteorology: Real-Time Retrieving of Atmospheric Water Vapor From BeiDou, Galileo, GLONASS, and GPS Observations, IEEE Transactions on Geoscience and Remote Sensing, 53(12), 6385-6393.

Li, Z., J. P. Muller, and P. Cross (2003), Comparison of precipitable water vapor derived from radiosonde, GPS, and Moderate-Resolution Imaging Spectroradiometer measurements, Journal of Geophysical Research D: Atmospheres (1984–2012), 108(D20), 1-12.

Li, Z., J. Li, W. P. Menzel, J. P. Nelson, T. J. Schmit, E. Weisz, and S. A. Ackerman (2009), Forecasting and nowcasting improvement in cloudy regions with high temporal GOES sounder infrared radiance measurements, Journal of Geophysical Research D: Atmospheres, 114(9).

Lu, C., X. Li, M. Ge, R. Heinkelmann, T. Nilsson, B. Soja, G. Dick, and H. Schuh (2015a), Estimation and evaluation of real-time precipitable water vapor from GLONASS and GPS, GPS Solutions, 1-11.

Lu, C., X. Li, T. Nilsson, T. Ning, R. Heinkelmann, M. Ge, S. Glaser, and H. Schuh (2015b), Real-time retrieval of precipitable water vapor from GPS and BeiDou observations, Journal of Geodesy, 89(9), 843-856.

Marini, J. W. (1972), Correction of satellite tracking data for an arbitrary tropospheric profile, Radio Science, 7(2), 223-231.

Melbourne, W. G. (1985), The case for ranging in GPS based geodetic systems, the 1st International Symposium on Precise Positioning with the Global Positioning System, US Department of Commerce, pp. 373–386, Rockville, MD, 15–19 April 1985.

Mendes, V. B., and R. B. Langley (1999), Tropospheric zenith delay prediction accuracy for high-precision GPS positioning and navigation, Navigation, 46(1), 25-34.

Mervart, L., and G. Weber (2011), Real-time combination of GNSS orbit and clock correction streams using a Kalman filter approach, Proceedings of the 24th International Technical Meeting of The Satellite Division of the Institute of Navigation (ION GNSS 2011), pp. 707-711, Portland, OR.

Mervart, L., and G. Weber (2013), BKG ntrip client (BNC) version 2.8, BKG, Frankfurt, Germany.

Meteorology, B. o. (2014), Severe weather events, Web Page, URL: *http://www.bom.gov.au/announcements/sevwx/*, Accessed on June 5, 2014.

Mohr, P. J., B. N. Taylor, and D. B. Newell (2012), CODATA recommended values of the fundamental physical constants: 2010, REVIEWS OF MODERN PHYSICS Rev Mod Phys, 84(4), 1527.

Molteni, F., R. Buizza, T. N. Palmer, and T. Petroliagis (1996), The ECMWF ensemble prediction system: methodology and validation, Quarterly Journal of the Royal Meteorological Society, 122(529), 73-119.

Montenbruck, O. (2014), IGS-MGEX: multi-GNSS biases, IGS Workshop 2014, Pasadena, CA, June 23-27, 2014.

Niell, A. E. (1996), Global mapping functions for the atmosphere delay at radio wavelengths, Journal of Geophysical Research B: Solid Earth, 101(2), 3227-3246.

Niell, A. E. (2000), Improved atmospheric mapping functions for VLBI and GPS, Earth, Planets and Space, 52(10), 699-702.

Niell, A. E., A. J. Coster, F. S. Solheim, V. B. Mendes, P. C. Toor, R. B. Langley, and C. A. Upham (2001), Comparison of measurements of atmospheric wet delay by radiosonde, water vapor radiometer, GPS, and VLBI, Journal of Atmospheric and Oceanic Technology, 18(6), 830-850.

Norman, R., J. Le Marshall, C. S. Wang, B. Carter, Y. Li, S. Gordon, and K. Zhang (2012), Simulating GPS Radio Occultations using 3-D numerical ray tracing, Geoscience and Remote Sensing Symposium (IGARSS), 2012 IEEE International, pp. 2446-2449, 22-27 July 2012.

Owens, J. C. (1967), Optical refractive index of air: dependence on pressure, temperature and composition, Applied Optics, 6(1), 51-59.

Pacione, R., and W. Söhne (2014), Exploitation of IGS real-time products for tropospheric monitoring, Oral Presentation IGS Workshop 2014, Pasadena, CA, June 23, 2014.

Petit, G., and B. Luzum (2010), Chapte 7: Displacement of reference points, in IERS technical note No. 36 (IERS conventions 2010), edited by Gérard Petit and B. Luzum, ISBN

3-89888-989-6

Poli, P., P. Moll, F. Rabier, G. Desrozier, B. Chapnik, L. Berre, S. B. Healy, E. Andersson, and F. Z. El Guelai (2007), Forecast impact studies of zenith total delay data from European near real-time GPS stations in Météo France 4DVAR, Journal of Geophysical Research D: Atmospheres, 112(6).

Puri, K., et al., (2010), Preliminary results from Numerical Weather Prediction implementation of ACCESS, CAWCR Research Letters, 5, 15-22.

Rao, K. S. (2007), Presentation of the Indian Regional Navigation Satellite System (IRNSS), Oral Presentation at the 1st Meeting of the International Committee on Global Navigation Satellite Systems (ICG), Bangalore, India.

Rao, V. G., G. Lachapelle, and S. Vijaykumar (2001), Analysis of IRNSS over Indian subcontinent, the 2011 International Technical Meeting of The Institute of Navigation, pp. 1150-1162, San Diego, CA.

Revercomb, H. E., et al. (2003), The Arm Program's water vapor intensive observation periods, Bulletin of the American Meteorological Society, 84(2), 217-236.

Rocken, C., T. Van Hove, and R. Ware (1997), Near real-time GPS sensing of atmospheric water vapor, Geophysical Research Letters, 24(24), 3221-3224.

Rohm, W., Y. Yuan, B. Biadeglgne, K. Zhang, and J. L. Marshall (2014), Ground-based GNSS ZTD/IWV estimation system for numerical weather prediction in challenging weather conditions, Atmospheric Research, 138(0), 414-426.

Ross, R. J., and S. Rosenfeld (1997), Estimating mean weighted temperature of the atmosphere for Global Positioning System applications, Journal of Geophysical Research D: Atmospheres, 102(18), 21719-21730.

Rothacher, M., and R. Schmid (2014), ANTEX: The Antenna Exchange Format, Version 1.4 Web Page, URL: *ftp://igs.org/igscb/station/general/antex14.txt*, Accessed on August 10, 2014.

Rüeger, J. M. (2002), Refractive index formulae for radio waves, XXII FIG International Congress: ACSM/ASPRS Annual Conference, Washington DC, USA, April 19-26, 2002.

Russian Institute of Space Device Engineering (2008), GLONASS Interface Control Document: Navigation Radiosignal in Bands L1, L2, Technical Report ICD L1, L2

GLONASS, pp. 20-22, Moscow, Russia.

Saastamoinen, J. (1972), Atmospheric correction for the troposphere and stratosphere in radio ranging satellites, in The Use of Artificial Satellites for Geodesy, Geophysical monograph series, edited by A. M. S. W. Henriksen, and B. H. Chovitz, pp. 247-251, AGU, Washington, D. C.,

Saastamoinen, J. (1973), Contributions to the theory of atmospheric refraction - Part II. Refraction corrections in satellite geodesy, Bulletin Géodésique, 47(1), 13-34.

Schmid, R., and M. Rothacher (2003), Estimation of elevation-dependent satellite antenna phase center variations of GPS satellites, Journal of Geodesy, 77(7-8), 440-446.

Schmid, R., P. Steigenberger, G. Gendt, M. Ge, and M. Rothacher (2007), Generation of a consistent absolute phase-center correction model for GPS receiver and satellite antennas, Journal of Geodesy, 81(12), 781-798.

Shi, J., C. Xu, Y. Li, and Y. Gao (2015), Impacts of real-time satellite clock errors on GPS precise point positioning-based troposphere zenith delay estimation, Journal of Geodesy, 89(8), 747-756.

Smith, E. K., and S. Weintraub (1953), The constants in the equation for atmospheric refractive index at radio frequencies, Proceedings of the IRE, 41(8), 1035-1037.

Smith, T. L., S. G. Benjamin, S. I. Gutman, and S. Sahm (2007), Short-range forecast impact from assimilation of GPS-IPW observations into the rapid update cycle, Monthly Weather Review, 135(8), 2914-2930.

Springer, T. A., and U. Hugentobler (2001), IGS ultra rapid products for (Near-) real-time applications, Physics and Chemistry of the Earth, Part A: Solid Earth and Geodesy, 26(6-8), 623-628.

Steigenberger, P., J. Boehm, and V. Tesmer (2009), Comparison of GMF/GPT with VMF1/ECMWF and implications for atmospheric loading, Journal of Geodesy, 83(10), 943-951.

Sturman, A. P., and N. J. Tapper (2006), The weather and climate of Australia and New Zealand, 2nd ed., pp. 520, Oxford University Press, Oxford, UK.

Stürze, A., S. Liu, and W. Söhne (2014), Real-Time tropospheric delay estimation using IGS products, EGU General Assembly 2014, pp. 5201, Vienna, Austria, April 27 - May 2,

2014.

Takasu, T. (2009), RTKLIB: Open source program package for RTK-GPS, Oral Presentation at FOSS4G 2009 Tokyo, Tokyo, Japan, November 2, 2009.

Teke, K., et al. (2011), Multi-technique comparison of troposphere zenith delays and gradients during CONT08, Journal of Geodesy, 85(7), 395-413.

Texas Tech University (2014), Lecture: GPS field mapping and data aquisition, Web Page, URL: *http://gis.ttu.edu/gist4310/documents/lectures/Fall* 2012/4310-04 Principles of GPS Operation.pdf, Accessed on October 10, 2014.

Thayer, G. D. (1974), An improved equation for the radio refractive index of air, Radio Science, 9(10), 803-807.

Tregoning, P., R. Boers, D. O'Brien, and M. Hendy (1998), Accuracy of absolute precipitable water vapor estimates from GPS observations, Journal of Geophysical Research D: Atmospheres, 103(D22), 28701-28710.

University of Tennessee (2014), Teaching notes: the Earth's Atmosphere, Web Page, URL: *http://csep10.phys.utk.edu/astr161/lect/earth/atmosphere.html*, Accessed on October 12, 2014.

Uppala, S. M., et al. (2005), The ERA-40 re-analysis, Quarterly Journal of the Royal Meteorological Society, 131(612), 2961-3012.

US AIR FORCE (2014), 50 SW completes GPS constellation expansion, Web Page, URL: *http://www.gps.gov/systems/gps/space/*, Accessed on September 8, 2014.

US Government (2008), GPS Standard Positioning Service Performance Standard, Technical Report GPS SPS PS, pp. 3-5, Washington, DC.

US Naval Observatory (2014), USNO NAVSTAR Global Positioning System, Web Page, URL: *http://tycho.usno.navy.mil/gpsinfo.html*, Accessed on June 5, 2014.

van den Honert, R. C., and J. McAneney (2011), The 2011 Brisbane floods: causes, impacts and implications, Water, 3(4), 1149-1173.

Vicmap Position (2014), CORS Interactive Map, Web Page, URL: *http://gnss.vicpos.com.au/Map/SensorMap.aspx*, Accessed on August 8, 2014.

Wahr, J. M. (1981), The forced nutations of an elliptical, rotating, elastic and oceanless earth,

Geophysical Journal of the Royal Astronomical Society, 64(3), 705-727.

Wickert, J., C. Reigber, G. Beyerle, R. König, C. Marquardt, T. Schmidt, L. Grunwaldt, R. Galas, T. K. Meehan, and W. G. Melbourne (2001), Atmosphere sounding by GPS radio occultation: First results from CHAMP, Geophysical Research Letters, 28(17), 3263-3266.

Wu, J. T., S. C. Wu, G. A. Hajj, W. I. Bertiger, and S. M. Lichten (1992), Effects of antenna orientation on GPS carrier phase, Man. Geodetica, 18, 91-98.

Wübbena, G. (1985), Software developments for geodetic positioning with GPS using TI 4100 code and carrier measurements, the 1st International Symposium on Precise Positioning with the Global Positioning System, US Department of Commerce, pp. 403–412, Rockville, MD.

Xu, A., Z. Xu, M. Ge, X. Xu, H. Zhu, and X. Sui (2013), Estimating zenith tropospheric delays from BeiDou navigation satellite system observations, Sensors, 13(4), 4514-4526.

Xu, G. (2007), GPS: Theory, Algorithms and Applications, 2nd ed., Springer, Heidelberg.

Yan, S., Z. Li, K. Yu, and K. Zhang (2014), GPS-R L1 interference signal processing for soil moisture estimation: an experimental study, EURASIP Journal on Advances in Signal Processing, 2014(1), 107.

Yao, Y., S. Zhu, and S. Yue (2012), A globally applicable, season-specific model for estimating the weighted mean temperature of the atmosphere, Journal of Geodesy, 86(12), 1125-1135.

Yao, Y., C. Xu, B. Zhang, and N. Cao (2014), GTm-III: A new global empirical model for mapping zenith wet delays onto precipitable water vapour, Geophysical Journal International, 197(1), 202-212.

Yao, Y. B., B. Zhang, S. Q. Yue, C. Q. Xu, and W. F. Peng (2013), Global empirical model for mapping zenith wet delays onto precipitable water, Journal of Geodesy, 1-10.

Yuan, Y., K. Zhang, W. Rohm, S. Choy, R. Norman, and C.-S. Wang (2014), Real-time retrieval of precipitable water vapor from GPS precise point positioning, Journal of Geophysical Research: Atmospheres, 119(16), 2014JD021486.

Zhang, K., F. Wu, S. Wu, C. Rizos, C. Roberts, L. Ge, T. Yan, C. Gordini, A. Kealy, and M. Hale (2006), Sparse or dense: Challenges of Australian network RTK, Proceedings of the IGNSS2006 Symposium, Paper(80), 17-21.

Zhang, K., E. Fu, D. Silcock, Y. Wang, and Y. Kuleshov (2011), An investigation of atmospheric temperature profiles in the Australian region using collocated GPS radio occultation and radiosonde data, Atmospheric Measurement Techniques, 4(10), 2087-2092.

Zhang, K., T. Manning, S. Wu, W. Rohm, D. Silcock, and S. Choy (2015), Capturing the Signature of Severe Weather Events in Australia Using GPS Measurements, Selected Topics in Applied Earth Observations and Remote Sensing, IEEE Journal of, 8(4), 1839-1847.

Zumberge, J. F., M. B. Heflin, D. C. Jefferson, M. M. Watkins, and F. H. Webb (1997), Precise point positioning for the efficient and robust analysis of GPS data from large networks, Journal of Geophysical Research B: Solid Earth, 102(B3), 5005-5017.

List of Publications

Yuan, Y., K. Zhang, S. Choy and W. Rohm (2015), Real-time high-accuracy retrievals of precipitable water vapour from GNSS precise point positioning, paper presented at *IGNSS 2015 Symposium*, Gold Coast, Australia, 16-18 July, 2015

Yuan, Y., K. Zhang, W. Rohm, S. Choy, R. Norman, and C. S. Wang (2014), Real-time retrieval of precipitable water vapor from GPS precise point positioning, *Journal of Geophysical Research: Atmospheres*, *119*(16), 2014JD021486.

Rohm, W., Y. Yuan, B. Biadeglgne, K. Zhang, and J. L. Marshall (2014), Ground-based GNSS ZTD/IWV estimation system for numerical weather prediction in challenging weather conditions, *Atmospheric Research*, *138*(0), 414-426.

Wu, S., T. Manning, Y. Yuan, X. Wang, A. Kealy, J. L. Marshall, and K. Zhang (2014), Strengthening severe weather prediction using the advanced Victorian regional GPS network-a recent NDRGS project, GSR_3, CEUR-WS, pp. 1-7.

Rohm, W., T. Manning, Y. Yuan, B. Biadeglgne, S. Choy, and K. Zhang (2013), GNSS meteorology for severe weather - 1D, 2D and 3D solution, *EGU General Assembly 2013*, Vienna, Austria.

Yuan, Y., W. Rohm, S. Wu, K. Zhang, and S. Choy (2012), Advanced weather prediction and severe weather monitoring using national GNSS CORS infrastructure - preliminary results, paper presented at *Geospatial Science Research_2 Symposium*, Melbourne, Australia, 10-12 December, 2012.